Diffusion and surface effects for SiC implanted with fission product elements

by

Remeredzai Joseph Kuhudzai

Submitted in partial fulfillment of the requirements for the degree of

DOCTOR OF PHILOSOPHY (PHD) IN PHYSICS

in the Faculty of Natural and Agriculture Sciences at the University of Pretoria

April……2015

Supervisor/Promoter: Prof. J.B. Malherbe

Co-supervisor: Prof. E.K.H. Friedland

Diffusion and surface effects for SiC implanted with fission product elements

By

Remeredzai Joseph Kuhudzai

Submitted in partial fulfilment of the requirements for the degree of (PhD) in Physics in the Faculty of Natural and Agricultural Science, University of Pretoria

Supervisor/Promoter: Prof. J.B. Malherbe

Co-supervisor: Prof. E.K.H. Friedland

SUMMARY

The diffusion and surface effects of several fission product elements implanted in SiC have been investigated. SiC is used as the main barrier for fission products in modern high temperature gas cooled reactors. An understanding of the transport behaviour of the implanted ions and their interactions with SiC will shed some light into SiC's effectiveness in the retention of fission products. The diffusion behavior of cesium implanted into SiC was investigated by isochronal and isothermal annealing methods up to temperatures of 1500 ºC. Ion implantation was performed at three temperatures, which were room temperature, 350 and 600 ºC. The implantation fluences in all cases were in the order of 10^{16} ions per cm^2. The implantation depth profiles before and after annealing were determined by Rutherford backscattering spectroscopy (RBS). The cesium diffusion results were compared with results from our previous studies on the diffusion behaviour of atoms of iodine, silver, strontium and xenon in SiC. Amorphisation of the SiC was observed for room temperature implantations but not for implantations at 350 ºC and at 600 ºC. A strong temperature dependence of irradiation induced diffusion was observed for the cesium implanted samples.

For room temperature implanted samples, isochronal annealing cycles showed that almost 50% of the implanted cesium is lost after the first annealing cycle. This behavior was similar to previous results on the loss of strontium during the first annealing cycle and to some extent previous data on silver loss where also some loss was observed after the first annealing

cycles. However this behavior was in sharp contrast to the diffusion behaviour of iodine and xenon where no losses were observed after similar annealing cycles. About 25 % of the cesium is lost in the case of the samples implanted at 350 ºC while no loss of implanted cesium is observed for samples annealed at 600 ºC.

For new high temperature isochronal annealing studies of silver and iodine room temperature implanted samples, complete loss of the implanted silver was observed after annealing at 1500 ºC for 30 hours. In the case of the iodine implanted samples under the same conditions, a significant amount of iodine was retained. These results showed that silver diffuses faster through the initially amorphised SiC than iodine. RBS results also showed that thermal decomposition of SiC at these temperatures due to the sublimation of silicon leaving a carbon layer on the surface appears to be more drastic in the case of the silver implanted samples as compared to the iodine implanted samples. Iodine appears to have some effect in slowing down the decomposition of SiC. This result was confirmed by Scanning Electron Microscopy (SEM) measurements. SEM also revealed that the surfaces of silver implanted samples contained more cavities than the iodine implanted samples after the annealing cycles.

The thermal decomposition was also investigated by Raman spectroscopy. Raman spectroscopy was performed using two laser wavelength excitation regimes. These were the 514 nm laser (visible region) and the 244 nm laser (deep ultraviolet region, DUV). Raman spectra show that the surface region of SiC at 1600 ºC had completely decomposed and the top surface layer was now covered by a carbon layer. Raman measurements with laser in the visible region showed that the extent of decomposition at 1600 ºC was greater for the silver implanted samples than for the iodine implanted samples. When ions of both elements (iodine and silver) were co-implanted in the same wafer and annealed under the same conditions as the single element implanted samples, iodine was observed to assist in the retention and trapping of silver ions. This was observed via Secondary Ion Mass Spectrometry (SIMS), Heavy Ion Elastic Recoil Detection Analysis (HI-ERDA), and Atom Probe Tomography (APT).

The differences in the diffusion behaviour observed between cesium and the other elements in SiC as well as the effect of iodine in the trapping of silver ions when both ions were co-implanted in SiC led us to perform a new systematic study of the surface microstructure of

samples implanted with the various elements and its effect on the diffusion. Amorphous surface layers were produced by ion implantation of 360 keV ions of iodine, silver, xenon, cesium and strontium into single crystalline 6H-SiC samples at room temperature. Vacuum annealing of the damaged silicon carbide samples was then performed. The microstructure of SiC surfaces before and after annealing was investigated using a high resolution field emission SEM. SEM analysis complemented by Atomic Force Microscopy (AFM) showed that nano-crystallites developed for all implanted samples after annealing. Larger and more faceted crystallites along with elongated thin crystallites were observed for iodine and xenon implanted 6H-SiC. Crystallites formed on surfaces implanted with strontium and cesium were smaller and less faceted. Strontium, silver and cesium implanted samples also exhibited more cavities on the surface. AFM was used to evaluate the effect of annealing on the surface roughness. For all the amorphous surfaces which were essentially featureless, the root mean square (rms) roughness was approximately 1 nm. The roughness increased to approximately 17 nm for iodine implanted samples after annealing with surface roughness below this value for all the other samples. AFM also showed that the largest crystals grew to heights of about 17 nm, 20 nm, 45 nm, 50 nm and 65 nm for Sr, Cs, Ag, Xe and I implanted samples after annealing at 1200 °C for 5 hours respectively. SEM images and AFM analysis suggest that iodine is more effective in promoting crystal growth during the annealing of bombardment-induced amorphous SiC than the rest of the ions we implanted. From the SEM images, It is therefore expected that iodine and xenon are more likely to be retained in SiC while the large cavities observed on silver and cesium and the cavities on strontium implanted samples could provide paths for their release. This is in agreement with the loss of implanted elements observed from the diffusion results. This is an important result indicating that the interaction of the fission product elements with the SiC itself can play a role in the diffusion and containment of the fission product elements.

DECLARATION

I, Remeredzai Joseph Kuhudzai declare that the thesis, which I hereby submit for the degree of PhD in Physics at the University of Pretoria is my own work and has not previously been submitted by me for a degree at this or any other tertiary institution.

Signature: ……

Date: ……

Acknowledgements

I would like to acknowledge the following people for their support in making this study a success.

- My academic promoter, Prof. J.B. Malherbe, my co-promoter Prof. E. Friedland and Dr. N.G. van der Berg for their wonderful guidance and mentorship during this study.

- The head of department, Prof. C.C. Theron, for arranging some part-time work in the department which helped my finances during my study.

- The University of Pretoria Research and Innovation office for Financial Assistance

- Ms Elfrieda Meyburgh for all the assistance in the Physics department.

- Dr E. Wendler and colleagues from Jena, Germany.

- Dr. A. Devaraj, Dr. Z. Zhu, Dr. M. Nandasiri and Dr. S. Thevuthasan from the EMSL, PNNL, Richland, USA

- Dr Mandla Msimanga, for assistance with the ERDA

- Dr Linda Prinsloo for the helpful discussions on Raman spectroscopy, Dr. Rudolph Erasmus from Wits School of Physics for DUV Raman, Antoinette Buys for all the help with AFM and SEM, Andre Botha for help with SEM

- My colleagues in the Physics Department, Dr. T.T. Hlasthwayo, Dr. W. Mtangi, Ope, Eric, Thabsile, Prince, Farshard and Thoko for their encouragement and moral support.

- My wife Rutendo and my daughter Upendo for all the love.

- My brothers Keith, Takachida and Ruvimbo, my sister Rutendo and her husband Simba, my sister in laws Kudzi, Henrietta and Edith, my nieces Tarisai, Tanaka, Tarisiro and Tirimunashe and nephew Tawana for their love and support.

- My Father in law Mr Makonyere, Mrs Makonyere, Tsitsi , Sipi, Sibb, Kuziwa and Kain.

- My late parents Mr and Mrs G.N. Kuhudzai for giving me a great foundation to be who I am today, and my late brother Farikai for being a loving brother and mentor.

List of abbreviations

AES-Auger Electron Spectroscopy

AFM-Atomic Force Microscopy

APT- Atom Probe Tomography

AVR- Arbeitsgemeinschaft Versuchsreaktor

BSE- Backscattered Electrons

CAB- Cores and Bonds model

CFE-Cold Field Emission source

CHA- Concentric Hemispherical Analyser

DLD- Delay line Detector

EBSD- Electron Backscatter Diffraction

EDS- Energy Dispersive X-ray Spectroscopy

EMSL- Environmental Molecular Sciences Laboratory

E-T-Everhart-Thornly

FEG-Field Emission Gun

FE-SEM- Field Emission Scanning Electron Microscope

FIB- Focused Ion Beam

FWHM-Full Width at Half Maximum

HI-ERDA-Heavy Ion Elastic Recoil Detection Analysis

HTGR- High Temperature Gas Cooled Reactor

IRP- Integrated Resource Plan

LEAP- Local Electrode Atom Probe

LV-SEM- Low Voltage Scanning Electron Microscopy

MCA- Multichannel Analyser

MCP- MicroChannel Plate

NA- Numerical Aperture

NDP -National Development Plan

NIASA- Nuclear Industry Association of South Africa

PBMR- Pebble Bed Modular Reactor

PIPS- Passivated Implanted Planar Silicon Detector

PNNL- Pacific Northwest National Laboratory

RBS-C- Rutherford Backscattering Spectrometry with Channeling

RHEED- Reflection High Energy Electron Diffraction

SE- Secondary Electron

SEM- Scanning Electron Microscopy

SFM- Scanning Force Microscopy

SHE-Schottky Emitter

SIMS- Secondary Ion Mass Spectrometry

SiC-Silicon Carbide

SNOM- Scanning Near Field Optical Microscopy

SPE- Solid Phase Epitaxy

SPM- Scanning probe Microscopy

STM- Scanning Tunneling Microscopy

TEM- Transmission Electron Microscopy

TFE- Thermal Field Emission source

ToF- Time of Flight

TRISO-Tri-Isotropic

XPS- X-Ray Photoelectron Spectroscopy

Table of contents

List of figures

List of tables

For My Girls

Rutendo and Upendo

Chapter 1: Introduction and Background

1.1 Motivation for new generation nuclear reactors

Nuclear reactors are expected to play a major role in meeting the world's ever increasing energy demands. The decreasing supply of fossil fuels and the need to reduce green house gas emissions are the major factors influencing this renewed drive for the development of alternative energy sources. High Temperature Gas Cooled Reactors (HTGR's) are part of the group of designs known as Generation IV reactors and are being considered for electricity generation. They also possess the added advantage for process heat applications such as high temperature electrolysis for the production of hydrogen by water splitting as opposed to the conventional production of hydrogen from hydrocarbons.

The HTGR uses coated fuel particles to permit high outlet coolant temperature. The helium coolant gas and the graphite, employed as a moderator, offer enhanced thermal and neutron efficiency respectively [Eld09]. Generation IV reactors promise advances in sustainability, safety, reliability, economic benefits and the stifling of proliferation risks due to low fuel enrichment levels [Mal08]. In South Africa, The South African Government is pursuing the so-called New Build Program underpinned by key legislation. This legislation includes The National Development Plan (NDP of 2012) and The Integrated Resource Plan for Electricity (IRP 2010-2030) [www1]. The IRP is the government's plan for broadening South Africa's energy mix to include technologies that reduce greenhouse gases between 2010 and 2030. These technologies include renewables such as wind, solar and hydro along with 9.6 GW of new nuclear power stations [www2]. Apart from the nuclear program's suitability for providing predictable on demand baseload power, the Nuclear Industry Association of South Africa (NIASA) report (www2) also cite the economic benefits of the new build program towards job creation. Table 1 illustrates the number of new staff to be trained for the 9.6 GW scenario [www2].

Table1: Total number of new staff to be trained for the new build program for the 9.6 GW case. Taken from [www2].

Trade	**Number of workers to be trained**
Technicians	2 606
Planners	60
Scientists	78
Professionals	203
Engineers	997
Artisans	25 147
Instructors	192
Project Managers	489
AE	1 826
Other	598
Total	**32 196**

1.2 The Pebble Bed Modular Reactor (PBMR)

The Pebble Bed Modular Reactor, (PBMR) had been proposed as the HTGR design for South Africa and China [Mal08]. This PBMR uses the Tri-Isotropic (TRISO) particle design consisting of a (UO_2) fuel kernel surrounded by successive layers of a low density pyrolytic carbon, a high density pyrolytic carbon, silicon carbide (SiC) and an outer layer of high density pyrolytic carbon [Ber10,Sch90]. The porous carbon buffer layer is designed to

protect the inner pyrolytic carbon layer from damage by recoiling fission fragments from the kernel. It contributes voids to compliment the voids contained in the fuel kernel to capture gasses created by the fission process, thereby reducing the pressure exerted on the denser inner pyrolytic carbon. The inner pyrolytic carbon acts as a barrier for gaseous fission products and reduces tensile stress in SiC layer [Ber10,Han03,Mal08]. The SiC layer in between the two high density pyrolytic carbon layers is considered the main barrier to fission product release, especially for metallic fission products. The outer pyrolytic carbon layer protects SiC layer from possible external mechanical and chemical interactions or attacks. It also helps to reduce tensile stress in the SiC [Nic02].

Commissioning of the HTGR's will depend on their ability to retain the radioactive fission products. Fission products not retained are transported from their original fission sites through the fuel material to the surface of the coated spheres where they are desorbed into the coolant gas or plate out onto the cooler surfaces of the primary circuit, like the colder parts of the steam generator. The released fission products pose a risk to people who access the main power system for maintenance purposes and increase the demands for decontamination of the plant. Inhalation, ingestion and absorption are the major potential exposure pathways of the radiation. The levels of exposure could be increased in accident conditions. A depressurization accident will result in loss of the contaminated primary coolant to the atmosphere. A water ingress accident will remobilize the fission products that would have plated out, (deposited) on the components of the primary coolant circuit by scrubbing of water and steam [Yua02].

The structure of the TRISO particle is shown in figure 1.1

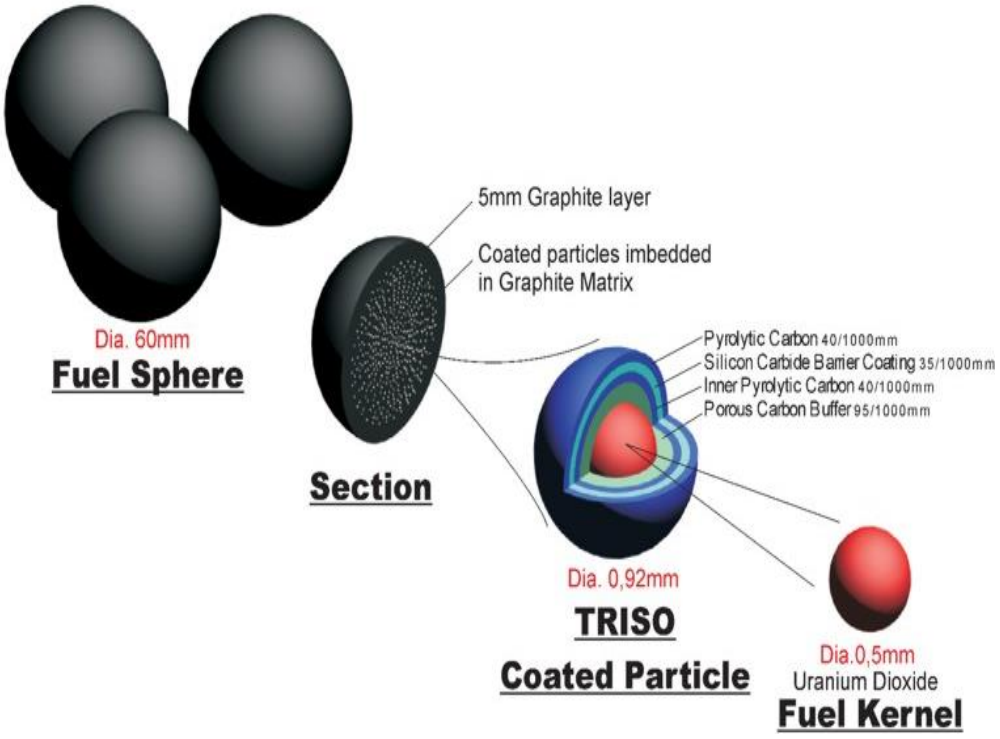

Figure 1.1: Schematic diagram of fuel for a pebble-bed modular reactor. Taken from [www3].

1.3 Silicon Carbide (SiC)

The choice of silicon carbide, (SiC) as the main barrier to the fission products is influenced by its exceptional mechanical properties and its ability to retain these properties at high temperatures. SiC is one of the hardest materials known with a Mohs hardness of around 9.5. The hardness is due to a high bond strength resulting from the short bond length between Si and C which is about 1.89 Å [Zso05]. SiC has a high corrosion resistance and also good resistance to chemical and abrasive attack. It has a high thermal conductivity which allows for lower operating fuel temperature. SiC's appeal is also strongly influenced by its low neutron absorption cross section. Perhaps the most important feature of SiC that supports its case as the main barrier to fission products in the TRISO particle is its high thermal stability. SiC maintains its outstanding mechanical properties at high temperatures above 1000°C [Pir93]. The highest designed temperature of modern HTGR's under normal operation is averages around 950 °C with 600 – 700 °C being the more common proposed temperatures. The core temperature does not exceed 1600°C [Moo08] in case of core heat up events. SiC

sublimates at temperatures around 2800°C [Zso05, Wol05], however, other authors note that SiC melts at around 2700°C [Wan08] and others have noted that SiC is already decomposing at around 1500°C into Si, C, SiC_2 and Si_2C [Ber12,Lil93]. Therefore SiC should in principle be a reliable barrier to fission products during the operation of the reactor under normal operating conditions of around 900°C. In this thesis we shall investigate some new aspects concerning the thermal stability of SiC – see sections 7.1 and 7.3.

The structure of SiC can be considered to be an assembly of tetrahedra [Pir93, Sne07], with two neighbouring tetrahedra, joined together at their corners. The mostly covalent bonded tetrahedron, can take any of the two forms SiC_4 or CSi_4 as shown in figure 1.2 [Zso05]. A silicon atom can be at the center of the tetrahedron surrounded by four carbon atoms or a carbon atom at the centre of the tetrahedron surrounded by four silicon atoms. The tetrahedral bond angle Θ shown in figure 1.2 is approximately 109° and the angle between two faces in the tetrahedral is approximately 70º [Bra88,Zso05].

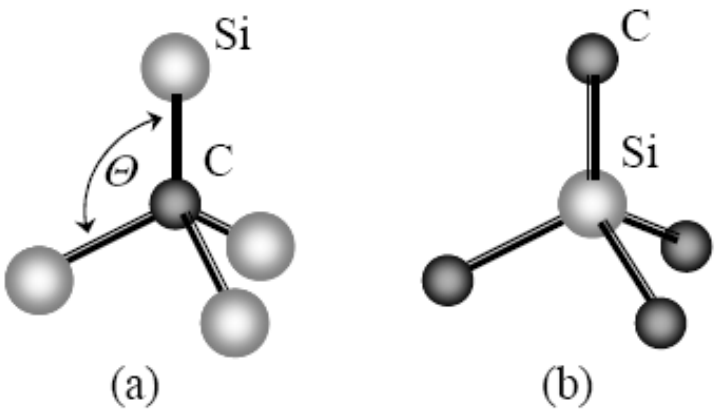

Figure 1.2: Tetrahedra showing (a) one carbon and four silicon atoms (b) one silicon and four carbon atoms. Taken from [Zso05].

A difference in the stacking sequence of identical atomic planes along a principal crystallographic axis and a large number of possible combinations of this stacking sequence, result in silicon carbide exhibiting a phenomenon known as polytypism. SiC is known to

have over 200 polytypes [Dev00]. The Ramsdell notation is widely used to describe the polytypes [Zso05]. The Ramsdell notation uses a number followed by a letter to prefix acronym SiC. The number represents the count of double layers in one period and the letter defines the symmetry with the more common letters, C and H standing for Cubic and Hexagonal respectively. Only one cubic polytype, 3C-SiC is known and the most common hexagonal polytypes are 4H-SiC and 6H-SiC [Dev00].

The tetrahedra mentioned above are arranged in such a way that all the atoms lie in parallel planes on the nodes of hexagonal networks. Two basic stacking sequences are possible in SiC [Wes96]. If the projections of silicon atoms in three successive layers of the stack are in three different positions A (circles), B (squares) and C (triangles) as shown in figure 1.3 (b) then the cubic (also known as zincblende) lattice is formed [Wes 96]. However, if the projection of the atoms in the third silicon layer coincides with the position of the first one (A) then the hexagonal (also known as wurtzite) lattice is formed as shown in figure 1.3 (c).

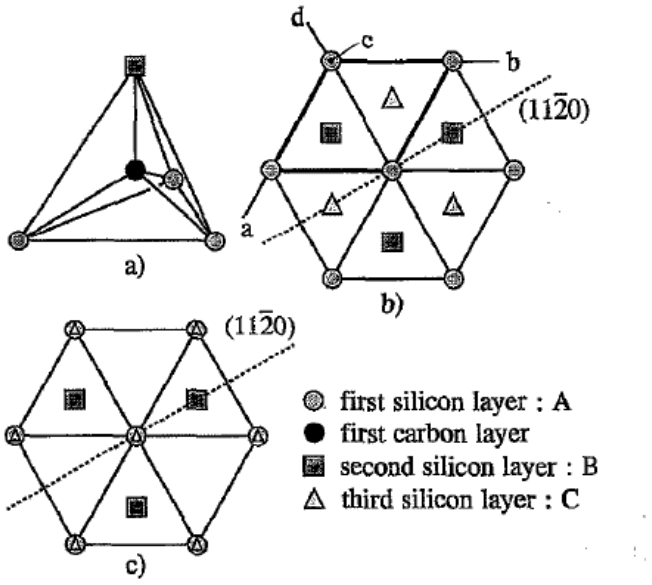

Figure 1.3: SiC tetrahedral (a) and projection of the different positions of the silicon atoms in the zinc blende structure (b) (the axes system and base of the unit cell are indicated) along with the wurzite structure (c). Taken from [Wes96].

Despite the many polytypes and different modifications of SiC, SiC crystals can be described in the hexagonal axis system with three axes a, b and d at 120º to one another and one axes, the c axis, being perpendicular to them. Figure 1.3 (b) shows the axes and the base of the hexagonal unit cell. Along with figure 1.3 (c), these two illustrations show that $(11\bar{2}0)$ planes give a correct representation of the SiC structure as all the relevant atoms lie in these planes [Wes96]. The cubic (zinc blende), on the left of figure 1.4 and the hexagonal (wurtzite) are shown on the right of the same figure 1.4 below.

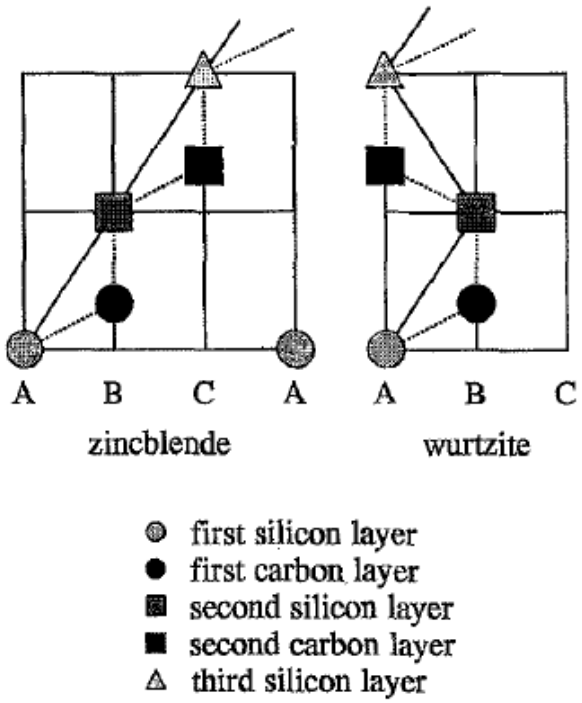

Figure 1.4: Position of silicon and carbon atoms in $(11\bar{2}0)$ planes of the cubic (zinc blende) and hexagonal (wurtzite) structures. Taken form [Wes96].

The positions of silicon carbide atoms in the $(11\bar{2}0)$ planes are shown in figure 1.5.

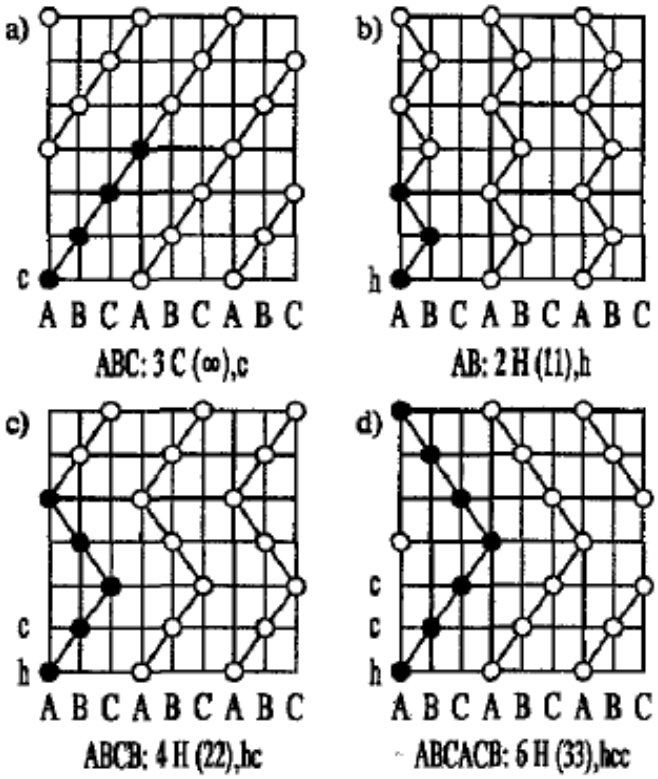

Figure 1.5: Position of silicon atoms in planes of the common polytypes. Taken from [Wes96].

Here the bold horizontal lines mark the completion of a unit cell along the c axis. The zinc blende structure requires three successive steps in the same direction resulting in the stacking sequence ABCABC (figure 1.5 (a)). This cubic lattice in the previously mentioned Ramsdell notation is known as 3C. A unit cell of the wurtzite structure is built on the sequence of one step to the right and one step to the left with the stacking order ABAB as shown in figure 1.5 (b). This stacking sequence is known as 2H. All other polytypes of SiC are characterized in the same manner and the most common hexagonal ones 4H and 6H are shown in figures 1.5 (c) and (d). The atoms in black in the figure are used to highlight the stacking sequence.

In this work we have used 6H-SiC wafers supplied by Cree Inc®. Cree Inc® uses the Modified Lely Method to prepare the wafers.

1.4 Motivation for simulation of neutron irradiation effects in reactor conditions with heavy ion irradiation as a surrogate.

Heavy ion irradiation for the purpose of simulating reactor conditions *vis-á-vis* neutron damage to materials has been employed since the1960's [Was07]. This stems from the fact that radiation damage occurring in SiC at fluences below the critical fluence for amorphisation are similar for ions and neutrons at the same displacement per atom (dpa) value [Mal13]. At low irradiation fluences and low temperatures, the main defects formed are point defects for both ion and neutron irradiation. However, in the case of neutron irradiation, point defects can also arise from neutron capture reactions [Mal08]. In reactor environments, most of the damage to materials is due to atomic collisions with fast neutrons which produce collision cascades. In projectile particle-solid interactions, an impinging particle may transfer enough energy to a target atom for that target atom to knock on further atoms down the line resulting in a series of tertiary knock-ons. It is these sequences of binary collisions that lead to collision cascades. During ion irradiation experiments, models developed to describe damage formation also include cascade formation. These collision cascades will be explained in more detail in chapter 2 of this thesis.

The use of ion irradiations over neutron experiments offers several advantages ranging from economic to health reasons. Neutron sources are not readily available to most users as compared to simple linear particle accelerators. Typical neutron experiments are time consuming, and it can take 1-3 years of in-core exposure to collect the desired data [Was07]. The fast turnaround times and the ability to tailor irradiation conditions at will make simulation with ion irradiation both cheaper and more flexible. Ion irradiations also provide the added advantage of being able to avoid high levels of residual radioactivity in most cases, a plus for health reasons. However, it is also important to note that some fundamental differences between interactions of ions and neutrons with target atoms may need to be taken into consideration. An example of such a difference is in the penetration depths of ions and of neutrons. While the penetration depths of ions range from ~0.1 to 100 μm depending on the ion mass and energy as well as the target material, neutrons can penetrate through to much larger depths. Details of this and other differences can be found in the text "Fundamentals of Radiation Materials Science" by G. Was [Was07]. In this PhD thesis, we have used ions of several elements which rank amongst the most radiologically significant fission products in

ion irradiation experiments to simulate in-reactor performance of SiC. These include ions of cesium, iodine, silver, strontium and xenon.

1.5 Radiation damage in SiC

Radiation damage in SiC has been the subject of many investigations over the last few decades. In the 1990s, studies by McHargue *et al*. [McH93], showed that SiC is easily amorphized by ion implantation of low energy ions in the order of a few hundred keV at room temperature irrespective of the ions implanted. They further state that the accumulation of the radiation damage is approximately linear with fluence until amorphization occurs. However, implantation of very light ions such as He^{+} results in the production of strongly disturbed but still crystalline layers in SiC [Hob97]. Wesch *et al*. [Wes95] implanted 230 keV Ga^{+} ions at various fluences and temperatures into SiC. Their investigations show that amorphisation is reached at 80 K for fluences above 1×10^{14} cm $^{-2}$. At an implantation temperature of 300 K, their studies show that amorphisation is reached for fluences between 2×10^{14} cm $^{-2}$ and 3×10^{14} cm $^{-2}$ .Wesch *et al*. also found that for implantation temperatures around 573 K, amorphisation is avoided for fluence of up to 1×10^{16} cm $^{-2}$. Higher temperatures are required to avoid damage for fluences higher than 1×10^{16} cm $^{-2}$.

On the aspect of annealing of the damage, McHargue *et al*. [McH93] found that for low damage, when an amorphous surface region is not produced, the damage anneals in the temperature range of 200°C to 1000°C. However, for the amorphous scenario, the regrowth is less clear and the ranges are from 750°C to 1700°C. Audren *et al*. [Aud07] observed that SiC is also easily amorphised by 300 keV Cs ions. At a fluence of 6 x 10^{14} cm^{-2}, their studies showed that an amorphous layer extending to a depth of approximately 150 nm below the surface was formed after implantation. Their Rutherford Backscattering combined with channeling (RBC/C) studies revealed that annealing of the damage started at around 600°C, beginning from the interface between the damaged layer and the crystalline bulk. Some appreciable recrystallization was only observed at temperatures above 960°C, with roughly 50% of the damage annealed at approximately 1300°C.

Wendler *et al*. [Wen98], implanted antimony ions to a fluence of 3 x 10^{14} cm^{-2} at energy of 300 keV. They also observed some recystallisation starting to occur at an annealing

temperature of 950°C for a period of 30 s. They reported an apparent perfect recystallisation of the amorphous layer for a 1500°C annealing cycle for 60 minutes in an argon ambient, however, they also note that the amorphous layer could have been etched away as they no longer detected the implanted ion profile after the annealing cycle. This phenomenon of thermal etching of SiC or its decomposition has recently been investigated by van der Berg *et al.* [Ber12]. Using modern high resolution scanning electron microscopy techniques, they were able to observe the evolution of the surface microstructure of single and polycrystalline SiC samples vacuum annealed in the temperature range from 1200 ºC to 1800 ºC. For single crystalline samples, thermal etching was observed from 1200 ºC while significant thermal decomposition was observed at 1800 ºC for the polycrystalline samples.

More recently our group has been characterising radiation damage produced by ions of the significant fission products produced in fuel particles of high temperature nuclear reactors. RBS and channelling studies were performed on SiC samples implanted with ions of cesium, silver, iodine, xenon and strontium. For 360 keV xenon ions (fluence of 1×10^{16} cm^{-2}) implanted at room temperature, an amorphous layer extending to a depth of 200 nm from the surface was observed [Fri14]. The amorphous layers produced by implantation of, iodine, strontium, silver and cesium ions, also of energy 360 keV, into 6H-SiC wafers, were up to depths of 220 nm, 240 nm, 260 nm and 190 nm respectively [Fri10,Fri12a,Fri09,Fri12b]. The fluence of the implanted ions was 1×10^{16} cm^{-2} for iodine, cesium and xenon ions, while a fluence of 2×10^{16} cm^{-2} was used for silver and strontium implantations. Annealing at temperatures of up to 1200 ºC resulted in very little epitaxial regrowth starting from the amorphous layer and bulk substrate interface. Similar results were obtained previously for iodine ion implantation in SiC to fluence of 2.7×10^{14} cm^{-2} Audren *et al* [Aud08]. An amorphous layer initially extending to a depth of 250 nm, showed some recystallisation on annealing at a temperature of 1000°C. Results from these studies seem to suggest that the recystallisation of the amorphous SiC starts around 900°C. Annealing temperatures ranging from 850°C to approximately 900°C are required to transform disordered Si-C bonds into the ordered 3C-SiC structure [Wes96].

The rest of the remaining previously amorphous material was simultaneously transformed into a polycrystalline layer. The near surface recystallisation behaviour into this polycrystalline layer of 6H-SiC damaged after implantation with these ions has been reported

by Kuhudzai *et al.* [Kuh14]. This work forms part of this thesis and will be explored in detail in chapter 7.

1.6 Radiological significance of chosen fission product elements

Iodine is known to accumulate in the thyroid gland. Exposure to the radioactive iodine isotopes could lead to thyroid cancer and therefore the extent to which the SiC retains the fission product iodine is essential to the development of HTGR's. There are two radio-active iodine isotopes. One of the isotopes is ^{131}I which has a half life of about 8 days. This half-life is fairly short, however, the more significant property of the isotope is its biological half life which is approximately 140 days. ^{129}I, is the other isotope and has a half-life of 15 million years. These isotopes could be produced by the following possible fission reactions:

$$^{235}\text{U} + \text{n} \rightarrow {}^{236}\text{U} \rightarrow {}^{129}\text{I} + {}^{107}\text{Y} \qquad (1.1)$$

$$^{235}\text{U} + \text{n} \rightarrow {}^{236}\text{U} \rightarrow {}^{131}\text{I} + {}^{105}\text{Y} \qquad (1.2)$$

where the uranium ^{235}U nucleus, absorbs a neutron giving rise to the highly unstable ^{236}U nucleus. The unstable uranium nucleus then undergoes fission, splitting into two fragments. In equation 1.1, the fragments are the isotopes ^{129}I of iodine and ^{107}Y of Yttrium. In equation 1.2, the resulting fragments are ^{131}I of the iodine and ^{105}Y of Yttrium.

Another important fission product element considered in this thesis is cesium. The ^{137} Cs isotope is one of the most hazardous fission product released during nuclear burn-up [Fri12b]. This isotope is a β-emmitter decaying to ^{137}Ba with a half-life of about 30 years. The cesium can enter the human body via the food chain and once there its biological half- life is 140 days in muscle tissue as well as 70 days in other parts of the body.

Strontium radioactive isotopes, ^{89} Sr with a half-life of 50.5 hours and ^{90} Sr with a half-life of 26.5 years are also some of the radiologically significant fission products [Fri12a]. They can accumulate in the human body and easily deposited in human bones due to chemical similarities with calcium.

Xenon is also one of the fission products of great significance with most of the isotopes emanating from the fission reaction being radioactive. The xenon targets the lung, bones and fatty tissue [www4]. ^{136}Xe is the longest lived isotope with a half-life of 2×10^{21} years followed by the isotope ^{127}Xe with a half-life of 36.345 days. Another isotope of xenon is ^{135}Xe with half-life of 9.5 hours. The majority of the ^{135}Xe yield comes from the decay of ^{135}I (~ 95%), while approximately 5 % fission of ^{135}Xe is from uranium [www5].

As reported in a comprehensive review by Malherbe [Mal13] and references therein, the only isotope found to escape from intact TRISO particles in significant quantities is silver ^{110m} Ag. This isotope is produced via neutron capture by ^{109} Ag. Although ^{109}Ag is a stable isotope of low fission yield (roughly 0.04 % for ^{233} U, 0.03 % for ^{235} U and 1.2 % for ^{239} Pu fission [Mal13]) and only 0.1 % of the ^{109} Ag is converted into ^{110m} Ag, the ^{110m} Ag is highly radioactive due to its high γ-ray dose rate. It also has a long half-life of 253 days.

1.7 Diffusion of fission product elements in SiC

The nuclear materials group of The University of Pretoria's Physics Department has for the most part of the last 8 years been working on a systematic study of fission product elements diffusion in SiC. This has led to several publications of the work on the diffusion of silver [Fri09], diffusion of iodine [Fri10], diffusion of strontium [Fri12a] and the diffusion of xenon [Fri14]. We have also published work on the diffusion of cesium [Fri12b]. The study of the diffusion of cesium forms part of this thesis and will be discussed in more detail in chapter 6. Other research groups have also over the years contributed to the knowledge base on the diffusion of fission product elements in SiC. Investigations by *Audren et al*. [Aud08], for 700 keV iodine ion implantation at room temperature, revealed that the iodine profile from RBS spectra does not change even after annealing up to a temperature of 1000°C for 30 minutes. 1000°C is the typical maximum temperature of the UO_2 kernel during normal operation of the HTGR. They conclude that they could not detect any diffusion of the iodine in SiC up to a temperature of 1000°C and that this would suggest that SiC could potentially be an adequate barrier to the fission product iodine. However, isotopes of the fission product iodine are known to accumulate in the primary coolant circuit during normal operation and can become significant under accident conditions [Han03]. Data on the release of the potentially

hazardous fission products has been compiled from research carried out over a period of about 40 years on prototypes of the HTGR like the Dragon reactor (UK), Peach Bottom1 (USA) and the Arbeitsgemeinschaft Versuchsreaktor, more commonly known as the AVR (Germany).

Gottaut *et al*. [Got90] carried out some experiments at the German pebble bed reactor, the AVR. They sampled coolant gas in hot and cold loops they called VAMPYR I and VAMPYR II respectively and their results revealed that significant amounts of iodine isotope ^{131}I, where present in the primary coolant gas. Specific activities of ^{131}I were in the order of 5, 2 x10^{2} Bq/m^{3}. Results from irradiation experiments on fuel elements carried out in a materials test reactor by A. Christ and W. Schenk [Chr85] are in agreement with those from the AVR experiments. Borisov *et al*. [Bo94], used carbon filters with silver nitrite to trap the fission iodine at the exit channel of the helium of their experimental apparatus. They found that radioactive iodine isotopes ^{131}I and ^{133}I produced in irradiated fuel elements were present in the helium in the form of aerosols and gas.

The diffusion behavior of silver has been a popular choice for many researchers for over 3 decades ranging from, Nabielek *et al.*[Nab 77] to Malherbe [Mal13]. In his review paper Malherbe gives a comprehensive summary of silver diffusion results to date and the reader is referred to this review for more details. In their study into the diffusion of cesium in SiC, Audren *et al.* [Aud07], observed that cesium diffusion after room temperature implantation started above 1150 ºC. A recent study into the diffusion behaviour in SiC [Kat12], has shown that while the majority of fission products studied so far are retained in intact fuel coatings, the release of cesium and silver from intact fuel coatings remains a problem. It is then essential to further explore the diffusion behaviour of cesium and silver. In this thesis, we present our findings on the diffusion of cesium in single crystalline and polycrystalline SiC. We revisit the diffusion of silver and iodine with particular emphasis on a new study into their synergistic behaviour when they are both implanted in the same wafer. We also take a close look at the surface effects after ion beam modification of the near surface region to evaluate their impact on the diffusion of fission product elements.

1.8 Outlay of this Thesis

The fact that some isotopes of the fission products have been found in the primary coolant circuit warrants further investigation of their behaviour in the main barrier layer to the fission products, namely SiC. In our work, we try to shed some light on the diffusion behaviour of implanted cesium, the diffusion of iodine and its influence on the diffusion of silver when both are co-implanted in the same wafer and annealed at temperatures above 1000°C. We also investigated the damage created by implantation of cesium at room temperature and the annealing of this damage at temperatures above 1000°C. Cesium implantations were also performed at higher temperatures (350 ºC and 600 ºC). By comparing the damage retained at these two temperatures and comparing it with the amorphised room temperature implantations, we were able to study the influence of radiation damage retained on the diffusion behaviour. Chapter 2 gives a description of ion-solid interactions with particular emphasis on ion implantation, radiation damage retained and annealing of that damage. In chapter 3, we discuss the theory of diffusion. Several techniques have been employed to characterize the behaviour of the implanted elements. These include Rutherford backscattering spectrometry (RBS) and α-particle channeling, Scanning Electron Microscopy (SEM), Atomic Force Microscopy (AFM), Atom Probe Tomography (APT), X-Ray Photo electron spectroscopy (XPS), Secondary Ion Mass Spectrometry (SIMS), Heavy Ion Elastic Recoil Detection Analysis (HI-ERDA) and Raman spectroscopy. The theory and description of these experimental techniques is given in chapter 4. Sample preparation and annealing details are outlined in chapter 5. In chapter 6, we present our results on the diffusion behaviour of cesium in SiC followed by results of the diffusion of silver, iodine and the synergistic behavior of iodine and silver when ions of both elements are implanted in the same wafer. In chapter 7 we present our results on the surface and microstructure changes of ion implanted SiC with annealing and their effect on the diffusion of the implanted ions. A summary of our findings and conclusions is presented in chapter 8 followed by a summary of our research outputs from this work in chapter 9.

References

[Aud07] A. Audren, A. Benyagoub, L. Thome and F. Garrido, Nucl. Instr and Meth. B 257 (2007) 227.

[Aud08] A. Audren, A. Benyagoub, L. Thome and F. Garrido, Nucl. Instr and Meth. B 266 (2008) 2810.

[Bra88] E. Brady and J. Holum, "Fundamentals of Chemistry" 3rd Edition John Wiley and Sons, Inc, New York, USA 1988.

[Ber10] N.G. van der Berg, J.B. Malherbe, A.J. Botha and E. Friedland, Surf. Interface Anal. 42 (2010) 1156.

[Ber12] N.G. van der Berg, J.B. Malherbe, A.J. Botha and E. Friedland, Appl. Surf. Sci 258 (2012) 5561.

[Bor94] N. Borisov, L. Borisova, B. Bylkin, S. Tsvetkov, G. Momot and A. Khulev, At. Energ. 76 (1994) 146.

[Chr85] A. Christ, W. Mehner and W. Schenk, IAEA Specialists Meeting on Fission Product Release and Transport in Gas-Cooled Reactors, Berkeley, UK (1985) 30.

[Dev00] R. Devanathan and W. Weber, J. Nucl. Mater. 278 (2000) 258.

[Eld09] R. Elder and R. Allen, Prog. Nucl. Energ. 51 (2009) 500.

[Fri09] E. Friedland, J.B. Malherbe, N.G. van der Berg, T. Hlatshwayo, A.J. Botha, E. Wendler and W. Wesch, J. Nucl. Mater. 389 (2009) 326.

[Fri10] E. Friedland, N.G. van der Berg, J.B. Malherbe, R.J. Kuhudzai, A.J. Botha, E. Wendler and W. Wesch, Nucl. Instr and Meth. B 268 (2010) 2892.

[Fri12a] E. Friedland, N.G. van der Berg, J.B. Malherbe, E. Wendler and W. Wesch, J. Nucl. Mater. 425 (2012) 205.

[Fri12b] E. Friedland, N. van der Berg, T. Hlatshwayo, R. Kuhudzai, J. Malherbe, E. Wendler and W. Wesch, Nucl. Instr and Meth. B 286 (2012) 102.

[Fri14] E. Friedland, K. Gärtner, T.T. Hlatshwayo, N.G. van der Berg and T.T. Thabethe, Nucl. Instr and Meth. B 332 (2014) 415.

[Got90] H. Gottaut and K. Kruger, Nucl. Engrg. Des. 121 (1990) 143.

[Han03] D. Hanson, "A Review of Radionuclide Release from HTGR Cores during Normal Operation", EPRI, Palo Alto, CA (2003) 1009382.

[Hob97] H. Hobert, H. Dunken, F. Seifert, R. Menzel, T. Bachmann and W. Wesch Nucl. Instrum. Meth. Phys Res B 129 (1997) 244.

[Kat12] Y. Katoh, L.L. Snead, I. Szlufarska and W.J. Weber, Current opinion in Solid State and Materials Science 16 (2012) 143.

[Kuh14] R.J. Kuhudzai ,N.G. van der Berg, J.B. Malherbe, T.T. Hlatshwayo, C.C. Theron, A.V. Buys ,A.J. Botha, E.Wendler and W. Wesch, Nucl. Instr and Meth. B 332 (2014) 251.

[Lil93] S. Lilov, Mat. Sci. Eng. B 21 (1993) 65.

[Mal08] J.B. Malherbe, E. Friedland and N.G. van der Berg, Nucl. Instr and Meth. B 266 (2008) 1373.

[Mal13] J.B. Malherbe, J. Phys. D. Appl. Phys. 46 (2013) 473001.

[McH93] C. McHargue and J. Williams, Nucl. Instr and Meth. B 80 (1993) 889.

[Moo08] R. Moormann, "Fission Product Transport and Source Terms in HTRs: Experience from AVR Pebble Bed Reactor," Science and Technology of Nuclear Installations 597491 (2008) 1.

[Nab77] H. Nabielek, P.E. Brown and P. Offermann, Nucl. Technol. 35 (1977) 483.

[Nic02] H. Nickel, H. Nabielek, G. Pott and A.W. Mehner. Nucl. Engrg. Des. 217 (2002) 14.

[Pir93] P. Pirouz and J.W. Yang, Ultramicroscopy. 51 (1993) 189.

[Sch90] W. Schenk, G. Pott and H. Nabielek, J. Nucl. Mater. 171 (1990) 19.

[Soh06] R. Sohal, "CVD Growth of (001) and (111) 3C-SiC Epilayers and Their Interface Reactivity with Praseoydmium Oxide Dielectric layers" PhD Thesis, Brandenburgische Technische Universität Cottbus, 2006, p.27.

[Sne07] L. Snead, T. Nozawa, Y. Katoh, T. Byun, S. Kondo and D. Petti, J. Nucl. Mater. 371 (2007) 329.

[Yua02] L. Yuanzhong and C. Jianzhu, Nucl. Engrg. Des. 218 (2002) 81.

[Wan08] J. Wang, "Developing a High Thermal Conductivity Nuclear Fuel with Silicon Carbide Additives" PhD Thesis, University of Florida, 2008, p.22.

[Was07] G. Was, "Fundamentals of Radiation Materials Science, Metals and Alloys", Springer, Berlin 2007.

[Wen98] E. Wendler, A. Heft and W. Wesch, Nucl. Instr and Meth. B 141 (1998) 105.

[Wes95] W. Wesch, A. Heft, E. Wendler, T. Bachmann and E. Glaser, Nucl. Instr and Meth. B 96 (1995) 335.

[Wes96] W. Wesch, Nucl. Instr and Meth. B 116 (1996) 305.

[Wol05] M. Wolborski, "Termination and Passivation of Silicon Carbide Devices", Licentiate Thesis, Royal Institute of Technology (KTH), Department of Microelectronics and Information Technology, 2005, p.5.

[www1] http://www.iaea.org/NuclearPower/Downloads//2.4SouthAfricapdf (accessed12-06-2014).

[www2] http://www.iaea.org/NuclearPower/Downloads/03.Niasapdf(accessed12-06-2014).

[www3] http://www.pbmr.co.za. (accessed 09-02-2010).

[www4] http://www.lantheus.com/PDF/msds/XenonLantheusComplete.PDF,20 (accessed June 2012).

[www5] http://en.wikipedia.org/wiki/Iodine_pit (accessed 12 December 2012).

[Zso05] Z. Zolnai, "Irradiation-induced Crystal Defects in Silicon Carbide", PhD Thesis, BUTE-DAP, Department of Atomic Physics, 2005, p.4.

Chapter 2

Ion solid interactions: Ion implantation, production of radiation damage and annealing of damage.

Introduction

Ion implantation is regarded as the main technique used to introduce controlled concentrations of impurities into solids. Atoms from the desired material are ionized, then accelerated and directed towards a target. The kinetic energy of the ions enables them to penetrate into the lattice of the target material. Energetic particles impinging on a target, penetrating into it until they come to rest somewhere within the target are said to have been implanted. During these ion-solid interactions, ions gradually lose energy when they interact with target atoms as they move through the solid until they stop at a certain depth within the solid.

A variety of other processes can also take place during interactions between projectile ions and solid targets [Gna99]. Some target materials are of a crystalline nature, meaning that their constituent atoms are positioned at specific points known as lattice sites in periodic arrays leading to long range order [Cal07]. Implantation into such materials may result in target atoms being temporarily or permanently displaced from their original lattice sites leading to the formation and accumulation of defects in the target. Accumulation of the defects can lead to the total loss of this systematic and regular arrangement of the atoms and this absence of long range order is known as the amorphous state [Cal07]. Incident ions may also supply target atoms close to the surface with enough energy to overcome the surface potential barrier and escape from the target. This emission of surface atoms on impact of energetic particles is known as sputtering [Hof76,Cal07]. A term known as the sputter yield, defined as the mean number of atoms removed from the target surface per unit incident ion is used to quantify the surface erosion [Beh83]. The sputter yield depends on the target material, the experimental geometry, ion species and ion energy of the incident ion beam [Fel86]. An excellent review of the sputtering of compound semiconductor surfaces is given by Malherbe [Mal94].

2.1 Energy loss of ions in solids

There are two major processes which result in the incident ions losing energy when energetic ions enter a solid. The ions lose energy when they undergo elastic collisions with lattice atoms and the ions also lose energy in inelastic interactions with electrons in the solid in which the electrons are excited. These processes are referred to as nuclear energy loss and electronic energy loss respectively. The two processes are generally viewed as being independent from each other [Wil73].

In nuclear stopping, elastic coulomb interactions between the nuclei of the ion and target atom result in relatively large amounts of energy and momentum transfer. This leads to significant changes in ion's direction as well as displacements of target atoms from their lattice positions. Nuclear stopping depends on the distance of closest approach of the ion to the target atom as the interaction potentials are strongly dependant on the distance separating the two nuclei. In the case of electronic stopping, the collisions are characterized by relatively small amounts of energy and momentum transfer due to the small electron mass. For such collisions, deflections of the ions will be negligible.

The average energy loss per unit length of penetration into a homogenous medium by a charged particle or projectile is the quantity most often referred to as the stopping power of the medium [Kam84]. The total stopping power for an ion coming to rest at a depth x below the target surface [Dea73] is given by

$$-\frac{dE}{dx} = N[S_n(E) + S_e(E)] \qquad (2.1)$$

where N is the atomic density of the target, $S_n(E)$ and $S_e(E)$ the nuclear and electronic stopping powers respectively. The total stopping cross section (ε) can be calculated by dividing the total stopping power by the target density N and are therefore defined by:

$$\varepsilon = -\left(\frac{1}{N}\right)\left(\frac{dE}{dx}\right) \qquad (2.2)$$

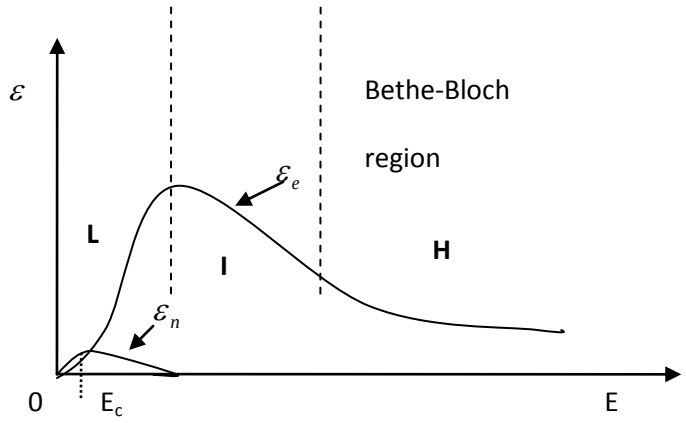

Figure 2.1: The nuclear ε_n and electronic ε_e stopping cross sections as a function of the ion energy E. E_c is the critical energy where the contributions of nuclear and electronic cross sections are the same. Also shown are the 3 energy regions L, the low energy region where $v_1 < v_0 z^{2/3}$, the intermediate region I, where $v_1 \approx v_0 z^{2/3}$ and the high energy region H, where $v_1 >> v_0 z^{2/3}$ .v_1 is the velocity of the ion and v_0 is the Bohr velocity and z is the atomic number of the ion. Redrawn from reference [Was07].

The stopping power is greatly influenced by the ion energy *E*. At low energies, nuclear stopping is the dominant mechanism. At higher energies nuclear stopping is overtaken by electronic stopping which then dominates. This shift in the dominant energy loss mechanism is shown in figure 2.1. It is clearly observed in the figure that electronic stopping begins to dominate above the critical energy E_c. The electronic stopping then reaches a maximum and then decreases again towards the high energy region described by the Bethe-Bloch equation [Bet30] where the ion has a shorter time to interact with the target atoms at the high ion velocities. The mechanisms of electronic and nuclear stopping are discussed in more detail in sections 2.1.1 and 2.1.2.

2.1.1. Electronic Stopping

In this energy loss mechanism, energetic ions penetrating a material lose their energy via inelastic interactions with target electrons. A number of processes facilitate this transfer of kinetic energy from the incident ion to the target electrons [Zie85]. These include electron-electron collisions, excitation or ionization of target atoms and excitation, ionization or electron–capture of the incident ion.

A model based on the ion velocity is used to describe the energy loss process. The basis of which arises from comparing the ion's velocity with the Bohr velocity $v_0 = e^2/\hbar$. Here, e and $\hbar$ are the electron charge and the Planck's constant $h/2\pi$ respectively. The first part of the model deals with the low energy region (L in figure 2.1) where the ion's velocity v_1 is such that $v_1 < v_0 z^{2/3}$. z here is the atomic number of the ion . $v_0 z^{2/3}$ for cesium ions is 3.16 × 10 ^{9} cm/s. At 360 keV, cesium ions have an initial velocity of 7.2 × 10 ^{7} cm/s which is less than $v_0 z^{2/3}$. At these ion velocities, the ion cannot transfer sufficient energy to electrons that are far lower in energy than the Fermi level. As a result only electrons in energy levels close to the Fermi level are involved in the inelastic energy loss process. In calculating the electronic stopping for this low energy region, a free electron gas with a density ρ is assumed [Lin53, Lin61]. The electronic stopping cross section ε_e of an ion with Z_1 is then [Zie88]:

$$\varepsilon_e = \int I(v,\rho)(Z_1(v))^2 \rho dV \qquad (2.3)$$

where I is the stopping interaction function of an ion of unit charge with velocity v, ρ is the electron density of each volume element the target dV, $Z_1(v)$ shows that the charge state of the ion is velocity dependant as the stripping of its electrons depends on its velocity. The integral is performed over each volume element of the target dV.

The second region of the model deals with the so-called intermediate region where the ions velocity v_1 is such that $v_1 \approx v_0 z^{2/3}$. In this energy region, the ion is partly ionized and the electronic stopping reaches it maximum (figure 2.1).

Very high velocities where the ion's velocity is now given by the condition $v_1 >> v_0 z^{2/3}$ make up the third region in the model and this region is described by the Bethe-Bloch equation [Boh13, Bet30, Blo33, Kam84]. The Bethe-Bloch equation shows that the energy loss in this case is proportional to $Z_1{}^2$ as given in equation 2.4 below.

$$\varepsilon_e = \frac{4\pi Z_1^2 Z_2 e^4}{m_e v_1^2}\left[\ln\frac{2m_e v_1^2}{I} - \ln(1-\beta^2) - \beta^2 - \frac{C}{Z_2} - \frac{\delta}{2}\right] \qquad (2.4)$$

where m_e is the mass of the electron, v_1 the velocity of the projectile, Z_2 is the mass of the target atom, $\beta = v/c$, c being the speed of light and C/Z_2 is the shell correction to compensate for the lower contribution to the stopping power of electrons in the inner shells. $\delta/2$ is the

density effect correction at very high kinetic energies to account for the decrease in stopping power due to dielectric polarization of the stopping medium. I is the mean excitation energy defined as [Kam84]:

$$\ln I = \sum_n f_n \ln(E_n - E_0) \tag{2.5}$$

where f_n is the dipole oscillator strength for transitions from the ground state E_0 to energy state E_n. Many models have been used estimate I. A common approximation for I is given by Block's rule [Bloc33]:

$$I=10Z_2 \text{ in eV} \tag{2.6}$$

For the work presented in this thesis, we are interested in the low and intermediate energy regimes. The low energy regime for the implantation of 360 keV ions and the intermediate energy regime for the ion beam analysis technique Rutherford backscattering spectroscopy (RBS) in which we use 1.6 MeV alpha particles.

2.1.2. Nuclear Stopping

As the projectile ion penetrates through the solid, the interaction between the incident ion and a target atom is taken to be isolated from the rest of the target atoms. This assumption allows the ion scattering and energy transfer to be treated as a simple two-body collision event. Nuclear scattering can then be described by the potential between the ion and the target electrons. There are many interatomic potentials that have been suggested over the years in literature [Gna99] and generally take the form of the screened coulomb potential given in equation 2.7 below.

$$V(r) = \frac{Z_1 Z_2 e^2}{r} \phi\left(\frac{r}{a}\right) \tag{2.7}$$

where Z_1 and Z_2 are the atomic numbers of the ion and target respectively, e is the electron charge, r is the interatomic distance and $\phi\left(\frac{r}{a}\right)$ is a screening function depending on the electron density distribution in the two atoms [Gna99]. The interatomic potentials for a number of atomic pairs have been calculated using the Hartree-Fock Methods [Zie85].

The collision between the incident ion of mass M_1 and target atom of mass M_2 results in the transfer of kinetic energy T. This transfer obtained from the conservation of energy and momentum, is a function of the masses of the ion and target atom along with the projectile energy E_0 and the scattering angle α in the centre of mass system [Tow94, Fri01] as shown in equation 2.10.

$$T = E_0 \frac{4M_1M_2}{(M_1 + M_2)^2} \sin^2(\frac{\alpha}{2}) \qquad (2.8)$$

The scattering angle (α) in equation 2.8 can be calculated as a function of collision parameter b for a given potential such as the one given in equation 2.7.

For an incident ion penetrating through an amorphous target having a density of N atoms/unit volume, and during its movement through a slab of the target material of thickness dx, (figure 2.2), the number of atoms with collision parameters in an interval db is given by [Was07].

$$dn(b) = Ndx2\pi bdb \qquad (2.9)$$

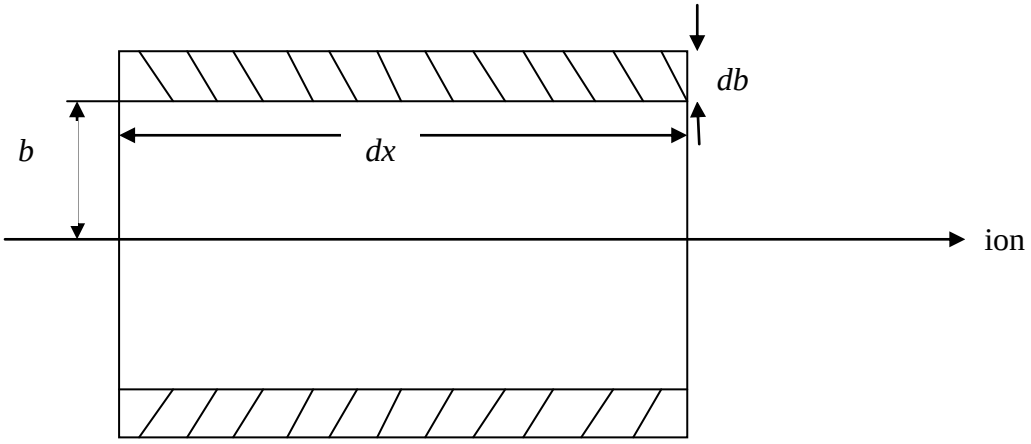

Figure 2.2: Schematic of an incident projectile of energy E passing within a distance b of an annular ring containing $Ndx2\pi bdb$ atoms. b here is a collision parameter [Redrawn fromWas07].

The projectile will transfer energy T which is a function of the collision parameter b (T(b)) to each target atom. The total energy transferred to the target atoms in the slab is then the integral over all the collision parameters. The total energy loss is then

$$-\frac{dE}{dx} = N2\pi\int_0^{b_{max}} bT(b)db = NS_n \tag{2.10}$$

The nuclear energy loss (ε_n) is then found by dividing (2.10) by N as stated in section 2.1.

$$\varepsilon_n = 2\pi\int_0^{b\,max} bT(b)db \tag{2.11}$$

2.1.3. Energy loss in compounds

Our work in this thesis revolves around silicon carbide. In dealing with the energy loss processes, we are therefore interested in the energy loss behaviour in multi element targets or compounds. In such targets, collisions are still considered to be independent encounters taking place one at a time. The collisions are distributed among the various elements and weighted proportionally to the elemental distribution of the compound. This is known as the Bragg rule [Bra05]. For a compound with composition A_mB_n, the stopping cross section $\varepsilon^{A_mB_n}$ is then:

$$\varepsilon^{A_mB_n} = m\varepsilon^A + n\varepsilon^B \tag{2.12}$$

where A and B are the elements in the compound and m and n are the relative molar fractions of the compound.

Deviations from this Bragg rule have been found experimentally. This is due to the fact that the rule assumes that the projectile ion-target atom interaction is independent of the environment [Tes95]. However, during the interactions, the chemical and physical state of the medium, influence the energy loss. Marked deviations from the Bragg rule, in the order of 10%-20% around the stopping maximum have been observed. Such cases involved light organic gasses, as well as solid compounds in which there are large differences between the atomic masses of the constituents such as in the case of oxides and nitrides of heavy metals [Tes95]. Ziegler and Manoyan [Zie88], developed the ‘Cores and Bonds’ model (CAB) to accommodate the chemical state effects. In this model for the stopping of ions in compounds, it is assumed that two contributions are involved. These are the effects of the non-bonding closed shell ‘core’ electrons and the bonding valence electrons. If the bond structure of a compound is known, the CAB correction can be determined.

2.1.4. Energy Straggling

An energetic particle moving through a medium loses energy via many individual interactions with the medium's atoms. The discreteness of such interactions leads to statistical fluctuations. Identical energetic particles initially having the same energy when entering the medium will not have the same energy after traversing the same thickness (x) of the same medium. This phenomenon is known as straggling [Fel86].

For electronic energy loss where the energy loss process is subject to statistical fluctuations of the electronic interactions, the straggling has been derived from the Bloch-Bethe equation [Boh48, Zie85, Fel86]. This so-called Bohr straggling, Ω_B^2, is given by:

$$\Omega_B^2 = 4\pi Z_1^2 Z_2 e^4 N x \qquad (2.13)$$

Here, Ω_B^2 is the variance of the average energy loss of a projectile travelling through a target thickness x. The distribution of energy loss for many independent collisions is approximately Gaussian when the energy loss is small compared to the incident energy [Fel86]. The full width at half maximum (FWHM) of the energy loss distribution is then given by $2\Omega_B\sqrt{2\ln 2}$. This Bohr theory of straggling has since been extended to include corrections for energies where earlier assumptions may not be valid. Some of these extended models include works by [Lin53] and [Chu76]. In compound targets, the total energy straggling is through a similar linear additivity rule to the Bragg's rule for energy loss [Chu76. Tes95].

2.1.5. Range of implanted ions

The penetration length of ions with initial incident energy E_0 known as the range, R, of ions moving through a target medium of atomic density N, is given by equation 2.14 [Gib75] below.

$$R = \frac{1}{N}\int_0^{E_0} \frac{dE}{(dE/dx)} \qquad (2.14)$$

The standard practice when dealing with penetration depths of ions into targets is to consider the projection of the distance travelled into the medium by an ion (the range R of the ion)

onto the direction of incidence. This projection is referred to as the projected range R_P of the ion (figure 2.3).

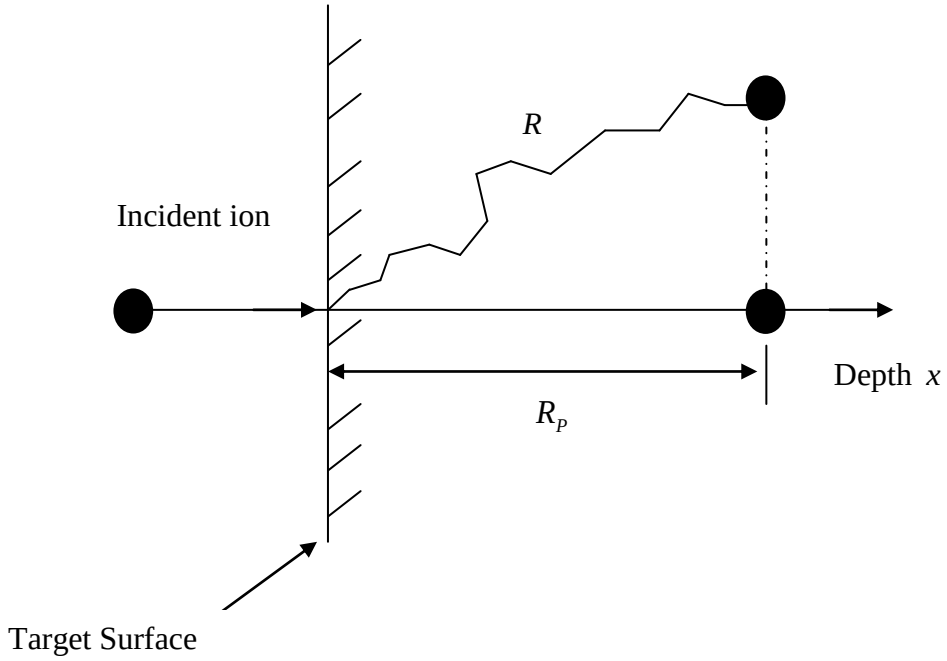

Figure 2.3: The projected range R_P and the total range R for an incident ion on a target.

In the case of multiple ions impinging on a target, the mean value of the projections of the individual total ranges of ions on the initial direction of the beam path gives the R_P of the distribution of ions in the medium. ΔR_P here is the standard deviation of the projected range and is known as the range straggle.

2.2. Ion Channeling

When the target medium is a crystal, the open spaces between close packed rows of atoms or planes of atoms (channels) may result in the incident energetic ions being steered along these open paths. This steering/guiding of the projectile ions is known as channelling. The channelling of ions is due to a series of correlated small angle and thus gentle screened Coulomb scatterings between the incident ion and the atoms bordering the channel. Channelled ions do not penetrate closer than the screening radius of the vibrating ions of target reducing the probability of large angle backscattering collisions [Tes95]. Ions incident well aligned with the open channels of the crystal only suffer smooth collisions with very little deviation from their original direction. The energy loss per unit

length is then reduced and the ions experience enhanced penetration into the crystal [Gro84]. Poorly aligned ions and ions incident in random directions experience large angle scattering. This results in an increase in the proportion ions that are scattered back. The cross section of events that require close collisions with atoms is greatly reduced during channeling. Examples of such events include X-ray production, nuclear reactions and Rutherford backscattering. For this channeling to occur, the angle of incidence of the ions must be smaller than a certain critical angle, ψ_0 .This condition will ensure that the ions are reflected away from the row of atoms continuously by the correlated series of the many consecutive glancing angle collisions with the atoms in the row. The critical angle is given by [Gem74]:

$$\psi_0 = \left(2Z_1 Z_2 e^2 / Ed\right)^{1/2} \tag{2.15}$$

where E is the incident ion energy, d is the inter atomic spacing along the axial direction, Z_1 and Z_2 are the atomic numbers of the ion and target respectively. Lindhard, [Lin65], showed that for ions incident below the critical angle, the ions move in a transverse potential, which arises from an averaging of the potential of each atom in the string or row of atoms. This so-called continuum potential is given by [Bir89]:

$$U(r) = \frac{1}{d}\int_{-\infty}^{\infty} V\left[\left(z^2 + r^2\right)^{1/2}\right] dz \tag{2.16}$$

here, V is the interatomic potential and d , r and z are defined in figure 2.4 as shown below

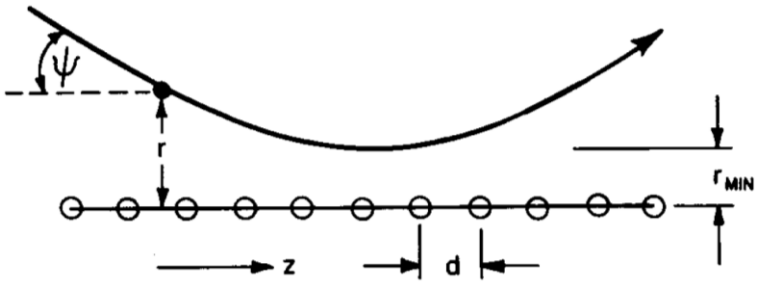

Figure 2.4: Ion scattering from an axial string of atoms. Taken from [Bir89].

Above this critical angle [Gem74], the particles begin to approach the row of atoms so closely that the particles will start to feel effect the atoms in the row individually. The particles will then experience large angle scattering and will be dechanneled. The probing of

targets by ion channeling of ion beams is a useful technique in materials science analysis for analysis of defects in solids as the channeled fraction of incident beam is sensitive to any irregularities in crystal structure. The use of channeling in this regard will be discussed in more detail in chapter 4.

2.3 The distribution of implanted ions

The distribution of the implanted ions with depth into the target medium is dependent on several factors. These include the incident ion's energy, mass, nuclear charge, the target atom's mass, nuclear charge and atomic density of target. Other important factors include the crystallinity of the target, temperature of the target and the ion fluence of implanted ions [Gib75]. Here ion fluence is defined as the number of implanted ions per unit area. In crystalline targets, the final profile of implanted ions may be influenced by channeling effects resulting in deeper penetration of ions. At very low energies, ions penetrate only up to a few atomic spacings. At very high fluences, the ions are subjected to an increased stopping power from the target due to the contribution of the preceding implanted ions. This also results in shallower penetration of the latter ions. In defective crystals where some lattice sites are unoccupied (vacancies), the distribution can be influenced by enhanced transport of the implanted ions via a vacancy assisted diffusion mechanism [Wil73]. For amorphous targets, the statistical nature of the ion-target atom collisions means that the incident ions will stop with an approximately Gaussian distribution inside the target at a depth dependent on the incident ion energy. Range theory [Lin63] generally approximates the target to be amorphous. Experimentally, minimizing channeling effects during ion implantation ensures that the random scattering needed to obtain the desired implantation profile which is approximately Gaussian in crystalline targets takes place. Several techniques can be implemented to minimize channeling effects in crystalline materials. These include pre-amorphisation of the target with inert ions and mis-orientation of the beam direction with respect to all crystal axes [Wil73]. In this study, ion implantation of silicon carbide wafers was carried out with the ion beam 7 º off normal incidence to minimize channeling effects.

In this thesis we have used the Genplot program [www1] to fit the implanted profiles before and after annealing to an Edgeworth distribution to obtain the first four moments of the implanted ion distributions. These moments are the projected range (R_p), the straggling (σ),

the skewness (γ) and the kurtosis (β). The skewness gives a measure of the asymmetry of a distribution while the kurtosis gives a measure of how peaked or flat the profile is compared to a Gaussian distribution. For a Gaussian distribution γ=0 and β=3. The Edgeworth distribution is given in equation 2.17 below:

$f(x)=g(x)p(x)$ 2.17

where $g(x) = \frac{h}{\sqrt{2\pi}} \exp(\frac{-\arg(x)}{2}$,

$$p(x) = 1 + \frac{\gamma \arg(x)^3 - 3\arg(x)}{6} + \frac{(\beta - 3)(\arg(x)^4 - 6\arg(x)^2 + 3}{24}$$

with $\arg(x) = \frac{(x - R_P)}{\sigma}$

h in $g(x)$ is a height fitting parameter. Mathematically the four moments can be expressed as

$$R_P = \frac{\sum_i x_i}{N}, \sigma = \left[\frac{\sum_i x_i - R_P}{N}\right]^{\frac{1}{2}}, \gamma = \frac{\sum_i (x_i - R_P)^3}{N\sigma^3} and \beta = \frac{\sum (x_i - R_P)^4}{N\sigma^4}$$

2.4. Radiation damage

The collisions encountered by an energetic ion or atom as it moves through a solid result in energy being transferred to the atoms of the solid. When this transferred energy is large enough to break the interatomic bonding, the atom may be permanently displaced from its lattice site [Kin55]. The amount of energy required to displace the atom permanently from its original lattice site is known as the displacement energy. If the energy transferred is smaller than the displacement energy, the target atoms will simply continue to vibrate about their lattice positions. In silicon carbide, the displacement energies for silicon and carbon are 35 eV and 20 eV respectively [Dev01].

2.4.1. Point defects and extended defects

The simplest irregularities or disturbances to the regular ordered arrangement of a crystal lattice introduced to the target by the impinging energetic ions when the energy transferred is

just greater than the displacement energy are the displacements around a single lattice point or site. These defects are therefore called point defects or primary defects. A dislodged atom leaves behind an unoccupied lattice site. This unoccupied site is called a vacancy. The dislodged atom may then position itself in between lattice sites in a position know as an interstitial position. Point defects can react with each other. Defects of opposite types recombine and annihilation of the defects follows. Defects of the same kind can combine to form clusters of defects. The clusters can grow even larger by absorbing similar defects. These defects of larger dimensions are known as extended or secondary defects. Examples of extended defects include voids (conglomeration of vacancies), dislocation loops and amorphous zones.

Energies used in ion implantation (360 keV ions in our case), cause large energy and momentum transfers such that the displaced target atoms may recoil with enough energy to displace further lattice atoms. Although the entire collision sequence lasts for approximately 10^{-11} s [Wil98], the primary knock on atom produces many displacements before all of its energy is dissipated. This knock-on effect may result in a collision cascade. A collision cascade is defined as a spatial cluster of lattice vacancies and atoms in interstitial positions within a localised region of a lattice due to a single primary knock-on atom [Was07]. For small cascades, the collisions are taken as separate binary events. Large energy transfers can lead to high density cascades known as spikes [Mal94,Was07]. One way of describing a spike is defining it as a local volume in which the local defect density produced by the incident ion exceeds some critical value such that the lattice experiences significant rearrangement to accommodate the defects [Mal94]. An example of such a rearrangement could be the crystalline to amorphous transition.

2.4.2 Amorphisation

Room temperature ion implantation even at low energies is known to easily induce amorphisation in silicon carbide [McH93, Wen98]. Amorphisation is readily achieved in the case of SiC due to the predominantly covalent nature of the carbon-silicon bonding. As in most covalent solids, the crystal structure of SiC is such that nearest neighbours to each atom are arranged in a regular tetrahedron with each bond containing two electrons [Yas04]. The nature of bonding in materials is one criterion that has been successfully used to predict the susceptibility of materials to amorphize under irradiation conditions [Nag75]. Radiation

sensitivity was adjudged to depend on the iconicity of the material. Setting unity as fully ionic and zero as fully covalent, substances having ionicities ≤ 0.47 have tend to amorphize under ion irradiation [Phi70,Nag75]. The calculated value of the ionicity of SiC was found to be approximately 0.18 [Nag75]. This value being well below 0.47, supports the case of its readiness to amorphize on ion impact.

The critical deposited damage energy of the alpha phase (hexagonal structure) of SiC had been found to range from 16 to 20 eV/atom while that of the beta phase (cubic type) is nearer to 25 eV /atom [McH93]. Later, P Musumeci *et al*. [Mus96], found the critical energy density for amorphisation to be around 23 eV/atom for 6H-SiC independent of the ion implanted. The general consensus attributes the amorphisation phenomenon to two possible models:

i. The critical accumulation model also described as the homogenous model [Voo69,Swa71, Voo73,Cha71], and

ii. The cascade overlap model (heterogeneous model) [Mor70].

2.4.3. Homogenous and Heterogeneous models for amorphisation

In the critical accumulation model, point defects or other defects build up homogeneously throughout a certain volume until a critical density of defects has been attained. When this critical defect density is attained, spontaneous amorphisation then follows. Amorphisation occurs due to the fact that the free energy of the highly damaged but still partly crystalline material becomes larger than the free energy of the amorphous material. The homogenous model is usually associated with the implantation of light ions. Lighter ions have lower scattering cross-sections. The energy deposition is lower than that of heavy ions along the ion track leading to damage which is sparingly distributed. Amorphisation in SiC which can be attributed to this model has been observed by transmission electron microscopy (TEM) for irradiations with 2 MeV electrons of α-SiC [Inu90], β-SiC [Inu92] and RBS-C studies of 155 keV $^{23}Na^{+}$ (Fluence~10^{16}) implanted SiC [Bol95].

Impinging ions may generate locally amorphised zones within the material. As the ion fluence increases, the amorphous zone accumulate up to a point where they eventually overlap producing a continuous amorphous layer [Mor70]. This is known as heterogeneous amorphisation or the overlap model. Amorphisation due to cascade overlap is usually associated with bombardment using heavy ions. Heavy ions have larger scattering cross

sections as compared to lighter ions. Heavy ions are thus more likely to undergo collisions. With the mean free path (λ) [Was07,Wer06] for energetic ions dependant on the inverse of the atomic density (N) of the target and the scattering cross section (σ), the larger scattering cross section for heavy ions result in shorter mean free paths.

$$\lambda = \frac{1}{N\sigma} \tag{2.18}$$

Heavy ions therefore cause high energy deposition densities leading to collision cascades and amorphous zones which eventually overlap depending on fluence. The width of the amorphous layer produced on ion implantation also depends on the energy of the incident ions. Amorphisation via the heterogeneous model has been observed for high resolution transmission microscopy studies for 1.5 MeV Xe^{+} [Web95, Web96].

2.4.4. Amorphisation: Fluence dependence

The ion fluence of the implantation process has an effect on the extent of damage produced in bombarded materials. For low fluences $\leq 10^{13}$ ions/cm^2, damage is limited to the formation of point defects and defect clusters which include dislocation loops, stacking faults and amorphous zones [Nag1975]. Naguib and Kelly, [Nag 1975] also state that for intermediate or medium fluences (10^{13} - 10^{16} ions/cm^{-2}), damage can result in amorphisation and stoichiometric changes. Experimental work carried out by our group (Rutherford backscattering studies RBS) [Kuh10] also shows amorphisation of the near surface region by ion implantation of iodine ions in the medium (10^{16} ions/cm^{-2}) fluence range as shown in figure 2.5. In figure 2.5, the backscattered yield of the channelled spectra (black curve) initially reaches the level of the random yield of backscattered particles (blue curve) indicating a high level of defect concentration due to amorphisation of the near surface region. The amorphous layer in this case extended to a depth of approximately 220 nm. The energy of the iodine ions was 360 keV. Similar observations have been found for room temperature ion implantation of strontium and silver ions, also of energy 360 keV, into 6H-SiC wafers. The amorphous layers produced by implantation were up to depths of 240 nm, 260 nm respectively [Fri12,Fri09].

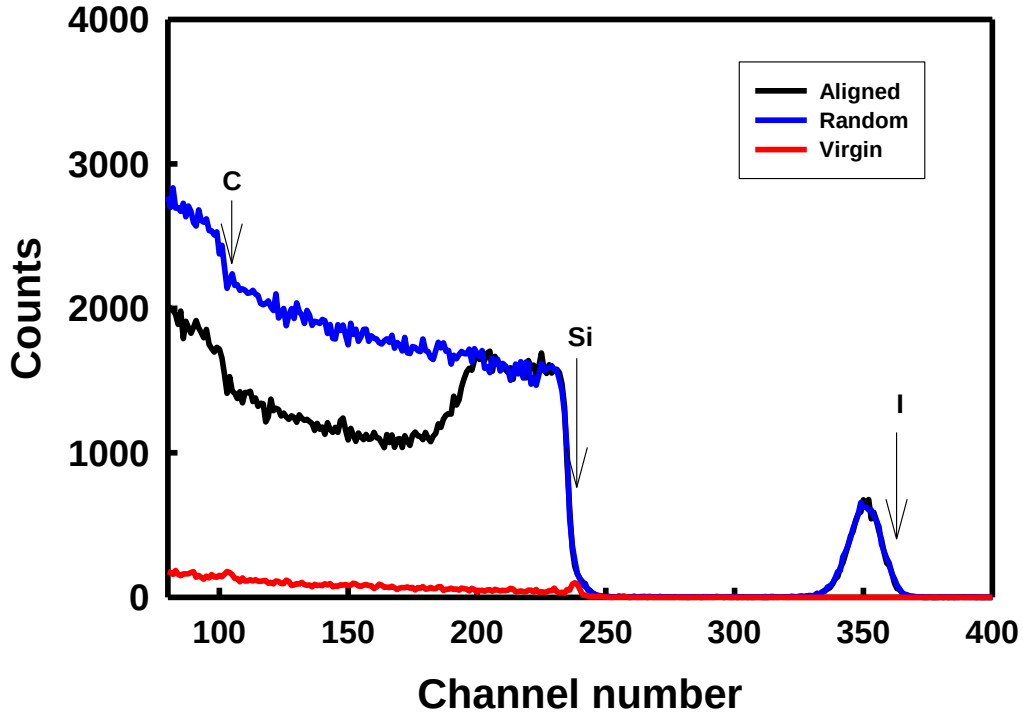

Figure 2.5: Random and aligned backscattering spectra of 6H-SiC implanted at room temperature with 360 keV $^{127}I^{+}$ ions to a fluence of 1 x10^{16} cm^{-2}. The α-particle energy was 1.6 MeV and a scattering angle of 165° was used. The arrows indicate the scattering from the surface of each element.

In addition to the amorphisation of the medium, high fluence regimes (≥ 10^{17} ions/cm^2) result in topographical changes such as facets, grooves, steps and cones due to sputtering [Nag1975, Wei96].

2.4.5. Armophisation: Temperature dependence

A strong temperature dependence of radiation damage retained during ion implantation has also been established. The temperature dependence of the amorphisation of the target medium is due to thermally enhanced annealing of generated defects within the primary collision cascade with increasing substrate temperature [Wen98]. Higher implantation fluences are then needed to induce amorphisation with increasing temperature. There are some models to describe this temperature dependence [Mor70,Web94,Web94(2)]. In general, the temperature dependence can be attributed to the simultaneous damage recovery process with an activation energy E_a, which decreases the average defect density produced

per particle [Web96]. This results in the decrease of the rate at which the amorphous fraction f_a accumulates. A general equation [Web96], is used to give the relationship between the temperature and the fluence required for complete amorphisation and is given in eqn (2.19) [Web96].

$$\ln\left[1-(D_0/D)^m\right]=C-E_a/kT \qquad (2.19)$$

where D is the implantation fluence,D_0 is the fluence for complete amorphisation at 0 K, C, is a constant which depends on the ion flux and damage cross section and k is the Boltzman constant. Several values for m have been used by different authors, m=1[Web96] and m=1/2 or 1/3 [Mor70].

As the implantation fluence D approaches infinity, ln(1-D_0/D) approaches 0, and eqn (2.19) yields an expression for the critical temperature above which amorphisation does not occur [Web96].

$$T_c = E_a/kC \qquad (2.20)$$

Wendler *et al*. [Wen98], give a summary of the critical temperatures T_c for ion and electron irradiation in SiC obtained by several authors. By fitting these results, Wendler *et al*. found that the critical temperature T_c for ion bombardment is given by:

$$T_c = \frac{A}{B-\ln(jE_r^2)} \qquad (2.21)$$

where A and B are material dependant constants, j is the dose rate and E_r is the average energy transferred to recoils per ion and unit depth.

A good account of this temperature dependence is given by Wesch *et al*. [Wes95]. They investigated the damage production in 6H-SiC by ion implantation of Ga and Sb ions in the temperature region between 80 K and 1473 K. Rutherford backscattering combined with channeling studies by Wesch *et al*. for Ga implantation (230 keV ions) showed that:

i. at 80 K amorphisation is achieved for doses above 1×10^{14} cm $^{-2}$

ii. at 300 K amorphisation is achieved in the range 2×10^{14} cm $^{-2}$ – 3×10^{14} cm $^{-2}$

iii. at 433 K the dose required for amorphisation goes up to approximately 5×10^{14} cm $^{-2}$

iv. at 573 K , however, amorphisation is avoided for doses up to 1×10^{16} cm $^{-2}$

From results, it can clearly be seen that the higher the implantation fluence, the higher also the temperature required to avoid or reduce the extent of radiation damage. Their work also investigated the effect of implantation temperature on damage retained using a particular fluence. For a fluence of approximately 1×10^{15} Sb^{+} cm^{-2} (300keV), maximum damage was realised up to 300 K. The thickness of the amorphous layer extended up to a depth of 150 nm from the surface. Increase in implantation temperature initially sees the crystalline to amorphous interface slightly shifting towards the surface without the backscattering yield in the remaining area subsiding. Further increase in implantation temperature in the range 673 K to 873 K reveals a significant drop in the backscattering yield where it no longer reaches the random level. However a residual damage peak still remains indicating some defects still remain. These results show that for higher implantation temperatures (above 500 k) residual damage due to ion implantation is influenced strongly by defect recombination, defect transformation and defect out diffusion from the damaged region.

2.5. Structure of amorphous SiC

Over the years many researchers have investigated the atomistic nature of amorphous SiC using a wide range of techniques [Ish02]. From these works, two atomistic structural models for amorphous SiC dependant on ion fluence of implantation have been proposed. In one model, amorphous SiC as investigated by Raman Spectroscopy [Bol95,Bol97, Mel00, Mus01,Ser96] consists of heteronuclear Si-C bonds as well as homonuclear Si-Si and C-C bonds. This type of amorphous structure [Bol95], was produced for the ion fluences in the order of 10^{16} cm^{-2} for 155 keV $^{23}Na^{+}$ into SiC at approximately 90 K. The presence of both homonuclear and heteronuclear bonds in amorphous SiC was also confirmed by electron diffraction for room temperature implantations with 150 keV Ar^{+} ions (10^{16} cm^{-2}) [Ish02]. In the second model, described for lower ion fluences, (10^{14} cm^{-2} - 10^{15} cm^{-2}) for sodium ion implantation and 2×10^{15} cm^{-2} Cr^{+} implantation at 280 keV at room temperature [Bol97], no decomposition of the Si-C bond was found and only the heterogeneous Si-C bond was detected from Raman measurements [Bol95]. The amorphous structure which had been confirmed by other techniques (RBS and Transmission electron Microscopy TEM) formed due to bond angle and bond length distortions [Bol95]. Several authors have also found

amorphous silicon carbide to be composed of highly disordered heteronuclear Si-C bonds [Ben89, Kal88,Tak92,].

2.6 Annealing of Radiation Damage

The annealing behaviour of amorphous SiC produced by room temperature ion implantation depends on the structure of the amorphous SiC (discussed in section 2.5 above) and the impurity concentration [Bae04,Pac96]. Investigations by Pacaud *et al*. [Pac96] suggest that the onset of this epitaxial recystallisation in SiC is around 1000 °C. Other studies [Höf99,Sat01], suggest epitaxial regrowth of implantation induced amorphous silicon carbide starts at approximately 800 ºC. Epitaxial regrowth here refers to the recrystallization of the overlaying damaged layer into a crystalline state whose form is determined by the orientation of the underlying crystal [Poa78]. Therefore any epitaxial recrystallization taking place starts at the interface between amorphous surface layer and the crystalline bulk of the single crystal. For an amorphous network generated by low ion fluences (10^{14}-10^{15} cm^{-2}), full epitaxial recrystallization has been observed using Transmission Electron Microscopy (TEM) [Bae04] for 150 keV Xe (10^{15} cm^{-2}) implantation SiC annealed at 890 ºC for 2 hours. For higher fluences, full epitaxial recrystallization is inhibited by nature of the amorphous structure produced after implantation [Bol97,Bae04] as well as the higher impurity concentration [Pac96,Bae04]. For these high fluence implanted samples, TEM studies showed that after the initial epitaxial regrowth of the 6H-SiC, the remaining recrystallized surface layer is composed of a mixture of columnar 6H-SiC, a granular layer and polycrystalline uppermost layer consisting of mainly 3C crystallites [Hei95,Ish97,Pac96,Hee95,Hef96,Har96,Wen98]. This behaviour has also been observed by Reflection High Energy Electron Diffraction analyses (RHEED) [Pez92,Pez93].

The polytype transition from 6H-SiC to mainly 3C SiC occurring during this recrystallization has been explained by Pacaud *et al*. [Pac96] and has been discussed further by Malherbe [Mal13] in a comprehensive review of the behaviour of fission products in silicon carbide. Pacaud uses a homo-epitaxial growth model to explain this behaviour. Homo-epitaxial growth of 6H-SiC on (0001) 6H-SiC substrates had been observed to occur via a step flow mechanism only above 1700 ºC [Bur31]. On the other hand, phase stability diagrams of SiC show that 3C-SiC can form over a wide temperature range that includes temperatures well

below 1700 ºC [Sne07, Kni63, Mal13]. Crystal growth occurs in layers at growth points at steps and at kink sites [Bur31, Fra49].

In armorphous SiC produced by ion implantation, epitaxial regrowth via the step flow mechanism starts from the interface between the crystalline bulk and the amorphous surface layer. Several Rutherford backscattering spectroscopy (RBS) in channelling mode studies [Ben08,Fri09,Fri10,Fri12,Hla10,Mal08,Wen98] have shown that heavy ion bombardment of single crystal SiC at room temperature with ion energies in the order of hundreds of keV and to fluences 1×10^{15} cm^{-2} or higher results in an amorphous surface layer. In these studies, they have shown that solid phase epitaxy (SPE) commences after vacuum annealing at 1000 ºC, the minimum annealing temperature reported. For amorphous surface layers produced by heavy ion implantation with fluences of up to 10^{16} cm^{-2}, the concentration of implanted ions inhibits SPE. This high concentration disturbs the step flow mechanism driving the homo-epitaxial growth and thus the recystallisation here does not follow the pattern of the underlying crystalline bulk anymore [Bae04]. Small recrystallised nuclei that form in the process of lowering of the free energy as the annealing proceeds then act as seed points for crystallites to grow. As mentioned earlier 3C-SiC crystallite growth is more favourable at these temperatures, leading to random nucleation and growth results in a polycrystalline structure of the near surface region. SEM studies [Fri09,Fri10] show that the near surface region recrystallises into a polycrystalline structure on annealing silver and iodine implanted 6H-SiC at temperatures above 1000 ºC.

References

[Bae04] I.T. Bae, M. Ishimaru, Y. Hirotsu and K.E. Sickafus, J. Appl. Phys. 96 (2004) 1451.

[Beh 83] R. Behrisch, "Sputtering by Particle Bombardment II", Springer-Verlag, Berlin (1983).

[Ben89] J. Bentley, P. Angelini, A. Gove, P. Sklad, and A. Fisher, Inst. Phys. Conf. Ser. 98 (1989) 107.

[Ben08] A. Benyagoub, Nucl. Instr and Meth. B 266 12-13 (2008) 2766.

[Bet30] H. Bethe, Ann. Phys. Leipzig 5 (1930) 324.

[Blo33] F. Bloch, Ann. Phys. Leipzig 16 (1933) 285.

[Boh13] N. Bohr, Phil, Mag. 25 (1913) 10.

[Boh48] N. Bohr, Mat. Fys. Medd. Dan. Vid. Selsk. 18 (1948) 8.

[Bol95] W. Bolse, J. Conrad, T. Rodle and T. Weber, Surf. Coatings. Tech.74 (1995) 927.

[Bol97] W. Bolse, J. Conrad, F. Harbsmeier, M. Borowski and T. Rodle, Mater. Sci. Forum 248 (1997) 319.

[Bra05] W. Bragg and R. Kleeman, Phil. Mag. 10 (1905) 318.

[Bur31] W. K Burton, N Cabrera and F C. Frank, Phil. Trans. Roy. Soc. 243A (1931) 299.

[Cal07] W. Callister, "Materials Science and Engineering an Introduction", Seventh Edition, John Wiley & Sons Inc, New York, 2007, p. 39.

[Cha71] L. Chadderton and F. Eisen, Radiat. Eff. 7 (1971)129.

[Chu76] W. Chu, Phys. Rev. A13 (1976) 2057.

[Chu78] W. Chu, J. Meyer and M. Nicolet, "Backscattering Spectrometry", Academic Press, New York, 1978.

[Dea73] G. Dearnaley, J. Freeman, R. Nelson and J. Stephen, "Ion implantation", North-Holland Publishing Company, Netherlands, 1973, p.10.

[Dev01] R. Devanathan, W. Weber and F. Gao, J. Appl. Phys. 90 (2001) 2303.

[Gib75] J. Gibbons, W. Johnson and S. Mylroie, "Projected Range Statistics, Semiconductors and Related Materials", Second Edition, Dowden, Hutchingson & Ros, Pennsylvania, 1975, p.3

[Gna99] H. Gnaser, "Low-Energy Ion Irradiation of Solid Surfaces", Springer, Berlin, 1999, p.2.

[Fel86] L. Feldman and J. Meyer, "Fundermentals of Surface and Thin Film Analysis", Elservier Science Publishing Co, New York, 1986.

[Fra49] F.C. Frank and J.H. van der Merwe, Proc. Royal Soc. A198 (1949) 205.

[Fri01] E. Friedland, "Radiation Damage in Metals", Crit. Rev. Solid. Stat. Mater. Sci. 25 (2001) 88.

[Fri09] E. Friedland, J.B. Malherbe, N.G. van der Berg, T. Hlatshwayo, A.J. Botha, E. Wendler and W. Wesch, J. Nucl. Mater. 389 (2009) 326.

[Fri10] E. Friedland, N.G. van der Berg, J.B. Malherbe, R.J. Kuhudzai, A.J. Botha, E. Wendler and W. Wesch, Nucl. Instr and Meth. B 268 (2010) 2892.

[Fri12] E. Friedland, N.G. van der Berg, J.B. Malherbe, E. Wendler, W. Wesch, J. Nucl. Mater. 425 (2012) 205.

[Har96] S. Harada, M. Ishimaru, and T. Motooka, Appl. Phys. Lett. 69 (1996) 3534.

[Hee95] V. Heera, R. Kögler, W. Skorupa and J. Stoemenos, Appl.Phys. Lett. 67 (1995) 1999.

[Hef96] A. Heft, E. Wendler, J. Heindl, T. Bachmann, E. Glaser, H. Bachmann, E. Glaser, H. Strunk and W. Wesch, Nucl. Instr and Meth. B. 113 (1996) 239.

[Hei95] J. Heindl, H. Strunk, A. Heft, T. Bachmann, E. Glaser, E. Wendler, and W. Wesch. Inst. Phys. Conc. Ser. No. 146 (1995). 435.

[Hla10] T. Hlatshwayo, "Diffusion of silver in 6H-SiC", PhD Thesis, Department of Physics , University of Pretoria, 2010.

[Hof76] W. Hofer, in "Erosion and Growth of Solids Stimulated by Atoms and Ion Beams" G. Kiriakidis (Ed.), G. Carter and J. Whtiton (1986).

[Höf98] A. Höfgen, V. Heera, F. Eichhorn, W. Skorupa, App. Phys. 84 (1998) 4769.

[Höf99] A Höfgen, V. Heera, F. Eichhorn, W. Skorupa and W. Möller, Mater. Sci. Eng. B61 (1999) 353.

[Ish97] M. Ishimaru, S. Harada, T. Matooka, T. Nakata, T. Yoneda and M. Inoue, Nucl. Instr and Meth. B 127 (1997) 195.

[Ish02] M. Ishimaru, I. Bae, Y. Hirotsu, S. Matsumura and K. Sickafus, Phys. Rev. Let. 89 issue 5 (2002) 055502-1.

[Inu90] H. Inui, H. Mori and H. Fujita, Philos. Mag. B 61 (1990) 107.

[Inu92] H. Inui, H. Mori, A. Suzuki and H. Fujita, Philos. Mag. B 65 (1992)1.

[Kal88] A. Kaloyeros, R. Rizk and J. Woodhouse, Phys. Rev. B 38 (1989) 13 099.

[Kam84] E. Kamaratos, Chem. Rev. 84 (1984) 561.

[Kin55] G. Kinchin and R Pease, Rep. Prog. Phys. 18 (1955) 1.

[Kni63] W.F. Knippenberg, Phillips Res. Reports 18 (1963) 161.

[Kuh10] R. Kuhudzai, "Diffusion of ion implanted iodine in 6H-SiC", Masters Dissertation, Department of Physics, University of Pretoria, South Africa, 2010, p. 55.

[Kuh12] R. Kuhudzai, Proceedings from 57th SAIP Conference, University of Pretoria, Pretoria (2012) Submitted.

[Lin53] J. Lindhard, M. Scharff and K. Dan. Vidensk. Selsk. Mat. Fys. Medd. 33 (1953) No 15.

[Lin61] J. Lindhard and M. Scharff, Phys. Rev. 124 (1961) 128.

[Lin63] J. Lindhard, M. Scharff and H. Schiøtt, Kg1. Danske Videnskab. Selskab, Mat. Fys. Medd. 33 (1963).

[Mal94] J. Malherbe, CRC Crit. Rev. Solid State Mater. Sci. 19 (1994) 55.

[Mal08] J.B. Malherbe, E. Friedland and N.G. van der Berg, Nucl. Instr and Meth. B 266 (2008) 1373.

[Mal13] J.B. Malherbe, J. Phys. D. Appl. Phys. 46 (2013) 473001.

[McH93] C. McHargue and J. Williams, Nucl. Instr and Meth. B 80 (1993).

[Mel00] P. Melinon, P. Keghelian, A. Perez, J. Rousset, A. Cadrot, A. Malhomme, A. Renouprez and F. Cadete Santos Aires, Philos. Mag. A 80, (2000) 143.

[Mor70] F. Morehead and B. Crowder, Rad. Effects, 6 (1970) 27.

[Mus96] P. Musumeci, L. Calcagno, M. Grimaldi, G. Foti, Nucl. Instr and Meth. B 116 (1996) 327.

[Mus01] P. Musumeci, F. Roccaforte, and R. Reitano, Europhys. Lett. 55 (2001) 674.

[Nag75] H. Nagiub, R. Kelly, Rad. Effects, 25 (1975) 1.

[Nor03] J. Nord, "Modelling of high-dose radiation damage in simiconductors" Academic Dissertation, Department of Physical Sciences, University of Helsinki, Finland, 2003, p. 8.

[Pac96] Y. Pacaud, J. Stoemenos, G. Brauer, R. Yankov, V. Heera, M. Voelskow, R. Kogler and W. Skorupa, Nucl. Instr and Meth. B 120 (1996) 177.

[Pez92] J. Pezoldt, A. Kalnin and W. Savelyev, Nucl. Instr and Meth. B 65 (1992) 361.

[Pez93] J. Pezoldt, A. Kalnin, D. Moskwina and W. Savelyev, Nucl. Instr and Meth. B 80 (1993) 943.

[Phi70] J. C. Phillips, Rev. Mod. Phys. 42 (1970) 317.

[Poa78] J. Poate, K. Tu and J. Mayer, "Thin Film-Interdiffusion and Reactions" John Wiley & Sons, New York, (1978), p. 83.

[Sat01] M. Satoh, Y. Nakaike and T. Nakamura, J. Appl. Phys. 89 (2001) 1986.

[Sat02] M. Satoh, Materials Science Forum, 389-393 (2002) 773.

[Ser96] C. Serre, L. Calvo-Barrio, A. Perez-Rodriguez, A. Romano-Rodriguez, J. Morante, Y. Pacauld, R. Kogler, V. Heera and W. Skorupa, J. Appl. Phys. 79 (1996) 6907.

[Sne07] L.L. Snead, T. Nozawa, Y. Katoh, T. Byun, S. Kondo and D.A. Petti, J. Nucl. Mater. 371 (2007) 329.

[Swa71] M. Swanson, J. Parsons and C. Hoelke, Rad. Effects. 9 (1971) 249.

[Tak92] T. Takeshita, Y. Kurata and S. Hasegawa, J. Appl. Phys. 71 (1992) 5395.

[Tes95] J. Tesmer and M. Nastasi, "Handbook of Modern Ion Beam Materials Analysis", MRS, Pittsburgh, USA (1995), p. 14.

[Tow94] P. Townsend, P. Chandler and L. Zhang, "Optical Effects of Ion Implantation" Cambridge University Press, Cambridge, UK, 1994.

[Voo69] F. Vook and H. Stein, Rad. Effects. 2 (1969) 23.

[Voo71] F. Vook in Radiation and Defects in Semiconductors, Inst. Phys. Conf. ser. No. 16, edited by J. Whitehouse, Institute of Physics, London (1973).

[Web94a] W. Weber., R Ewing and L Wang, J. Mater. Res. 9 (1994) 688.

[Web94b] W. Weber and L Wang, Nucl. Instr and Meth. B 91 (1994) 63.

[Web95] W. Weber and L. Wang, Nucl. Instr and Meth B 106 (1995) 298.

[Web96] W. Weber , L Wang and N. Yu, Nucl. Instr and Meth. B 116 (1996) 322.

[Wer06] M. Werner , "Damage formation and annealing studies of low energy ion implants in silicon using medium energy ion scattering" PhD Thesis, Institute for Materials Research School of Computing, Science and Engineering ,The University of Salford, UK, 2006, p.37.

[Was07] G. Was, "Fundamentals of Radiation Materials Science, Metals and Alloys", Springer, Berlin 2007, p.63.

[Wen98] E. Wendler, A. Heft and W. Wesch, Nucl. Instr and Meth. B 141 (1998) 105.

[Wei96] H. Weishart, H. Steffen, W. Matz, M. Voelskow, W. Skopura, Nucl. Instr and Meth. B 112 (1996) 338.

[Wes95] W. Wesch, A. Heft, E. Wendler, T Bachmann, E. Glaser, Nucl. Instr and Meth. B 96 (1995) 335.

[Wil73] R. Wilson and G. Brewer, "Ion beams, with applications to ion implantation", John Wiley and Sons Inc., New York, 1973, p.268.

[Wil98] J. Williams, Mat. Sci. Eng. A 253 (1998) 1.

[www1] http://www.genplot.com, 4 November 2009.

[Yas04] H. Yasuda and H Mori, Materials, Transactions. 45. 1 (2004) 2.

[Zie80] J. Ziegler and U. Littmark, "Handbook of Range Distributions or Energetic Ions in All Elements",Pergamon Press, New York, 1980, p.2.

[Zie85] J. Ziegler, J. Biersack and Y. Littmark, "The Stopping and Range of Ions in Solids, Pergamon Press, New York, 1985.

[Zie88a] J. Ziegler and J. Manoyan, Nucl. Instr and Meth. B 35 (1988) 215.

[Zie88b] J. Ziegler "Ion Implantation Science and Technology", 2nd edition Academic press, New York, 1988.

Chapter 3: Diffusion

Introduction

The process by which matter is transported from one part of a medium with a higher concentration to another with a lower concentration as a result of random motion is known as diffusion. Random walk theory is used to characterize the motion of the particles of diffusing substance. In a one dimensional system, each particle has equal probability of moving in a direction either side of its initial position, that is, the particle has no preferred direction of motion for a given time interval. The net flow of matter in the medium is governed by the concentration gradient, with particles moving from a region of higher concentration to a region of lower concentration. The flow down the concentration gradient is not influenced by a bias towards a particular direction, the net flux results from the fact that there are more atoms that randomly move in the region of higher concentration than in the region of lower concentration.

Changes to the structure of materials which ultimately influence the physical and mechanical properties of the materials often occur as a consequence of a diffusion process [She89]. These transformations are brought about by material transport via atomic motion. In a crystal, atoms are normally found oscillating about their lattice positions with frequencies of the order of the Debye frequency which is approximately 10^{12} Hz [Hei05]. Diffusion is essentially a stepwise migration of atoms from lattice site to site [Cal07]. This migration is then only feasible when a vacancy is present in the lattice and the diffusing atom has sufficient energy to break the bonds with its neighbours thus overcoming the potential barrier to make the move. This movement is often referred to as a 'jump'. The movement of atoms is strongly influenced by the diffusing species, host material and the temperature of the environment. Collisions with other atoms in the material also influence the path of the diffusing species hence the diffusion phenomenon is characterised by zigzag motion governed by the random walk process as mentioned above.

3.1 The diffusion coefficient

If we consider a reference plane and the direction x perpendicular to that plane, an expression relating the flux J, to the concentration gradient $\partial C/\partial x$ and the diffusion coefficient D, can be written as:

$$J = -D\frac{\partial C}{\partial x} \tag{3.1}$$

here C is the concentration of the diffusing substance. Equation (3.1) is known as Fick's first law [Cra75, Jos60]. The diffusion coefficient, also known as the diffusivity, gives a measure of the ease with which particles move in a medium, that is how far the particle can move within a given time interval. For an isotropic medium, in three dimensions, Fick's first law can be written as:

$$\bar{J} = -D\nabla C \tag{3.2}$$

Fick's second law, widely regarded as the general diffusion equation, is derived from equation (3.1) and the continuity equation.

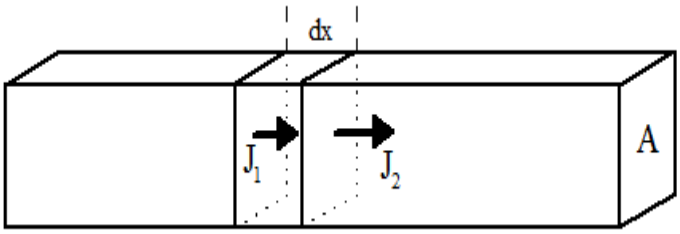

Figure 3.1: A differential volume element in a bar of cross-sectional area A, with impurity flux into and out of the volume J_1 and J_2 respectively. Redrawn from [Cam96].

For the long bar of material in figure 3.1, with cross section A, and considering a small volume of length dx, and a one dimensional flux, J_1 entering the volume, and flux J_2 leaving the volume [Cam96], we have,

$$\frac{J_2 - J_1}{dx} = \frac{\partial J}{\partial x} \tag{3.3}$$

For the case $J_2 \neq J_1$, the concentration of the diffusing substance in the small volume element of the bar will change. With the number of impurity atoms in the volume element being given by the product of the concentration and the differential volume element ($A \cdot dx$), the continuity equation is then:

$$-A(J_2 - J_1) = -A \cdot dx \frac{\partial J}{\partial x} = A \cdot dx \frac{\partial C}{\partial t} \tag{3.4}$$

Equation (3.4) can thus be presented as

$$\frac{\partial C}{\partial t} = -\frac{\partial J}{\partial x} \tag{3.5}$$

Incorporating Fick's first law, equation (3.1) into equation (3.5) yields the general form of Fick's second law.

$$\frac{\partial C}{\partial t} = \frac{\partial}{\partial x}\left(D \frac{\partial C}{\partial x}\right) \tag{3.6}$$

Based on the assumption that the diffusion coefficient is independent of position, Fick's second law reduces to

$$\frac{\partial C}{\partial t} = D \frac{\partial^2 C}{\partial^2 x} \tag{3.7}$$

For an isotropic medium, in three dimensions, Fick's second law is expressed as:

$$\frac{\partial C}{\partial t} = D \nabla^2 C \tag{3.8}$$

The temperature dependence of the diffusion coefficient [Sha73] is given by an Arrhenius equation:

$$D = D_0 \exp\left(\frac{-E_A}{kT}\right) \tag{3.9}$$

E_A is the activation energy, k is the Boltzmann constant, D_0 is a temperature independent pre-exponential factor and T the temperature in units of Kelvin.

3.2 Evaluation of the diffusion coefficient

Several methods of obtaining the general solutions of the diffusion equation (3.7) for a variety of initial and boundary conditions are discussed in the book "*The Mathematics of Diffusion*" by Crank [Cra75]. In this study , in order to describe the spreading by diffusion of the implanted fission product elenents with annealing time, we have used the solution shown in equation (3.10) [Mye74]. This method assumes that the original implanted profile is purely Gaussian and gives the diffused profile as

$$C(x,t) = \left[2(\pi Dt)^{1/2}\right]^{-1} \int_0^\infty C_0(y) \times \left(e^{-(y-x)^2/4Dt} + e^{-(y+x)^2/4Dt}\right) dy \tag{3.10}$$

To obtain this solution the initial condition

$$\lim_{x\to 0}\left(\frac{\partial}{\partial x} C(x,t)\right) = 0$$

is used, with $C_0(x) = C(x,0)$ representing the initial iodine profile.

The initial profile $C_0(x)$ is taken to be:

$$C_0(x) = K(\pi Dt_0)^{-1/2} e^{-x^2/4Dt_0} \tag{3.11}$$

where K is an adjustable constant. The concentration profile in equation (3.10) reduces to a Gaussian function of the form:

$$C(x,t) = K[\pi D(t+t_0)]^{-1/2} e^{-x^2/4D(t+t_0)} \qquad (3.12)$$

In the dilute limit, the concentration profile will remain a normal distribution with annealing time t in an infinite medium and equation (3.12) can generally be expressed as:

$$C(x,t) = K[\pi Dt]^{-1/2} \exp\left(-x^2/4Dt\right) \qquad (3.12b)$$

Defining the profile width $W(t)$ as the full width at half maximum (FWHM), the relationship between the final and initial widths are given by

$$[W(t)]^2 = 4Dt\ln(2) + [W(0)]^2 \qquad (3.13)$$

Therefore from the change in the FWHM of a Gaussian depth distribution, the slope of a plot of $[W(t)]^2$ versus the annealing time t at constant temperature will yield the diffusion coefficient D.

3.3 Mechanisms of diffusion in solids

Diffusion does not take place in an ideal crystal. An enormous amount of energy would be required to break the bonds between lattice atoms and cause atoms to jump simultaneously and exchange positions. In real crystals, the mobility of atoms is enhanced by the presence of defect structures. These include point defects such as vacancies and interstitials (Frenkel-pairs) as well as extended defects like point defect clusters, dislocations and grain boundaries. The atoms oscillate about their equilibrium positions with frequencies of the order of the Debye frequency which is approximately 10^{12} Hz [Hei05] until they acquire enough energy to surpass the potential barrier jump from one site to another, leading to diffusion in the solid. Fick's diffusion equations describe diffusion on a macroscopic level. It is thus necessary to also understand the phenomenon on a microscopic level to get a clearer picture of the processes involved. In our review on the literature of diffusion we shall deal initially with movement of atoms in single crystals (volume diffusion), and then extend it further to include

a short review of diffusion in polycrystalline materials. Diffusion in polycrystalline materials is more complex in that on top of intra-grain diffusion, movement of atoms readily occurs as well along the high diffusity paths such as along the boundaries between grains.

3.3.1 Diffusion in Crystalline materials.

In perfect crystals, atoms are so closely packed that an atomic jump of any atom must be accompanied by a simultaneous jump of a nearby atom in the opposite direction. To facilitate this jump (figure 3.1), the lattice the lattice must undergo considerable distortion in between the jumps and hence a great deal of energy is required to surmount the potential barrier required to make the jump [Gui89].

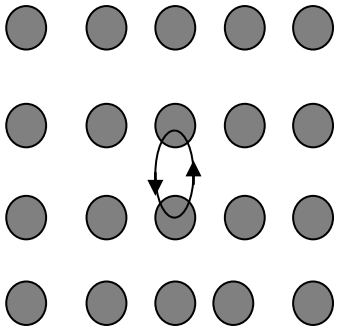

Figure 3.2: Direct interchange of neighbouring atoms, redrawn from reference [Gui89].

Jumps requiring less energy are therefore much more favourable. Defects in solid which act as locations of minimum energies for displaced atoms are then the primary vehicles for the diffusion process. Diffusion in crystalline materials therefore occurs mainly via defects contained within the crystal. Defects could be introduced in the material during preparation or any subsequent treatment the material may be subjected to. Several methods detailing how atoms jump from one stable position to another in the lattice of a single crystal have been proposed in literature [Mro80,She89,Was07]. Examples of these mechanisms include the vacancy mechanism, interstitial mechanism and the interstitialcy mechanism.

3.3.2 Vacancy mechanism

Unoccupied lattice sites, known as vacancies, provide the favourable route for atomic diffusion. In the vacancy mechanism [She89], atoms from adjacent sites can jump into a nearby vacancy. The atoms sitting next to a vacancy are bonded to fewer atoms as a result of the displacement of one of the lattice atoms, hence less energy is required to move the adjacent atom into the vacancy than in a direct position exchange between two adjacent atoms without a vacancy between them.

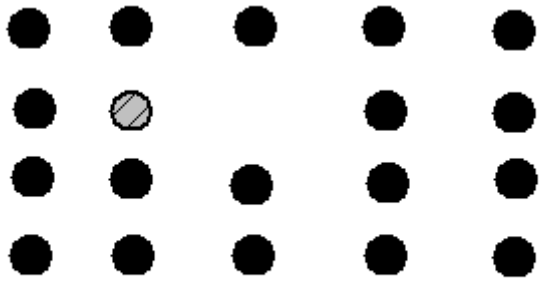

(a)

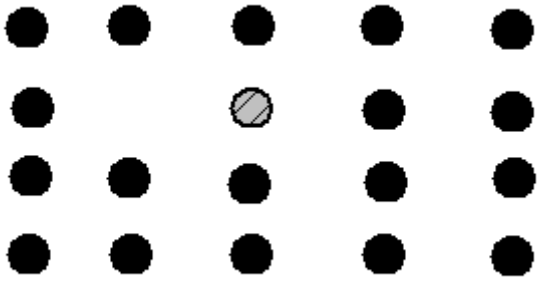

(b)

Figure 3.3: (a) and (b) show the diffusion of an impurity by vacancy exchange.

The probability that a site is vacant is proportional to the Boltzmann factor for thermal equilibrium [Kit05]. For a crystal lattice composed of N atoms, the equilibrium number of vacancies n is given by the Boltzmann factor as:

$$\frac{n}{N-n} = \exp(-E_V / k_B T) \tag{3.14}$$

where E_V is the energy required to move one atom from a lattice site within the crystal to one on the surface (energy to create Schottky defect) and k_B is the Boltzmann constant. When $n<<N$ equation (3.14) then becomes

$$n = N \exp(-E_V / k_B T) \tag{3.15}$$

Vacancies can also be created when a lattice atom is displaced from its lattice site to an interstitial position. This type of defect is referred to as the Frenkel defect [Kit05]. If the number of Frenkel defects n, is far smaller than N, the number of lattice sites, and also far smaller than N', the number of interstitial sites, then [Kit05]:

$$n \cong (NN')^{1/2} \exp(-E_1 / 2k_B T) \tag{3.16}$$

where E_1 is the energy required to remove an atom from a lattice site to an interstitial position.

3.3.3 Interstitial mechanism

An atom diffusing interstitially [She89] meanders from one interstitial site to another without displacing any of the lattice atoms. These solute atoms are usually smaller than lattice atoms and can easily move from one interstitial site to the next. This mechanism is commonly referred to as the direct interstitial mechanism.

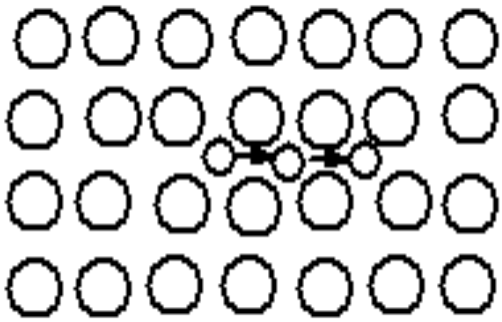

Figure 3.4: Diffusion of an impurity atom via the interstitial mechanism.

Larger atoms sitting in interstitial positions may require large amounts of energy to overcome the potential barrier associated with the large distortions to the lattice to facilitate an interstitial jump. A jump process needing less distortion may then be more favourable. A process known as the interstitialcy mechanism is an example of one mechanism needing less distortion [She89]. In this case, an atom in an interstitial position pushes one of its nearest neighbour atoms out of a lattice position into an interstitial one and itself taking up the lattice site previously occupied by the atom it had dislodged. Interstitialcy mechanism generally occurs when the atom diameters of the host lattice and diffusing atom are similar or generally comparable [Was07]. Two types of interstitialcy diffusion [Was07] are the collinear in which the atoms move along a straight line and the non collinear, when the displaced atoms moves into an interstitial position at an angle to the direction of motion of the incident atom (the dislodging atom). Illustrations of these to variants are shown in figure 3.4.

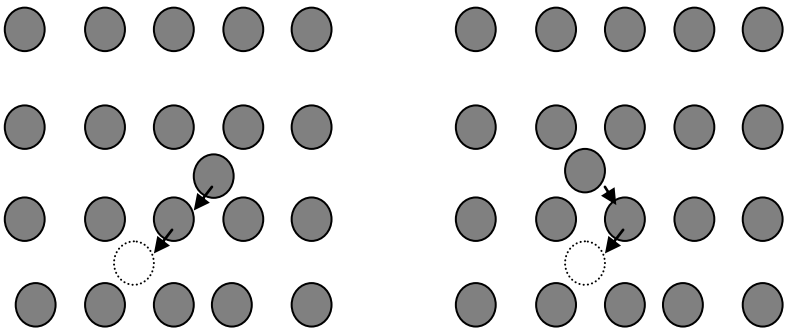

(a) (b)

Figure 3.5: Interstitialcy mechanism of diffusion (a) collinear (b) non-collinear. Redrawn from reference [Was07].

In general, any increase in the number of vacancies beyond their thermal equilibrium concentration or any local distortion to the close-packing of the lattice atoms will enhance diffusion processes [Guil89].

An example of common extended defects often found in SiC crystals resulting from the manufacturing process are micropipes. Micropipes are cylindrical pipes running through from one end to the other of the crystal, hence diffusion will be more rapid along micro pipes than through perfect bulk material. Defects can also be retained during certain treatment of the material. An example of such behaviour is in the extent of defect retainment after ion irradiation of SiC. As discussed in chapter 2, the extent to which defects are retained in ion implanted single crystalline materials depend on the parameters of the implantation process. Examples of these parameters include the temperature of implantation, the implantation rate, specie of ions implanted, the energy of implantation and the type of target material. Ion implantation in SiC for example sees more defects being retained for implantation at low temperatures as compared to implantations done at high temperatures [Wen98]. At high temperatures, atoms have more kinetic energy to move around increasing the probabilities of recombination with vacant lattice sites unlike at low temperatures where generated defects are more likely to be ‘frozen in’ after ion implantation.

3.4. Diffusion in defective and damaged crystals

Defect complexes and damage clusters in crystals can influence the diffusion in and through solids. In such materials, diffusion through damage centres can be slower than in less damaged regions as the diffusion could be subjected to a trapping-detrapping mechanism [Kas94]. If A and B are defined as the probability rates for ion trapping and ion detrapping respectively, then for traps homogeneously distributed throughout the damaged region of interest, the differential equations for the trapping and de-trapping are given in equations (3.17) and (3.18) [Kas94, Kas96,Soa04]:

$$\frac{\partial C_f}{\partial t} = D\frac{\partial^2 C_f}{\partial x^2} - AC_f + BC_t, \qquad C_f = C_f(x,t) \tag{3.17}$$

$$\frac{\partial C_t}{\partial t} = AC_f - BC_t, \qquad C_t = C_t(x.t) \tag{3.18}$$

where, C_f and C_t represent the concentration of free and trapped ions respectively, C is the total ion concentration and $C=C_f+C_t$. It has been shown also [Kas94], that:

$$B = v_t \exp(-E_t / kT) \tag{3.19}$$

and

$$A = 4\pi r_s D c_s \tag{3.20}$$

where v_t is the jump frequency, E_t the activation energy for the detrapping process, r_s the effective trapping radius, D the diffusion coefficient and c_s the concentration of effective traps. Equations (3.17) and (3.18) have been solved numerically using the "Finite Difference Method" [Kas94,Smi78].

3.5 Diffusion in polycrystalline materials

Crystalline materials are often found in polycrystalline form. Here the materials are composed of multiple grains generally orientated at random and separated from each other by boundaries along which atomic configurations are severely distorted [Gui89,Was07].

These grain boundaries usually have dimensions of a few lattice spacings and models concerning grain boundary diffusion generally assume grain boundary widths (δ) ranging from δ=0.3-0.5 nm [Was07]. It is known from experiment that at low temperatures diffusion is faster along the grain boundaries than through bulk of a grain due to the high level of disorder along the boundaries [She89,Poa78]. Grain boundaries along with other defects such as dislocations and free surfaces where diffusion occurs faster are often referred to as high diffusivity paths [She89,Gui89,Was07]. The diffusion in polycrystalline materials is a more complex process due to the fact that grain boundary diffusion can rarely be decoupled from lattice or volume diffusion as the diffusing species can also leak from the boundary into the lattice. Therefore diffusion can occur along multiple paths in polycrystalline materials [Poa78].

References

[Bar51] R. Barrier, "Diffusion in and through Solids", Cambridge University Press, Cambridge, England (1951).

[Cal07] W. Callister, "Materials Science and Engineering an Introduction 7th edition", John Whiley and Sons, New York, U.S.A. 2007.

[Cam96] S. Campbell, "The Science and Engineering of Microelectronic Fabrication", Oxford University Press, 1996, p.40.

[Cra75] J. Crank, "The Mathematics of Diffusion", Oxford University Press, Bristol, 1975, p.2.

[Fick55] A. Fick, Ann. Phys. (Leipzig) 170 (1855) 59.

[Gui89] A. Guinier and R. Jullien, "The Solid State, From Superconductors to Superalloys",Oxford University Press, London, 1989.

[Hei05] P. Heitjans and J. Karger, "Diffusion in Condensed Matter", Springer, Netherlands, 2005, p.22.

[Jos60] W. Jost, "Diffusion in Solids, Liquids and Gases", Academic Press, New York, 1960, p.2

[Kas94] J. Kaschny and M. Behar, Nucl. Instr and Meth. B 88 (1994) 267.

[Kas96] J. Kaschny and M. Behar Nucl. Instr and Meth. B 111 (1996) 51.

[Kit05] C. Kittel, "Introduction to Solid State Physics", 7th ed, John Wiley and Sons, Inc. California, (2005).

[Mro80] S. Mrowec, "Defects and Diffusion in Solids, an introduction", Elsevier, New York, 1980.

[Mye74] S. Myers, S. Picraux and T. Prevender, Phy. Rev B. 9 (1974) 3953.

[Poa78] J. Poate, K. Tu and J. Mayer, "Thin Films Interdiffusion and Reactions", John Wiley and Sons, Inc., USA (1978).

[Sha73] D. Shaw, "Atomic Diffusion in Semiconductors", Plenum Press, London, 1973, p.3.

[She89] P. Shewmon, "Diffusion in Solids", The Minerals, Metals and Materials Society, U.S.A, 1989, p.57.

[Smi78] G. Smith, "Numerical Solution of Partial Differential Equations: Finite Difference Methods", 2nd, ed. Oxford (1978).

[Soa04] M. Soares, L. Amaral, M. Behar, F. Fink, Nucl. Instr and Meth. B 215 (2004) 90.

[Was07] G. Was, "Fundamentals of Radiation Materials Science, Metals and Alloys", Springer, Berlin 2007, p.168.

[Wen98] E. Wendler, A. Heft and W. Wesch, Nucl. Instr and Meth. B 141 (1998) 105.

Chapter 4 Experimental: Analysis Techniques

4.1 Scanning Electron Microscopy (SEM)

Introduction

The development of the first conventional light microscope (with a magnification of roughly 200) by Antoni van Leeuwenhoek in the 15th century [Zha09] led to more research focused on how to improve the magnification and the quality of the images. The work of German optician Ernst Abbe in 1873 led to the establishment of the relationship between the wavelength of light and the resolving power of a microscope, *d*, given by [Zha09]:

$$d = \frac{0.612\lambda}{n\sin\alpha} \tag{4.1}$$

where *d*, the resolving power can be defined as the minimum resolvable separation between two points, λ is the wavelength of the light and n is the refractive index of the medium between the specimen and objective lens and α is the half angle in radians of the cone of light from the specimen plane accepted by the objective. The product *n*sinα is usually referred to as the numerical aperture (NA).

The origins of electron sources and the possibility of forming electron beams were later demonstrated by JJ Thompson in the later part of the 19th Century [Zha09]. De Broglie's relationship of 1924 given in equation (4.2) outlined the relationship between a moving electron and radiation with an associated wavelength:

$$\lambda = \frac{h}{mv} \tag{4.2}$$

where λ is the wavelength of the moving particle (in this case the electron), *h* is Plank's constant, *m* is the mass of the electron and *v* is the speed of the electron. The use of electron beams with the advantage of smaller wavelengths compared to the wavelength of light meant microscopes with better resolving power. The idea of the electron microscope then became feasible after Busch in 1926 showed the similarity between the refraction of electron beams through magnetic fields and the refraction of light through glass lenses. This development proved that the geometric laws of optics could be applicable to electron systems [New00].

4.1.1 Electron beam-specimen interactions

Before we look at the principles behind the operation of scanning electron microscopes, we review briefly the physics of electron beam interactions with matter. Figure 4.1 shows an illustration of a number of different effects produced from a particular interaction volume of the beam below the sample surface [Vau08].

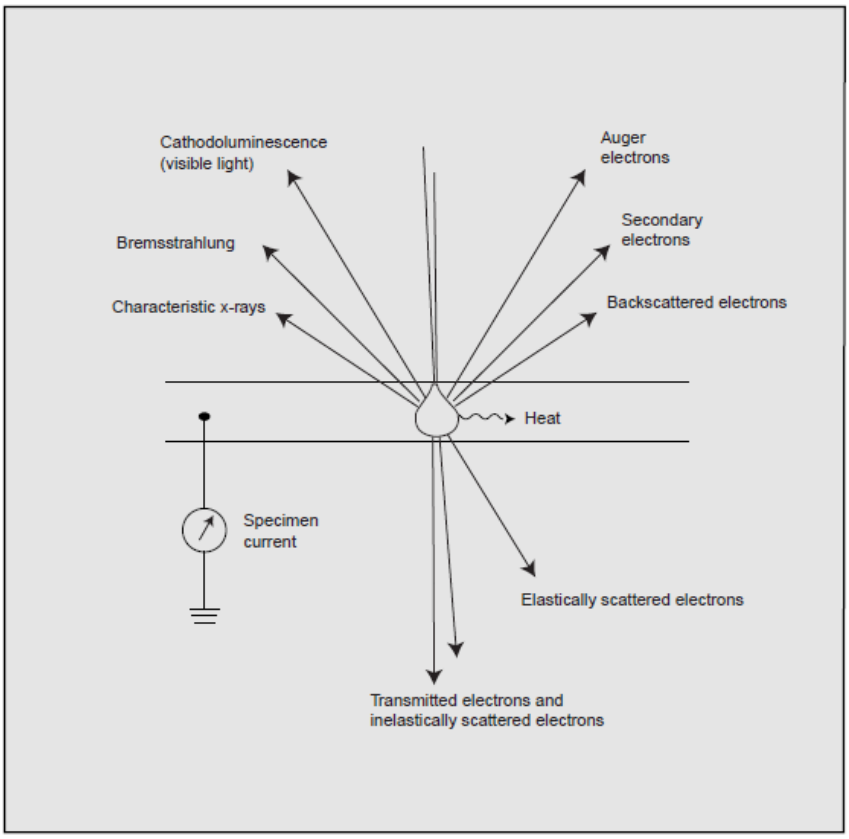

Figure 4.1: The main processes resulting from the interaction of an electron beam with a sample. The diagram shows that Auger and secondary electrons emerge from the near surface region of sample, and elastically scattered electrons are typically scattered through larger angles than the inelastically scattered ones. Taken from [Vau08].

Excitations due to the primary electron beam can create inner shell holes (in low energy levels). Outer shell electrons (in high energy levels) then move to fill up the holes in the lower levels. The energy released during such transitions can be carried away by low energy electrons, e.g. with the so-called Auger electrons emitted from the sample near surface region [Ree05]. Auger electrons with their characteristic energies which escape from the surface

arise from sample depths between 0.5 and 3 nm and therefore Auger Electron Spectroscopy (AES) is a widely used surface analysis technique [Zha09]. Electron transitions between inner atomic levels following the creation of holes can also lead to the emission of X-ray photons with a maximum energy of up to E_0, which is the energy of the incident electrons leading to a continuous X-ray spectrum. Since the X-rays are produced by the energy from the inner level transitions, they are characteristic of the elements in the sample and are used in chemical analysis using a technique commonly referred so as Energy Dispersive X-ray Spectroscopy (EDS) [Gol03]. Some materials are able to emit long-wavelength photons in the visible or infrared spectrum when under electron bombardment. This phenomenon is known as cathodoluminescence. [Ree05,Zha09].

Weakly bonded specimen electrons can be ejected from the specimen (with energy less than 50 eV) via inelastic scattering interactions with the incident electron beam. These low level electrons emanating from the sample itself are known as secondary electrons (SE) [Law87]. SE are mainly used in topographical imaging as they are generated from regions very close to the surface. No significant dependence exists between the sample atomic number and the yield of SE. However, the intensity of the signal from SE is highly sensitive to the topographical features of the sample. An example of this is the so-called edge effect illustrated in figure 4.2 and explained in the next paragraph. More electrons are able to escape at an edge than away from the edge and this results in the edge appearing brighter.

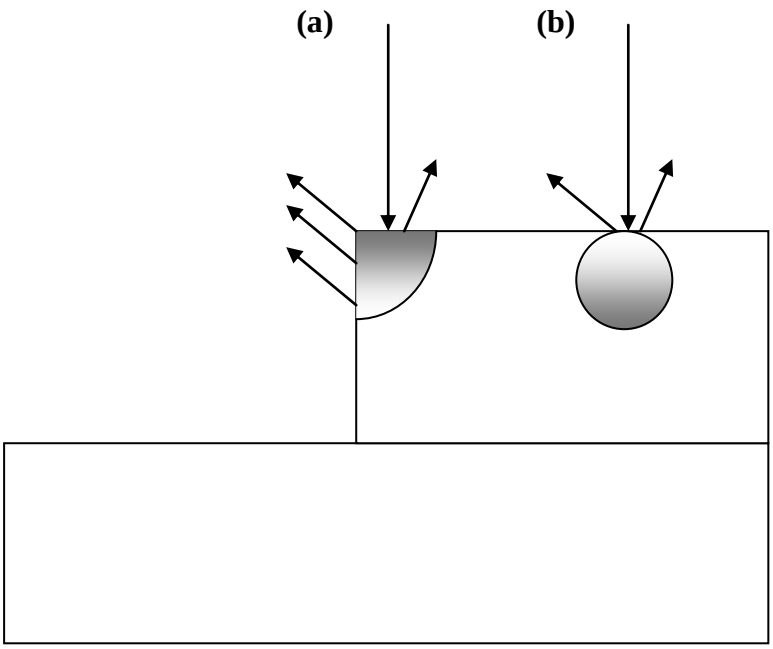

Figure 4.2: Illustration of the edge effect in SE imaging. (a) stronger SE signal at an edge compared with (b) away from the edge of the sample. Redrawn from [Ree05]

As seen in figure 4.2, the electron beam incident angle is more oblique around sample edges (a), resulting in the illumination of a broader area and also a decrease in the escape distance for secondary electrons and hence a higher yield of secondary electrons. For perpendicular incidence (b), the illuminated region is uniform around the axis of the beam and only the electrons activated near the surface can escape with electrons originating elsewhere in the interaction volume being captured before they can escape hence a lower secondary electron than at sample edges.

Electrons in the incident beam can be subjected to large angle scattering during interactions with specimen atoms. Some of the collisions result in the electrons being backscattered and travelling back through the sample and escaping through the surface. Since backscattered electrons are a result of collisions with specimen atoms, their signals are used in compositional contrast imaging. The signal intensity of backscattered electrons increases with increasing atomic number of the specimen. Elements with higher atomic numbers therefore

appear brighter in backscatter electron images. As backscattered electrons are affected by chemical composition, the crystallography and internal magnetic changes in the sample, they are the basis of most compositional studies centred on atomic number distribution, electron channeling and magnetic fields respectively [Zha09]. Backscattered electron emissions are also influenced by the sample tilt angle. Emissions increase with the tilt angle. It is for this reason that microscopy techniques such as Electron Backscatter Diffraction (EBSD) are carried out at high tilt angles (normally tilt angle is around 70 °).

The resolution of an SEM instrument is the key indicator or benchmark of its performance. Resolution is the ability to clearly distinguish between two separate structures of the sample. The ability to discern fine structures and features of a specimen has led to the continued search for microscopes with high resolution. In SEM, the resolution depends on the beam diameter on sample surface or spot size, (d_s). The spot size is a function of the beam current (i_B), beam voltage (V), and the spherical aberration (C_s) of the electron lenses as given in equation 4.3:

$$d_s = a\left[b\frac{i_b}{\beta} + \frac{a}{V}\right]^{3/8} C_s^{1/4} \qquad (4.3)$$

Here, a and b are constants and β is the brightness of the of electron beam. The brightness is in turn dependant on the applied voltage, operation temperature and filament material of electron gun source [Zha09]. Equation 4.3 implies that a higher brightness leads to better performance of a microscope. Electron guns of SEMs come in mainly 3 types, Tungsten filament guns, Lanthanum Hexaboride (LaB_6) guns, and field emission guns, (FEG) [Zho06]. LaB_6 has the advantage over Tungsten, which are cheaper, of having a lower work function of 2.4 eV compared to 4.5 eV of tungsten [Zho06]. LaB_6 filaments therefore provide stronger electron emissions at the same temperature giving them a higher brightness (about 5 -10 times brighter [Zho06] and longer lifespan than the Tungsten filaments. For real high resolution work, field emission guns with their enhanced brightness of about 100 times that of the tungsten filament guns [Zho06] are employed. The SEM images in this Thesis were acquired using an instrument fitted with a FEG and therefore we will concentrate more on this type of electron source.

4.1.2 The Field Emission Gun (FEG)

A single crystal tungsten wire with a very sharp tip (figure 4.3a) is used as the electron source in field emission electron guns. A strong electron field builds ups on the sharp tip and electrons are then drawn from it towards a set of anodes as shown in figure 4.3b [Zho06].

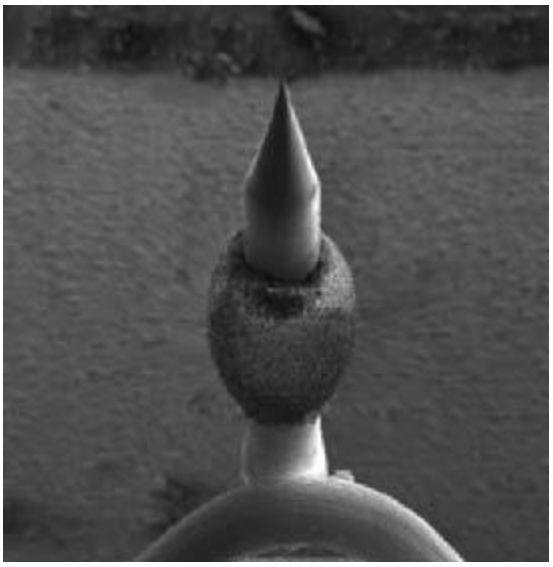

(a)

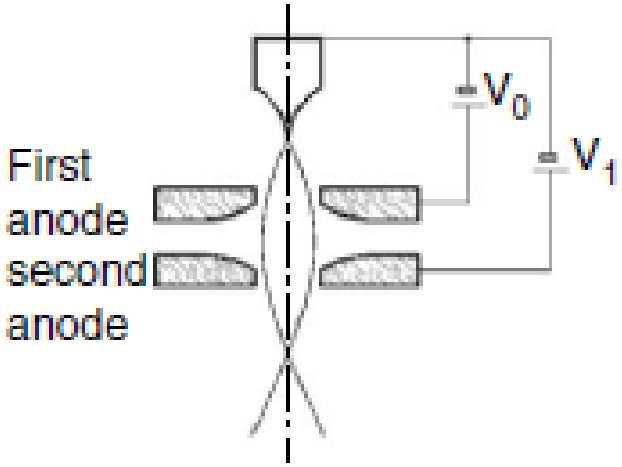

(b)

Figure 4.3: Field emission tip (a) and (b) Schematic of the field electron source showing the two anodes that work as electrostatic lenses in forming the electron beam. Taken from [Zho06].

In this set-up two anodes are employed. A voltage V_0, typically in the order of a few kilovolts, is applied between the tip and the first anode and is used as the extraction voltage to draw the electrons from tip to the anode. An acceleration voltage V_1 applied on the second anode, accelerates the electrons down the optical column of the microscope. In general, three types of field emission sources are used in electron microscopes. These include the Cold Field Emission sources (CFE), Thermal Field Emission sources (TFE) and the Schottky Emitters (SE) [Gol03]. CFE sources are operated at room temperature hence the name cold field emission. The emission of electrons is then only a factor of the voltage applied between the cathode and the anodes. The tip is cleaned periodically by heating it to a temperature of around 2000 K for a few seconds thereby degassing the adsorbed gases. This cleaning process is commonly referred to as flashing. In contrast, TFE sources are operated at elevated temperatures. This has the advantage of reducing the adsorption of gases on the tip.

The third type of source, the Schottky emitter is the type fitted on the University of Pretoria's Laboratory for Microscopy and Microanalysis' Zeiss Ultra 55 High Resolution Microscope used in this study. The SE is the most advanced electron source available commercially. It consists of a single crystalline tungsten wire. The tip of the wire is etched to a tip radius of approximately 0.3 μm to ensure high brightness and the {100} planes are perpendicular to the wire axis [www1]. A zirconium oxide reservoir is placed halfway along the tungsten wire. This reservoir helps to lower the work function of the emitter. The SE source is operated at 1800 K and in vacuum of ~10^{-9} or better [www1].

The advantages of the SE include ease of operation (no flashing required) and higher stability [Ver04]. It has an emission area which is about 100 times larger than that of the CFE leading to greater resistance to vibrations due to external sources/movements [Zho06]. It has a higher emission current which is approximately 50 times that of CFE sources but still possessing similar low energy spread as in CFE's.

Modern advanced microscopy work requires SEM systems that provide electron guns offering a stable electron beam of high current, small spot size, small energy dispersion and adjustable electron beam energy. The stability of the electron beam is therefore a key aspect of electron microscopy. LaB_6 guns offer a smaller energy spread as compared to the tungsten filament gun resulting in the former having a smaller chromatic aberration. Field emission guns offer even smaller energy spread as compared to the LaB_6 guns. CFE guns have a low

energy spread of 0.3 eV [Zho06] but have lower stability than TFE due to the TFE elevated operation temperature reducing adsorption of gases while enhancing electron emission. SE sources offer the best stability of all the above sources.

4.1.3. Electron Beam optical Column

The main components making up an SEM are the vacuum system, the electron gun, condenser lens, some apertures, the objective lens, the scanning or defection coils and a series of detectors to pick up the signals resulting from the various electron beam sample interactions. A schematic of the electron optical column of a cross-section of a typical electron optical column used in Ultra® Field SEM instruments from Zeiss is shown in figure 4.4. The Ultra from Zeiss, is fitted with an in-Lens detector as illustrated in figure 4.4.

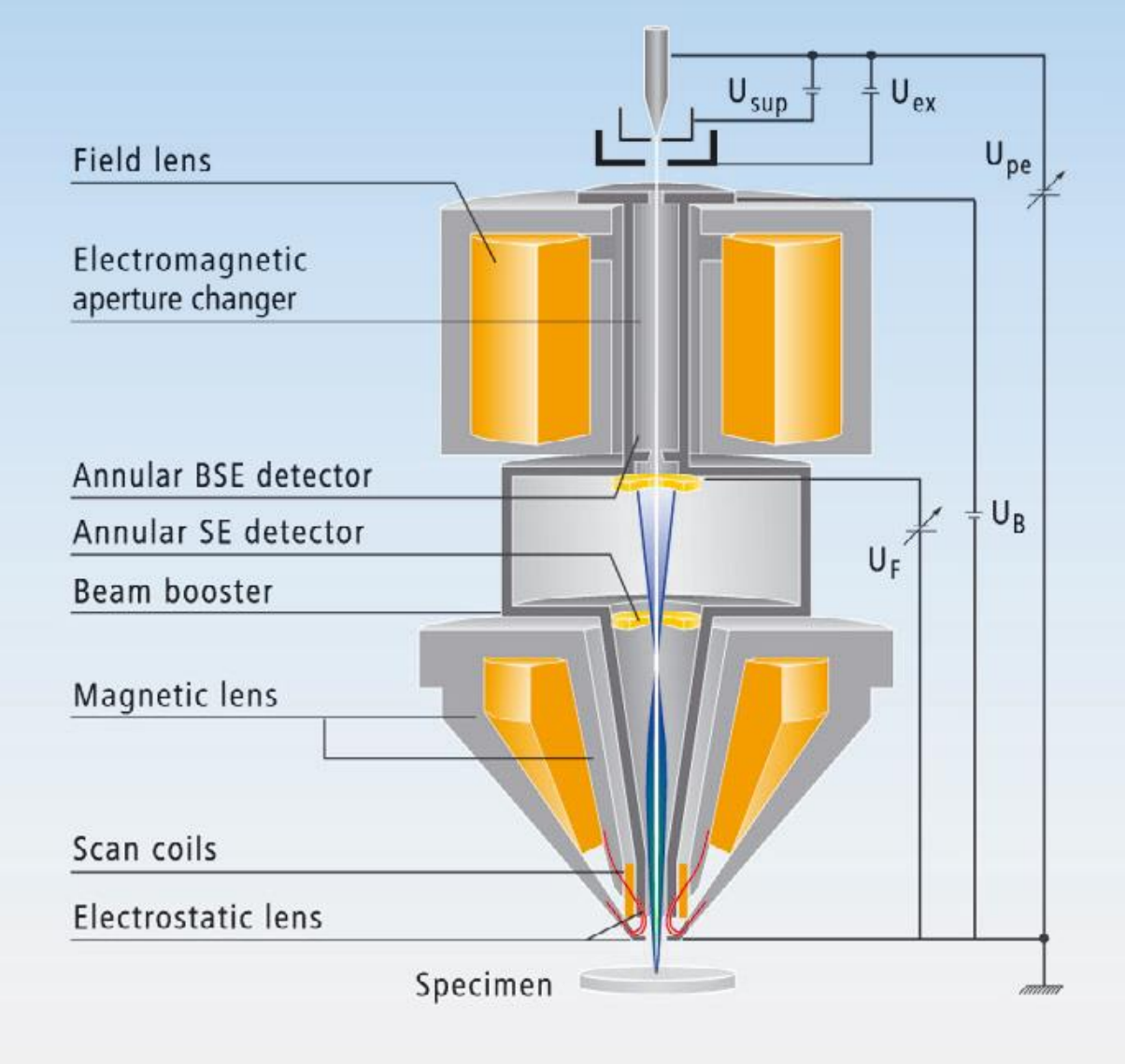

(a)

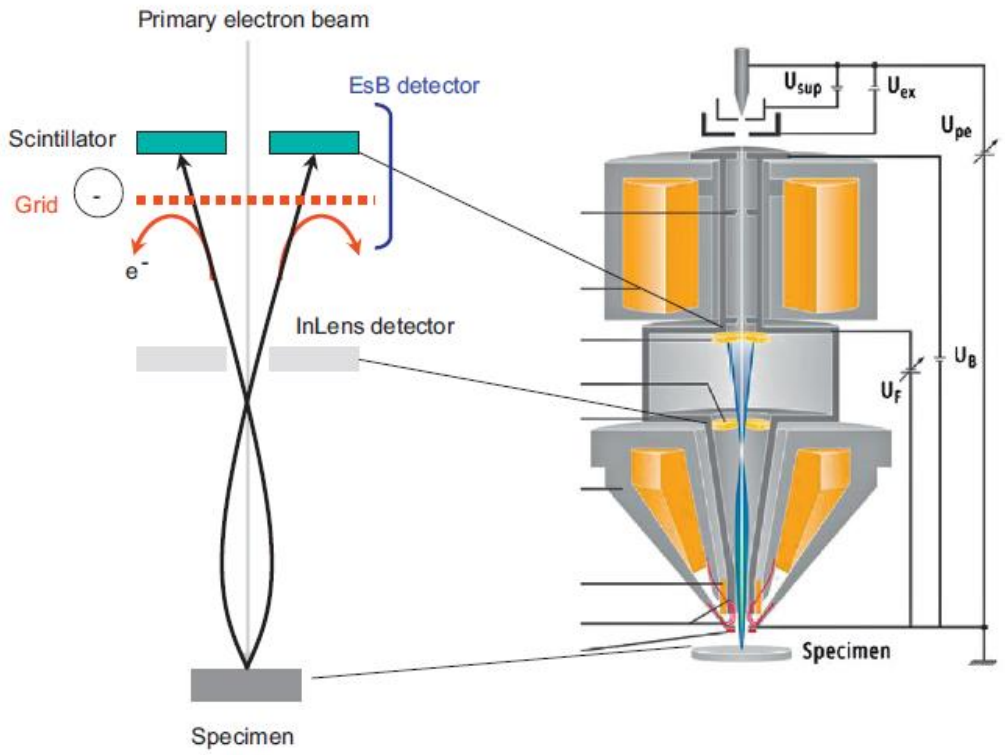

(b)

Figure 4.4: A cross section of the Gemini electron optical column utilised in the Ultra FESEM [Nag13, Ver04].

In figure 4.4, U_{ex} is the extractor voltage of the first anode, U_{PE} is the primary beam voltage, U_B is the booster voltage, normally maintained at 8 kV [Kum09], and U_F is filtering grid voltage that filters SE and only allows BSE to be directed toward the BSE detector.

4.1.4.Condenser lenses

The electron beam emerging from the electron gun will diverge after passing through the anode. A set of magnetic lenses (marked as the Field Lens in figure 4.4) consisting of two rotationally symmetric iron pole pieces with copper winding, provide a magnetic field that converges and collimates the emerging beam into a parallel beam. The beam is streamed through a central hole in the pole pieces and the beam is focused in this lens gap. Adjusting the current of the lenses and hence changing the magnetic field, enables one to adjust the position of the focal point. Further filtration of the beam is made possible by use of a

condenser aperture below the focal point of beam which can be adjusted to sift out inhomogeneous electrons from the beam.

4.1.5. The objective lenses and scanning coils

The electron beam tends to diverge again below the condenser lens and aperture. Another set of magnetic lenses known as the objective lens are employed to focus the beam into a fine probe point on the sample surface as well as facilitate demagnification of beam. Lens demagnification in conjunction with aperture size control will influence the diameter of the electron beam and are used to determine the spot size of beam on sample surfaces. The objective lens is illustrated in figure 4.4 and marked as Magnetic lens in the cross-sectional image. Scanning coils (figure 4.4) deflect the beam along the *x* -and *y*- axis of the sample plane thereby allowing be beam to be "scanned" over an area of the sample and not just the area illuminated by the beam spot size.

4.1.6. In-lens detector

Low voltage scanning electron microscopy (LV-SEM) typically in the range of 100 V to 5 kV [Kum09], is used for high resolution surface imaging due to its high surface sensitivity. This enhanced surface sensitivity is due to the small penetration depths and smaller scattering volume of low energy electrons. The other key feature for high resolution surface image formation is the type of detector utilised. In-lens detectors have been found to have higher surface sensitivity than the traditional out of column Everhart-Thornly (E-T) detectors [Kum09, Suv07]. In the In-lens detector set-up (figure 4.4), in which the detector itself is located in the column above the sample, an immersion lens system is used in the electron optics for nm scale spatial resolution [Kum09]. In such a set-up, an electron beam booster U_B, in the column accelerates the primary beam to several kilovolts. The boosted electrons are then decelerated at the pole-piece of the objective lens located at the end of the electron column. This deceleration field doubles up as a collector of secondary electrons from sample surface by accelerating them into the column [Fro89,Kum09]. Previous studies [Kum09], have shown that there exists a strong relationship between increasing U_B and accelerating the low energy secondary electrons into the in-lens detector. At a booster voltage of 8 kV, the secondary electron image is formed by secondary electrons having energy lower than 40 eV, and are readily attracted by electrostatic field generated by U_B. At this low energy, information is coming from the very near surface hence the in-lens detectors have higher

surface sensitivity than out of column detectors. In out-of-column detectors, the SE electrons detected also contain electrons of higher energies (larger than 40 eV) which come from deeper regions of the sample.

In this work, the microstructure of SiC surfaces before and after annealing was investigated using a high resolution *Zeiss Ultra 55* field emission scanning electron microscope fitted with an in-lens detector. A cross-section of its electron optical column is illustrated in figure 4.4 of section 4.13. A 2 kV accelerating voltage was employed during all SEM imaging. The working distance was maintained at approximately 2 mm for all the imaging experiments

4.2. Atomic Force Microscopy (AFM)

To complement the SEM images, AFM studies were performed. AFM has the added advantage of being able to provide quantitative information of sample topography that is, the heights and depths of surface features. AFM falls under the broader family of Scanning Probe Microscopy (SPM) techniques which include Scanning Tunnelling Microscopy (STM), Scanning Force Microscopy (SFM) and Scanning Near Field Optical Microscopy (SNOM) [Bow09]. Scanning probe microscopy techniques essentially involve the use of a very sharp probe to scan across a sample surface and then utilising interactions between the probe and surface to produce high resolution images.

The technique of AFM, was developed by Binning *et al*. of IBM Zurich from the need to broaden the imaging capabilities of their earlier invention, the STM. STM was limited to conductive surfaces and Binning *et al*. sought to extend it to non-conductive surfaces [Bin83, Bin86]. In the AFM, a very sharp tip, attached to a flexible cantilever, probes the repulsive and attractive forces between the tip itself and the sample surface to produce high resolution three-dimensional images of the sample topography [Bow09]. Its simplest forms are Contact Mode where the probe remains in constant contact with surface and Tapping Mode (Intermittent Mode), where the cantilever oscillates near the sample surface. In tapping mode the tip oscillations result in the probe engaging and disengaging from the sample surface potential field. Figure 4.5 illustrates the force-distance curves highlighting the regions of operation of the two modes. In contact mode, the net interaction between atoms of the probe and sample is repulsive due to electron shells of the respective atoms repelling each other. The magnitude of this repulsive force has a mean value of approximately 10^{-9} N [Zha09]. At

larger separations (in tapping mode) attractive van der Waals forces play a role in pulling the probe towards the sample surface.

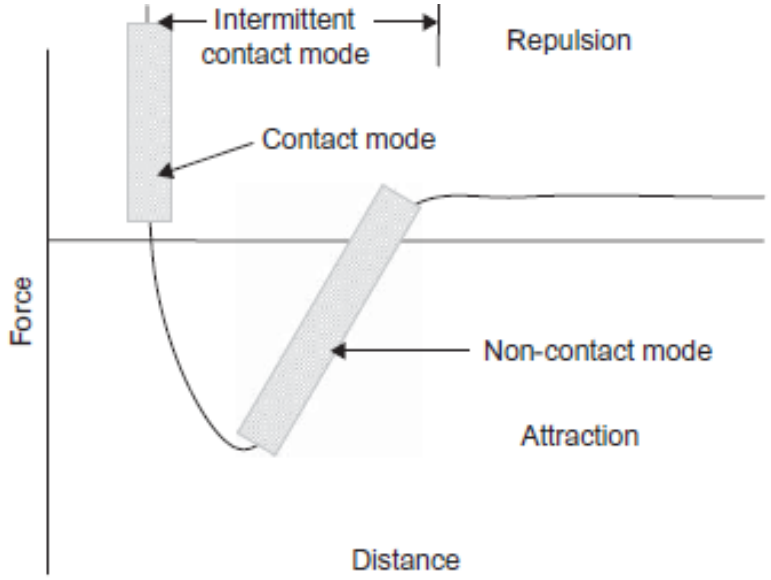

Figure 4.5: Force distance curve showing the two regimes. For contact mode, operated in the repulsive force regime, the sample stays in touch with the surface. In tapping mode, (attractive force regime), the probe oscillates very close to the surface, thereby repeatedly coming in and out of contact with surface. In a third mode , the non-contact mode, which is similar to tapping mode, the probe oscillates above the surface with a smaller amplitude but kept totally out of contact with the sample surface is also shown. Taken from [Bow09].

Contact mode is more suitable to hard surfaces and the taping mode is often used on soft samples to minimise sample degradation during probing. In this study, AFM has been carried out in contact mode using *Bruker's Dimension Icon* scanning probe microscope.

4.2.1. Basic principle of the AFM set up

Figure 4.6 illustrates the basic working principle of the AFM. In contact mode AFM, V-shaped cantilevers (figure 4.6 (b)) are normally employed for imaging. The cantilever is usually made of silicon nitride (Si_3N_4). At the free end of the cantilever, a sharp tip (made of wet-etched silicon) is attached and acts as the surface probe. The choice of these two materials is due to their high yield strength and elastic moduli [Bow09]. As the measurements depend on physical interactions between the probe and the sample surface, the

resolution of the AFM is ultimately a function of the probe's shape. Thus the radius of curvature at the apex of probe tip and the tips aspect ratio will determine its ability to resolve surface features [Bow09]. Lateral resolution is limited by the radius of curvature of the probe and hence surface features smaller than the contact area between the probe tip and sample will not be resolved successfully. The key factor here is the apex angle of the probe. AFMs have very good vertical resolution and resolution in the order of 0.01 nm is possible [Zha09] nowadays. Therefore the AFM is a powerful tool for extracting height information from sample surfaces. In this work, Si_3N_4 cantilevers with Si probes of tip radius ≤ 10 nm were employed for all measurements. High end research facilities and laboratories are working on using ultra-thin carbon nanotubes (radius of curvature < 1 nm) to optimize probe resolution [Zha09].

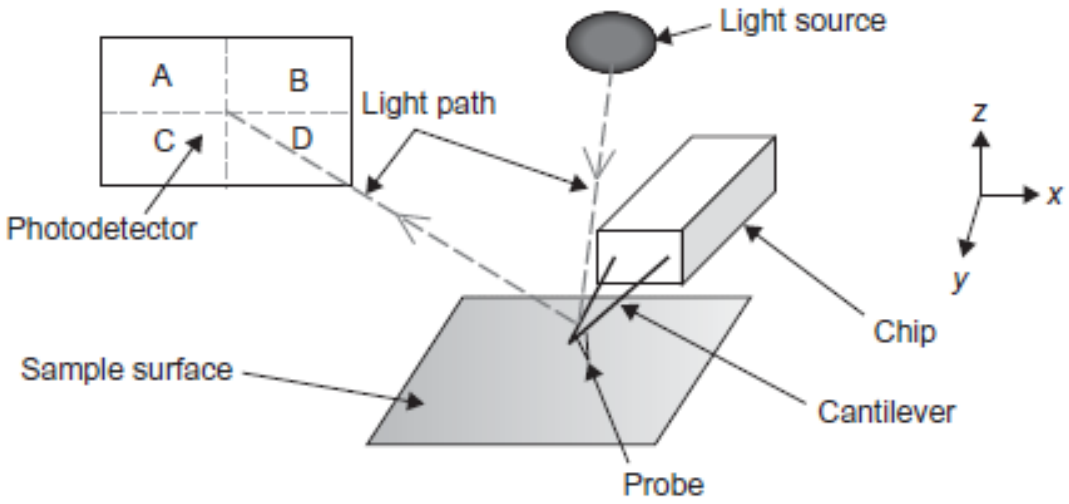

(a)

Figure 4.6: (a) General set up of an AFM. Taken from [Bow09].

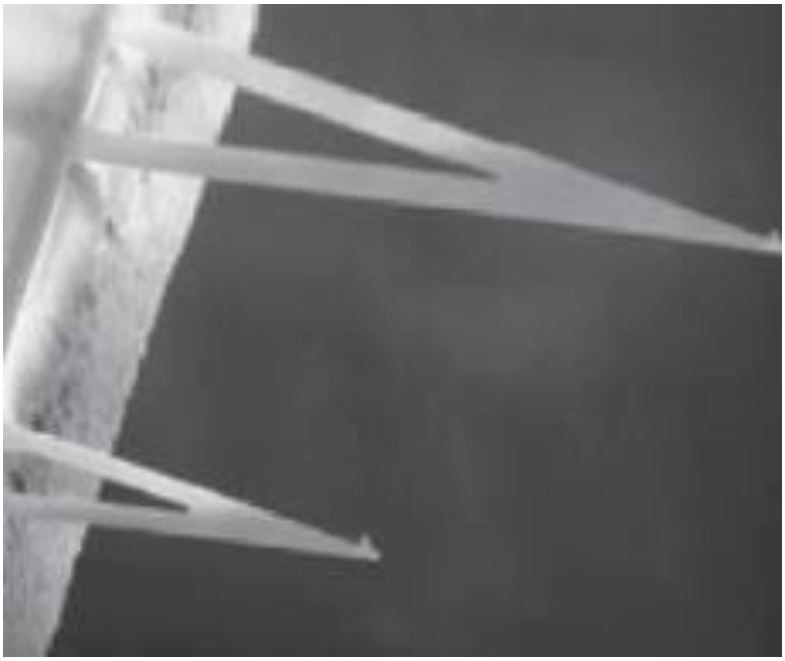

(b)

Figure 4.6 (b): An SEM image of two V-shaped cantilevers for contact mode imaging with the tip just visible at the end of one of the cantilever. Taken from [Bow09].

The cantilever is connected to a piezoelectric crystal which acts as the scanner responsible for movement of the cantilever via three perpendicular transducers in the x, y (lateral) and z (height) directions. The piezoelectric effect [Cur80], is the induction of expansion or contraction of a material upon application of a voltage and its bias. The top surface of the cantilever is coated with a highly reflective layer of either gold or aluminium. This reflective coating is used to deflect laser light from a light source to a position sensitive photodetector. As the probe tip is raster scanned over the sample surface, a deflection of the laser light due to the deflection of the cantilever as it scans the sample surface will then result in a change of position of the laser spot on the photo detector. The photodetector (figure 4.6 (a)), is a quadrant photo diode consisting of four parts with a horizontal and vertical line dividing it into sections A, B, C and D. The deflection signal is then calculated by the difference signal from A+B versus C+D quadrants [Bow09].

4.3 Atom Probe Tomography (APT)

The APT technique is fast becoming an indispensible tool for materials science analysis due to its outstanding atomic resolution (sub nm spatial resolution ~0.3 nm) [Mil01]. Driving this

surge in interest in the use of APT is its unique ability to identify and also quantify individual species in three dimensions [Cer07]. APT is often used to complement several techniques including Transmission Electron Microscopy (TEM) and Secondary Ion Mass Spectrometry (SIMS) [Cer07]. Of the three techniques just mentioned, APT has the added advantage of providing the highest spatial resolution of all [Cer07]. Advances made in Focused Ion Beam (FIB) milling techniques for sample preparation allow for site specific samples to be fabricated from areas of interest, for example, ion implanted zones in a material [Cer07,Mil12]. The power of three-dimensional ATP is illustrated by its ability to locate the precise positions of solutes in a material and structures in the material such as grain boundaries, other boundaries or interfaces, precipitation/phase separation and clustering [Mil00].

The technique of APT involves the ejection/release of ions through field evaporation of ions from a sample with tip of radius of ~50 nm and the projection of the ejected ions on to a position sensitive detector of diameter approximately 100 mm, yielding a very high magnification in the order of 10^6 [Cer07,Gna13]. Continued removal of ions results in depth profiling since the tip of the sample is eroded atom by atom; thus depth information is obtained directly from the order of evaporation [Vur11]. This enables the reconstruction of full three dimensional images of the tip and the location of atomic species along the full depth of the sample. The field evaporation is produced by the application of a high voltage (~10kV) which in turn generates a high electric field (~10^{10} V/m) [Cer07] on the apex of the sample which is at cryogenic temperatures of approximately 40 K. Pulsed evaporation enables the measurement of the time of flight of each ion and hence its chemical nature directly from its mass to charge ratio.

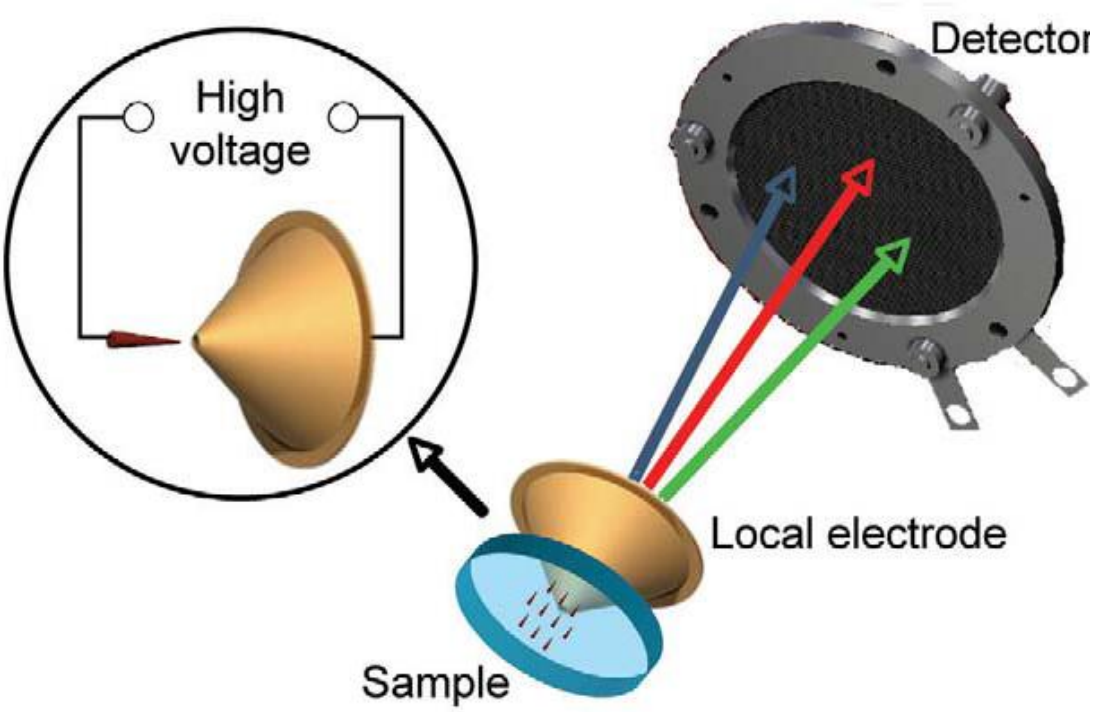

Figure 4.7: Illustration of a three-dimensional Local Electrode Atom Probe (Leap). Atoms are extracted from the apex of a sharp needle shaped sample by application of a high electric field between the local electrode and the sample. The ions are then attracted towards an imaging detector with their impact positions directly mapping the original atomic positions in the sample. Taken from reference [Cer07].

Evaporation by voltage pulsing limits the technique to conductive samples with a requirement of conductivity > 10^{2} S/cm [Cer07]. Atoms can also be extracted from sample tips using laser sublimation. In this so-called laser-pulsed mode, the laser beam is precisely focused and positioned by computer control to ensure that only the apex region of the tip is targeted for evaporation [Mil09]. Short pulses < 1 ns directed at the sample induce a pulse in the evaporation rate of any material regardless of conductivity [Cer07].

4.3.1 The physics of Atom Probe Tomography

Field evaporation breaks surface atom bonds and also causes ionization of the atoms. The evaporation which is material dependant occurs in two stages: 1. Thermally activated ions escape over an energy barrier, and 2. post field ionisation into higher charge states [Mil09].

The rate at which atoms escape from the surface is determined by the field evaporation rate constant *k* given in equation 4.4 as [Vur11]:

$$k = A\exp[-Q(F)/k_B T] \qquad 4.4$$

where, A is a pre-exponential factor, *Q(F)* is the field evaporation activation energy for escape into a charge state *s*, and $k_B T$ is the normal Boltzmann factor.

The mass to charge ratio *m/n*, is derived from the potential energy *neV* of the escaping ion. *V* here being the applied voltage between the local electrode (entrance to the mass spectrometer) and the specimen itself. The *m/n* is given by equation 4.5 and is expressed as [Mil00]:

$$\frac{m}{n} = cV\frac{t^2}{d^2} \qquad 4.5$$

where *c* is a constant, *V* is the total voltage on the sample and *d* is the flight distance. The time of flight *t*, is measured by applying a high voltage pulse to remove an ionised atom from the sample surface at a certain time. Since this voltage pulse is used to start the timing system, stopping the timer as the ionised atom hits a single atom detector yields directly the time of flight. Modern time of flight spectrometers have a timing resolution of 1 ns or better [Mil00].

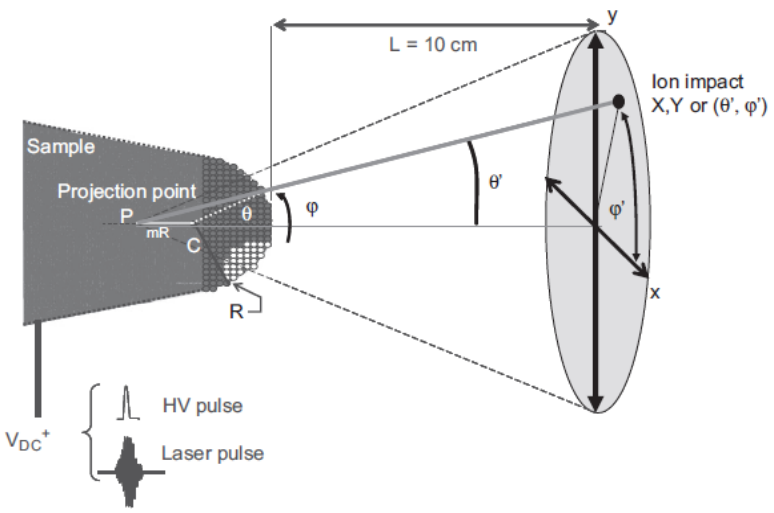

Figure 4.8: Illustration showing the principle of the evaporation and projection of ions in atom probe tomography. The sharp needle shaped sample it evaporated atom by atom. Evaporated ions are attracted to a position sensitive detector and the impact positions are used to derive the projected angles θ' and φ'. Taken from reference [Vur11].

The electric field F and the applied voltage V are related as shown in equation 4.6 by:

$$F = \frac{V}{\beta R} \qquad 4.6$$

here, β is a field factor influenced by the electrostatic nature of the sample and whose value is usually adjusted between 2 and 8 [Gom61] and R is the radius of curvature of the apex of sample. Image reconstruction is then achieved via point projection with point P (Figure 4.8) as the centre of projection. As illustrated in Figure 4.8, the point P is placed a distance mR from the centre of the apex of sample which is assumed to have a hemispherical tip end. m [Sou78,Vur11], is merely a compression factor ($0 < m < 1$) dependant on the electrostatic environment. When the axis of the tip is aligned with the centre of the detector, the impact positions can then be written in spherical coordinates (θ', φ') as illustrated in figure 4.8. These impact angles can are given by [Vur11]:

$$\varphi = \varphi'$$

and

$$\theta \approx (m+1)\theta' \qquad 4.7$$

with ($m+1$) defined as an image compression factor [Gau09].

From the above relations, the positions of the ion impacts on the detector can then be used to extract information on the original atoms positions in the sample (tip) using the following geometrical relations [Vur11]:

$$x = R\sin(\theta)\sin(\varphi)$$

$$y = R\sin(\theta)\cos(\varphi)$$

and

$$z = R(1-\cos(\theta)) \qquad 4.8$$

The magnification M defined by $M = \frac{L}{(m+1)R}$ where L is then distance from the sample tip to the detector.

Atom by atom evaporation ensures that depth information is simply extracted from the evaporation order. In this work, atom probe analysis was performed at the EMSL in a CAMECA LEAP 4000XHR system in electric field evaporation at a temperature of approximately 40 K. The base pressure was kept below 2×10^{-11} mbar throughout the evaporation. A 100 ρJ pulsed laser was employed during the evaporation. Field evaporation was achieved by steadily increasing the field from 500 V to approximately 6.5 kV.

4.3.2. Fabrication of the atom probe samples with a dual beam focused ion beam (FIB) instrument.

Samples prepared for atom probe tomography are generally sharp thin needle shaped specimens with an apex radius of less than 50 nm. It is desirable that the samples have a smooth shank with a taper angle of less than 5 ° [Mil05]. The FIB based Lift-out method developed originally for Transmission Electron Microscopy (TEM) [Mil05], offers the ability of preparation of samples at site specific locations. These locations are chosen by scanning and imaging over the region of interest on a sample in the electron microscope. The sites of interest can then be marked by depositing a layer of platinum of tungsten or by simply making a cut with an ion beam.

A platinum capping layer on 6H-SiC sample prepared by first electron beam assisted deposition and then gallium ion beam assisted deposition using a Helios Nanolab 600 FIB-SEM (EMSL, PNNL, Richland , USA) is shown in Figure 4.9 (a).

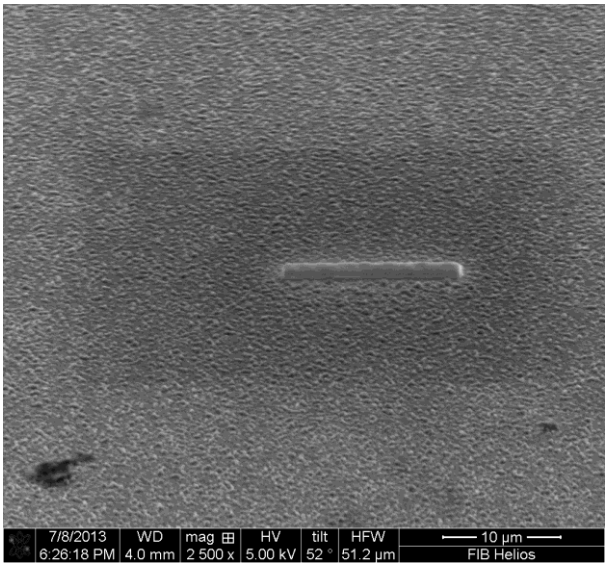

(a)

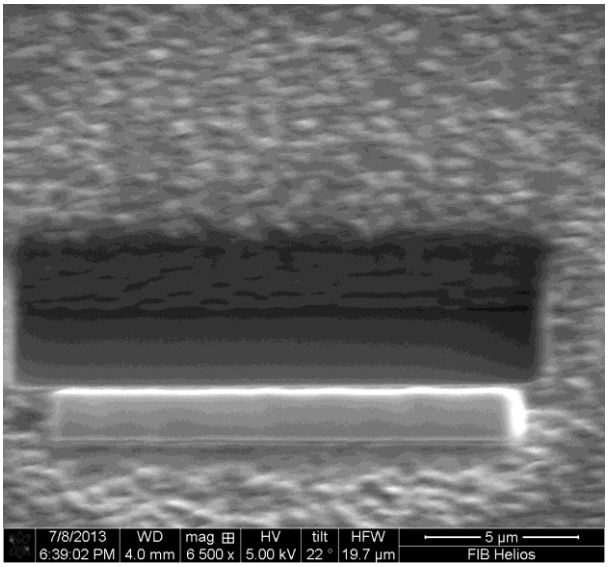

(b)

Figure 4.9: SEM images showing (a) a platinum capping layer applied to chosen site and (b) trenches milled around edges of capping layer.

A 5 keV , 2.7 nA electron beam was used to achieve the initial Pt coating layer of thickness 200 nm and with of 1,5 µm and length 15 µm. A 30 kV, 46 ρA gallium beam was later used

to extend the thickness of platinum capping layer to about 0.7 µm. The Pt capping layer is essentially a protective layer meant to protect the true sample surface during final ion milling sharpening of sample into the desired 50 nm radius at apex sharp needle. It was found that ion milling with gallium ions introduces gallium ions into the near surface layers of samples. At an energy 30 keV which is generally used in ion milling, the range of gallium ions in some materials ranges from 10~30 nm for low and high angle ion incidence [Gia04,Mil05]. The thickness of the capping layer also helps bring out *z*-contrast in backscatter SEM imaging ultimately aiding the user in distinguishing between the rest of the sample and site selected for analysis.

In the next stage of the lift-out procedure, a 30 kV , 2.7 nA gallium beam incident at an angle of 22 º relative to the specimen, was used to cut a slice 0.5 µm deep by scanning the beam from left to right to obtain the trench seen on the upper side of Figure 4.9 (b). The sample was rotated through 180 º to obtain the trench on the lower side as shown in Figure 4.9 (c). Throughout the cutting and milling, SEM imaging was performed in the dual beam instrument using a 2 kV ,0.44 nA electron beam.

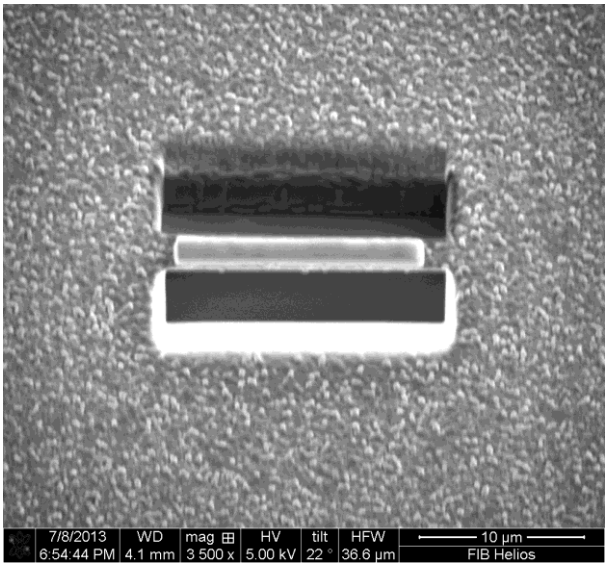

(c)

Figure 4.9: (c) SEM image showing trenches after milling on either side of platinum cap.

A nanomanipulator, (figure 4.10 (a)), was then inserted and placed so that it is in contact with one of the corners of the sample.

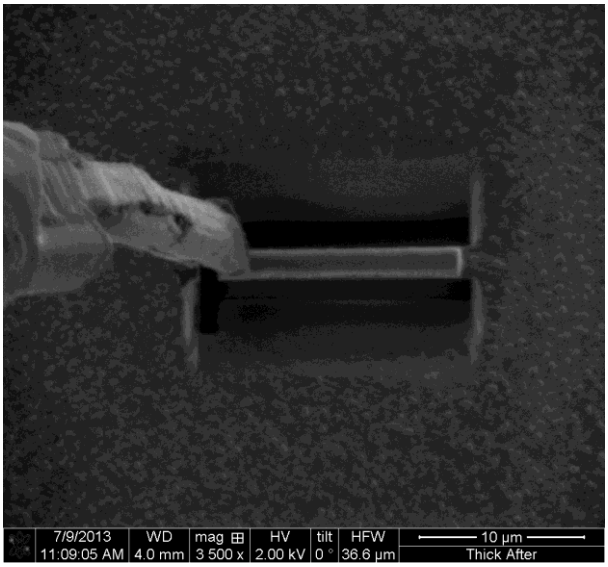

(a)

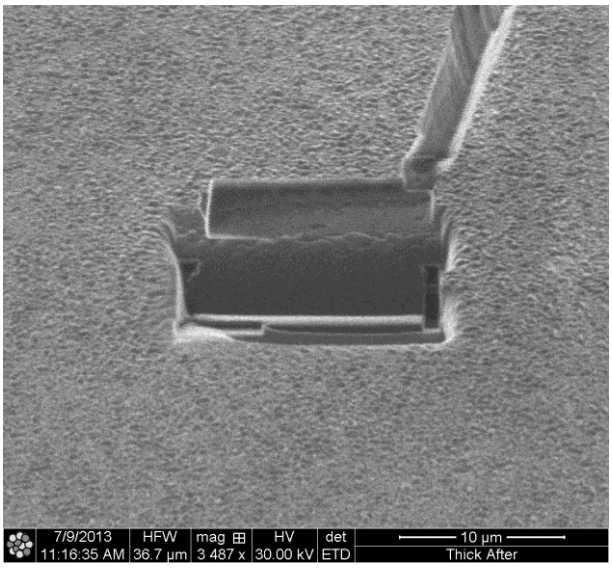

(b)

Figure 4.10: SEM images illustration the welding of sample to nanomanipulator (a) and lift out of specimen (b).

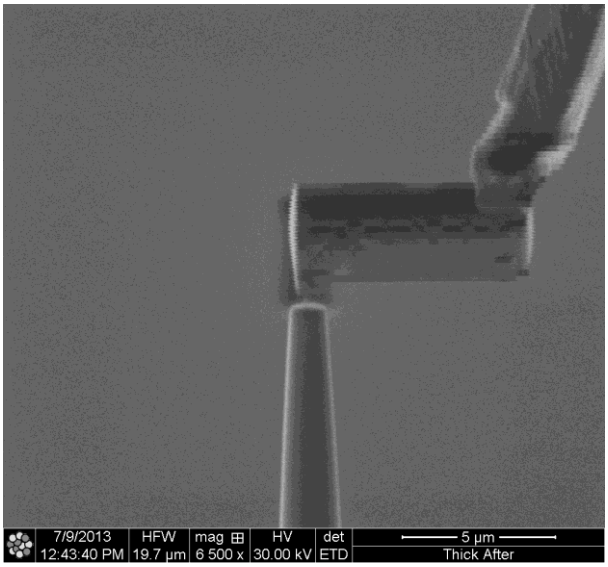

(c)

Figure 4.10 (c): welding of specimen to the holding post in preparation for annular milling

The nanomanipulator is a platinum gas injection needle used to secure the sample by the deposition of a Pt weld to the sample to itself. Once the sample was secured, the opposite end was cut by means of further gallium ion beam milling. The free end (figure 4.10 (b)) then allowed for the lift-out of the welded piece by the nanomanipulator. After the lift out procedure, the nanomanipulator was manoeuvred to position the sample onto a holding post where the specimen was again Pt welded to the post (figure 4.10 (c) and Figure 4.11 (a)). The sample was then milled into a sharp needle using an annular musk. For the annular milling, a 30 kV, 0.26 nA gallium beam starting with diameter of 4 µm. The sample was then progressively milled while reducing the milling diameter to 2µm, 1.5µm, 1.2 µm and finally 1.0 µm. The beam current was then reduced to 46 ρA and the milling diameter reduced to 500 nm and then to 400 nm. A 2kV gallium beam completes the annular milling by a applying a fine polish to the final specimen with the desired tip diameter of about 50 nm as shown in figure 4.11 (b).

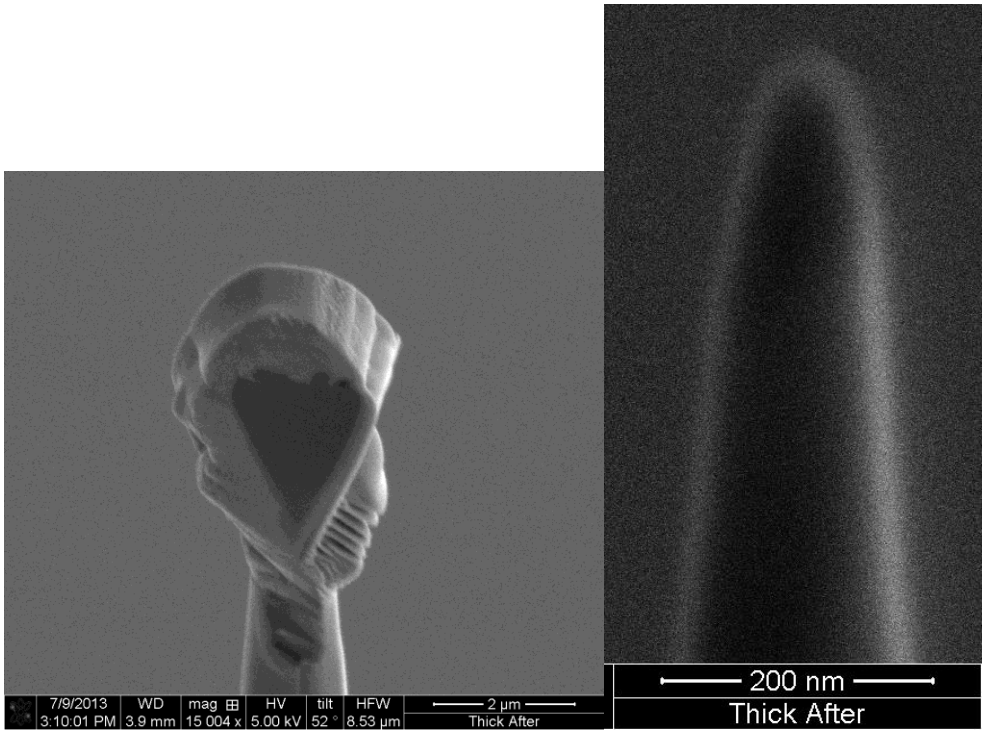

(a) and (b)

Figure 4.11: SEM image of specimen after platinum weld onto holding post (a) and final ATP tip after annular milling.

4.4 Rutherford backscattering spectrometry-Channelling (RBS-C)

Materials analysis by Rutherford backscattering spectrometry (RBS) involves a very simple principle where a beam of monoenergetic ions in the MeV range is projected towards a target and followed up by the detection of a small fraction of the ions that are scattered back from the target at a particular angle. The incident beam is usually made up of light ions ($^{4}H^{+}$ or $^{1}H^{+}$ or $^{7}Li^{+}$ ions). As discussed in chapter 2, as the ions penetrate the solid, they are progressively slowed down and stopped. However, a certain portion of the ions undergo close collisions with target atoms resulting in large angle scattering and large energy transfers. From these $<10^{-4}$ of the projectiles are scattered back and leave the target [Grob84]. The energy of these particles at a certain predetermined angle yields information on the nature, concentration and depth distribution of the target material.

4.4.1 The accelerator, scattering chamber and detector system-RBS experimental set up at the University of Pretoria

In this study, SiC samples implanted with several of the significant fission product elements were used as the target materials mounted on a sample stage fitted on a 3 axis goniometer. The impinging ion beam was made up of helium ions. The charged helium ions were generated by an RF-source and accelerated to high energies via a large potential difference across an accelerating tube based on the principles discovered by Van de Graaff [Gra11]. A schematic of a typical a Van de Graaff accelerator and RF ion source are shown in Figure 4.12 (a) and (b) below.

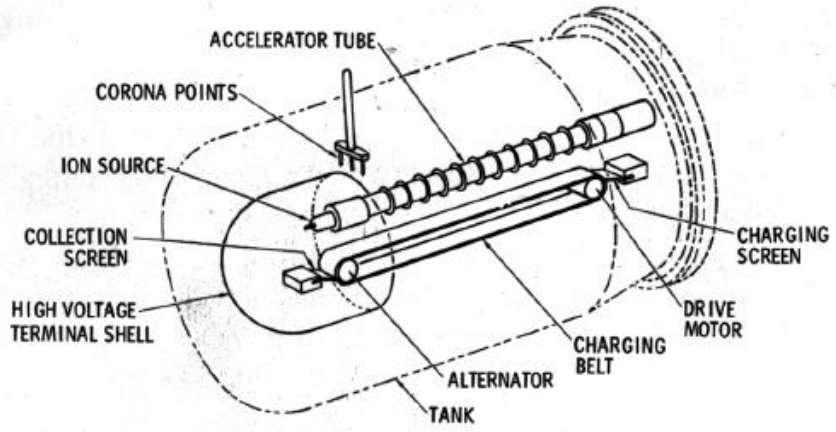

(a)

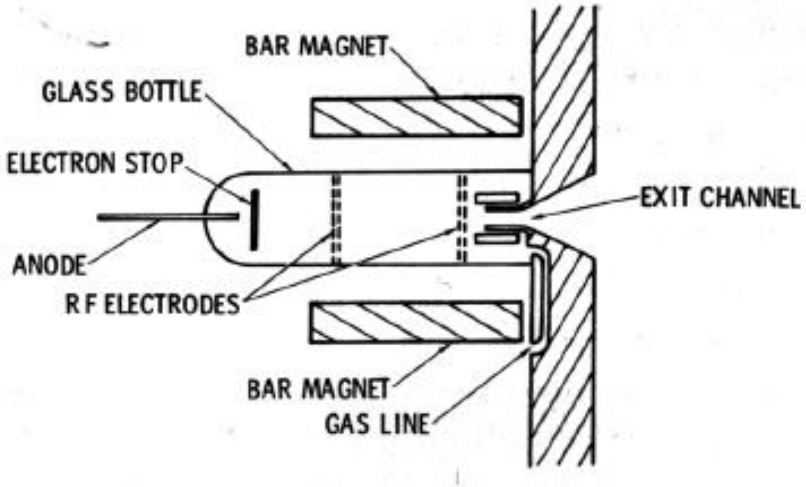

(b)

Figure 4.12: Schematic of a Van der Graaff accelerator (a) and an rf ion source (b). Taken from [Chu78].

In this thesis, a 2.7 MeV Van der Graaff accelerator of the University of Pretoria was used for ion acceleration. The ion energies employed in this work were 1.2, MeV, 1.4 MeV and 1.6 MeV. Figure 4.13 illustrates the experimental set up of the RBS measurements at the University of Pretoria. Shown here are the accelerator tank, analysing magnet, beam lines and the scattering chamber.

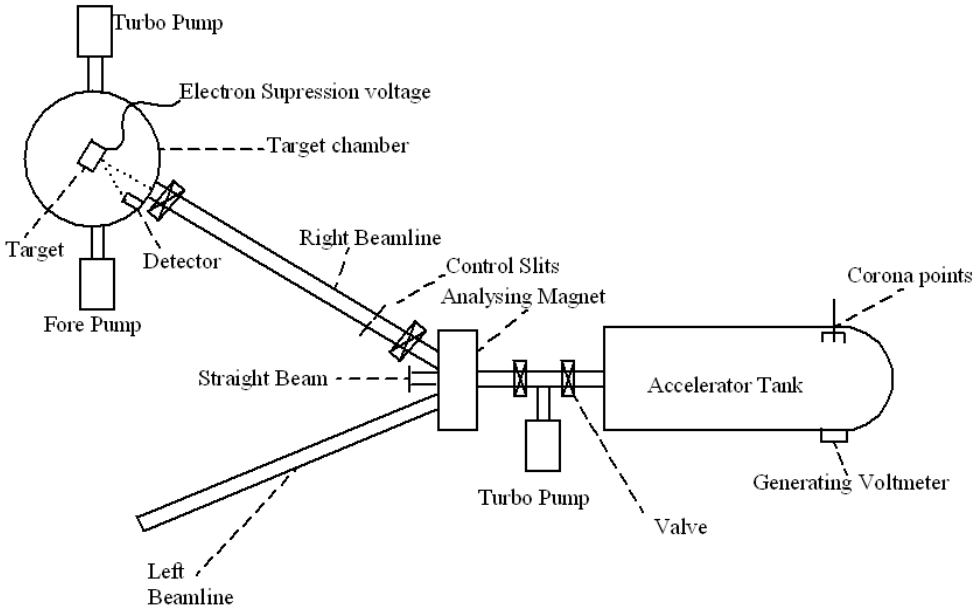

Figure 4.13: Illustration of the Van de Graaff accelerator at the University of Pretoria in the RBS set-up.

Enclosed in the accelerator tank are the ion source, charging belt, accelerator tube and the components making up the electrostatic environment of the particle accelerator. The tank is then filled with an insulating dry gas. The dry gas is usually made up of a mixture of N_2 and CO_2 or SF_6 [Gro31]. At the University of Pretoria mixture of N_2 and CO_2 is used for insulation. On exiting the tank, the ion beam is energy analysed using an electromagnet which deflects the beam into either beam line 1 (left beam) or beam line 2 (right beam).

Immediately after the magnet (right beam line) are a set of horizontal and vertical slits. The slits aid in the production of a monoenergetic beam by filtering out any unwanted species and allowing only ions at a particular energy to pass through as determined by the energy flight paths of the ions. In this case helium ions were used as the analysing beam. A collimator inside the scattering chamber finally shapes the beam into a specific size before it reaches the target sample. In this work the beam spot was collimated to an area of approximately 2 mm^2. The samples are mounted on a stainless steel sample holder fitted to a 3 axis goniometer which has a precision of approximately 0.02º for each axis. During measurements, secondary electrons which distort readings are suppressed by an applied negative voltage of 200 V connected to a ring shaped electrode placed in front of the target.

4.4.2 The physics of RBS

The technique of RBS evolved from the understanding of the binary collision mechanisms proposed by Rutherford [Rut11] and first ion backscattering experiments by Geiger and Marsden [Gei13]. After the Second World War, nuclear physicists employed backscattering techniques for determining the presence of contaminants on samples [Gro84]. The realisation that the detection and measurement of the number and energy of ions in a beam backscattered yields quantitative information on the sample led to its wide spread adoption across many industries ranging from chemical analysis of impurities in metals to the silicon device industry. The quantitative power of RBS arises from the four major effects associated with charged particle backscattering. These are namely [Chu78,Gro84,Tes95]:

i. The elastic two body collision between an incident particle and a target atom leading to the possibility of mass separation via a kinematic factor.

ii. The probability of such an event to occur (differential scattering cross section)

iii. The energy loss of the projectile ions in the target (stopping cross section yielding information on depth)

iv. The statistical dispersion in the energy loss (energy straggling resulting in the limitation to the extent of mass and depth resolution, discussed in chapter 2).

4.4.3 The kinematic factor

For an elastic collision, the energy of a backscattered particle (E') is calculated from the principle of conservation of energy and momentum according to [Chu78,Tes95]:

$$E' = KE = \left[\frac{M_1 \cos\theta \pm (M_2^2 - M_1^2 \sin^2 \theta^{1/2}}{M_1 + M_2} \right]^2 E \qquad (4.9)$$

where E is the energy of the incident particle, θ is the backscattering angle and K is the kinematic factor.

From equation 4.9, the kinematic factor is therefore the ratio of the projectile energy after collision, E', to that before collision E. For a fixed backscattering angle (165º in our scattering chamber), K depends only on the mass ratio M_1/M_2. Therefore the technique of RBS is used to identify the constituents of a sample as the incident particles with the same incident energy and angle will backscatter of different masses with different energies. There are however some limitations to mass resolution with depth. These include the spread in the incident energy beam, the solid angle of the detector and the beam size. To improve mass resolution, a higher mass element in the projectile beam but one not larger than the target mass atoms can be used. In our RBS set-up, He ions are preferred over heavier ions such as Li as the use of heavier mass elements results in more radiation damage in the substrate.

4.4.4 Depth profiling

Backscattered particles will also have different energies when scattered from different depths. As illustrated in figure 4.14, a particle backscattered from the target surface possesses energy equal to KE_0 while one scattered at a depth x will have energy E lower than E_0 when it scatters at that depth due to loss in the projectiles energy on its inward path. This inward path length from figure 4.14 will be equal to $x/\cos\theta_1$. After the backscattering event at depth x the projectile has energy of KE. This ion will also experience energy losses on its way out of the target on a path length $x/\cos\theta_2$ as shown in figure 4.14.

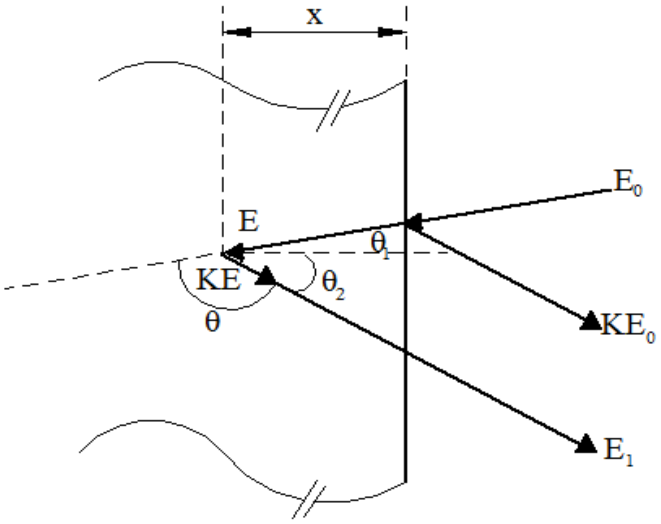

Figure 4.14: Energy loss components representing backscattering events from the surface and from a depth x within the target. Redrawn from [Chu78].

The total energy loss of a particle scattered at depth *x* has been derived by assuming that the energy loss *(dE/dx)* stays constant along the inward and outward paths (surface approximation) [Chu78,Tes95] and this energy loss relationship is shown in equation 4.10:

$$\Delta E = KE_0 - E_1 = [S]x \qquad 4.10$$

Where [*S*] is the energy loss backscattering factor given by

$$[S] = \frac{K}{\cos\theta_1}\frac{dE}{dx}(in) + \frac{1}{\cos\theta_2}\frac{dE}{dx}(out) \qquad 4.11$$

This energy loss factor carries the information relating the energy to the depth information. It is therefore used to convert a measured energy spectrum directly to a depth scale. Energy to depth conversions are performed using numerically tabulated values of stopping powers [Zie77]. In this thesis, the computer code Stop5 [Fri12] has been used to calculated the energy loss factors.

For compound targets such as SiC, the energy loss is calculated by taking into consideration Bragg's rule of the linear additivity of the stopping cross sections of all the elements making

up the target. For a binary compound defined as A_mB_n, the energy loss of a particle backscattered from element A at depth x can be written as:

$$\Delta E_A = [S]_A^{A_mB_n} x = \left(\frac{K_A}{\cos\theta_1} \frac{dE}{dx}(in) + \frac{1}{\cos\theta_2} \frac{dE}{dx}(out) \right) x \qquad 4.12$$

And for element b

$$\Delta E_B = [S]_B^{A_mB_n} x = \left(\frac{K_B}{\cos\theta_1} \frac{dE}{dx}(in) + \frac{1}{\cos\theta_2} \frac{dE}{dx}(out) \right) x \qquad 4.13$$

Here K_A and K_B are the kinematic factors of elements A and B in the compound.

From Bragg's rule (defined in section 2.1.3 of chapter 2) the total energy loss is then given by:

$$\Delta E = [S]^{A_mB_n} x = \frac{m}{m+n}[S]_A^{A_mB_n} x + \frac{n}{m+n}[S]_B^{A_mB_n} x \qquad 4.14$$

4.4.5 The differential cross section

As mentioned in introduction of section 4.4, only a small fraction of the incident particles are backscattered. The probability of a backscattering event at a particular solid angle occurring is expressed by the concept of the differential cross section. This cross section is defined as the number of incident particles scattered into the solid angle $d\Omega$ per number of incident particles per unit area. This differential scattering cross section connects the backscattering yield to quantitative analysis. In backscattering spectroscopy [Gro84,O'Co03], where the energy of the ion beam is usually in the 1 to 4 MeV range, the distance of closest approach between the projectile ion and target atom is considered to be large when compared to nuclear dimensions. Albeit this, the distance is still taken to be small as compared to the Bohr radius (0.53 Å). In this case the interaction between the projectile ion and target atom nuclei can the considered to be an unscreened coulomb repulsion between two positively charged nuclei. The Rutherford differential cross section can then be applied and this is given by equation 4.15 below [Fel86,Chu78]:

$$\frac{d\sigma}{d\Omega} = \left(\frac{Z_1 Z_2 e^2}{4E} \right)^2 \frac{4\left(\sqrt{M_2^2 - M_1^2 \sin^2\theta} + M_2 \cos\theta\right)^2}{M_2 \sin^4\theta \sqrt{M_2^2 - M_1^2 \sin^2\theta}} \qquad 4.15$$

$Z_1$is the atomic number of the projectile ion of mass M_1, Z_2 is the atomic number of a target atom of mass M_2, e is the electronic charge, E is the energy of the ion immediately before scattering and θ is the scattering angle.

Equation 4.15 shows that the Rutherford backscattering probability depends on the square of the atomic number of the projectile ion as the yield increases with atomic number. The cross section is also influenced by the target atom atomic number Z_2, and as such RBS is much more sensitive to heavy elements. The differential cross section is inversely proportional to the square of the energy and thus the backscattering yield decreases sharply with increasing energy. The total number of detected particles (Y) backscattered from a volume element of atoms representing one channel in a thick target [Fel86] is given by:

$$Y = \sigma\Omega QN \qquad 4.16$$

where Q is the total number of incident particles determined by the time integration of the current of charged particle incident on the target, Ω is the detector solid angle, σ is the scattering cross section and N is the total number of target atoms per unit area. From the experimental set up and theory, Q, Ω, σ and Y can be found or are known and hence N can be calculated leading to quantification of the experimental results.

4.4.6 Rutherford backscattering combined with Channelling (RBS-C)

The alignment of an ion beam with a low index direction (axial alignment) [Bir89] can result in approximately 95% of the incident ions being channeled resulting in a corresponding decrease of the yield of backscattered ions from small impact parameter interaction processes. Planar alignment results in a higher backscattering yield of about 30% of the normal (random) yield. Figure 4.15 shows the normalized yield of backscattered particles for planar and axial channeling.

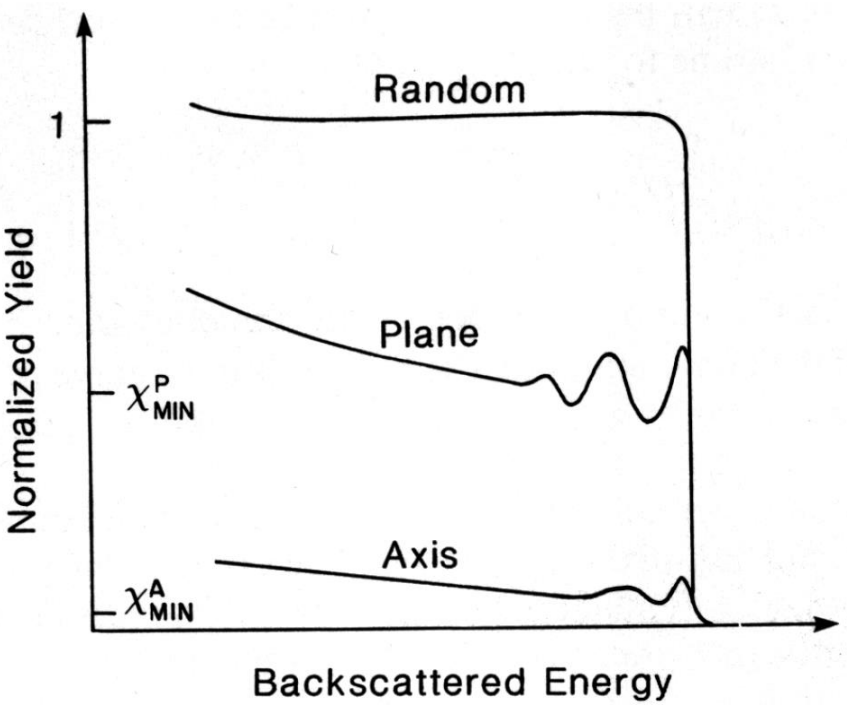

Figure 4.15: RBS/Channeling spectra of axial and planar channeling. Taken from [Bir89].

Experimentally, crystal alignment [Gro84], is performed by placing the sample at the centre of high precision goniometer. Such a goniometer allows one to tilt and rotate the sample about two or three axes. The stepping motors of the goniometer can make movements with an accuracy of about 0.01° [Gro84]. The incident beam will be aligned with successive lower index planar directions when moving the goniometer. A stereographic projection of the crystal can then be constructed from the positions of the planar minima obtained during the angular scan. The angular yield about axial and planar channels is shown in figure 4.16. In Figure 4.16, $\chi_{\min}$ is the minimum yield which corresponds to the minimum random component of the beam as it enters the crystal and $\psi_{1/2}$ is the angular half width at half height of an angular scan – see Figure 4.16 [Bir89].

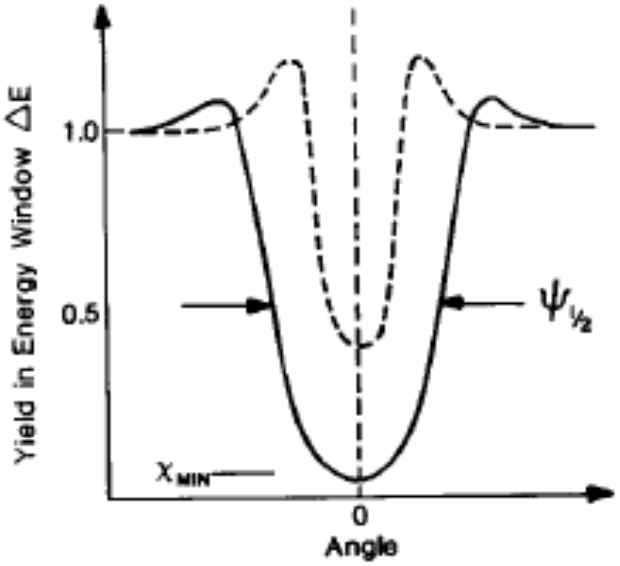

Figure 4.16: The angular yield about an axial channel (solid curve) and a planar channel (broken line). Taken from [Bir89].

The channeling process is very sensitive to small departures from the crystalline structure of a medium. Crystal defects such as displaced lattice atoms, substitutional impurities and interstitial atoms blocking channels can cause dechannelling to occur (figure 4.17). In this case there will be a corresponding increase in the yield of backscattered particles.

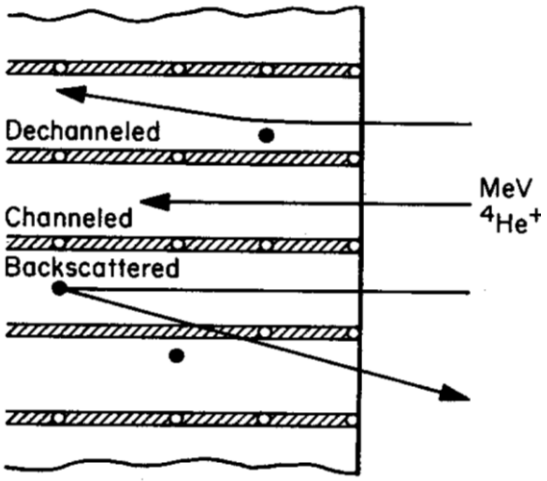

Figure 4.17: Schematic showing the dechannelling and direct backscattering of ions by interstitial atoms blocking a low index direction (channel). Taken from [Chu7].

Channeling techniques combined with the randomly aligned beam in conventional RBS provide information on the amount and depth distribution of lattice disorder in the near surface region of materials and on the thickness of amorphous layers. The backscattered yield about an axial channel from a perfect crystal or an un-implanted sample (virgin sample), is very low as compared to the yield about a random direction (figure 4.15). Radiation damage production in crystals during ion implantation can be determined by comparing the aligned yield after irradiation with the yield in a random direction. The aligned backscattering yield in general, increases from the levels of the virgin crystal with increasing defect concentration. The production of defects depends on the irradiation conditions like the fluence and irradiation temperature. In RBS [Wes95], the absence of long range order or amorphisation is defined by a relative defect concentration which is equal to unity, which means that the aligned yield reaches the random level. In some cases during ion implantation, the need arises to limit the probability of the channeling of ions incident on a target material. This is usually done by ensuring that the angle of incidence is approximately 7° off axis or by pre-amorphising the near surface region of the crystalline solid.

4.4.7 Data acquisition in RBS

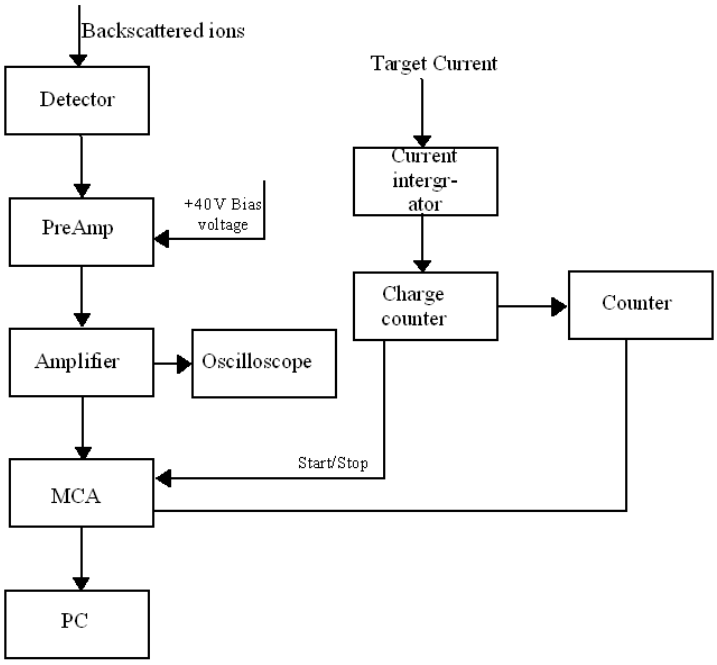

Figure 4.18: Block diagram of the energy spectrometry system used at the University of Pretoria.

The electronic set up of the University of Pretoria's RBS system is shown in figure 4.18. The backscattered α-particles are detected by a Canberra passivated implanted planar silicon (PIPS), partially depleted (PD) surface barrier detector with an active area of 25mm^2 located at an angle of 165° relative to the incident beam. An output charge signal from the detector, which is proportional to the energy of the backscattered particle, is fed into a Canberra 220 pre-amplifier. A +40V bias voltage from a Canberra 3102D high voltage supply is supplied to the detector. This voltage ensures that the depletion region in the detector is thick enough to stop higher energy particles. In the pre-amplifier the charge signal is converted into a voltage signal proportional to the backscattered energy. This voltage signal is then further amplified by a Tennelec TC 243 amplifier. From this main amplifier, a bipolar output signal is fed to an oscilloscope to monitor the shape of the output pulses. Meanwhile, a unipolar output signal from this main spectroscopy amplifier is fed to the input of a multichannel analyser (MCA).

A current is simultaneously collected at the back of the target and delivered to an Ortec 439 current integrator. A logic signal from the current integrator is responsible for initiation and termination of signal processing by both the MCA and the counter. A desired energy range can be selectively processed by adjusting the lower and upper energy discriminators in the MCA.

The sample orientation can be varied during the experiment by making use of a precision three axis goniometer. This goniometer is used extensively in the channelling experiments. The use of the goniometer in channelling experiments is outlined in the previous section on channelling (section 4.4.6).

4.4.8 Data Analysis

The backscattering energy spectra of counts against channel number were obtained by collecting a charge of 8 μC constituting a run. Several runs performed for each sample and the average of these runs used for better statistics. In order to obtain the energy per channel calibration of the system, backscattering spectra were obtained for runs at three energies. These energies were 1.6 MeV, 1.4 MeV and 1.2 MeV. The positions of channel number of the silicon edge at the different energies were plotted against the corresponding energies. The slope of this plot gives the energy calibration of the system in keV/channel. This energy calibration in keV/channel was then converted into a depth scale calibration in nm/channel, using the computer code STOP5 [Fri12]. As stated earlier, the code STOP5 uses the energy loss data of Ziegler [Zie77].

The moments R_p, the projected range, and σ, the range straggling or standard deviation of the implanted profiles were obtained by fitting the resulting spectra of counts against depth (nm) with the computer program GENPLOT as outlined in section 2.3 of chapter 2. The standard deviation,σ, can be related to the full width at half maximum (FWHM) [Chu78], of a Gaussian distribution by

$$FHWM = 2(2\ln 2)^{1/2} \times \sigma \qquad (4.17)$$

In this study, the FWHM's of the depth profiles after iso-thermal annealing were fitted to the function

$$[W(t)]^2 = 4Dt\ln(2) + [W(0)]^2 \qquad (4.18)$$

to obtain D

4.5 Time-of-Flight -Heavy Ion Elastic Recoil Detection Analysis (ToF-ERDA)

Much like RBS, Elastic Recoil Detection Analysis (ERDA) is an ion beam technique that depends on four basic physical concepts [Tes95] namely:

i. The kinematic factor which details the energy transfer from a projectile to a target atom in an elastic collision thereby ejecting the target atom which is subsequently detected.
ii. The differential scattering cross-section that shows the probability for the occurrence of a scattering event.
iii. The stopping powers that outline the average energy loss of the projectile and also the recoil target atom as they move in the sample and hence establishing a system for obtaining a depth scale.
iv. The energy straggling that gives the statistical fluctuations in the energy loss.

4.5.1 ToF-ERDA set-up at the iThemba Labs, Gauteng 6Mev Tandem Accelerator

The basic principle of Heavy Ion-ERDA is centred on the detection of recoil atoms knocked of the first few 100s of nanometres of a target surface by a projectile beam of heavy ions at grazing angle incidence. It is essentially then a forward scatter technique. In this study, a 26 MeV Cu^{7+} ion beam, projected at a 20º grazing incidence angle to the target surface was employed. The tandem accelerator is equipped with a sputter ion source with cesium gas as the source of sputter ions. A typical experimental configuration of the ERDA set-up is shown in figure 4.19.

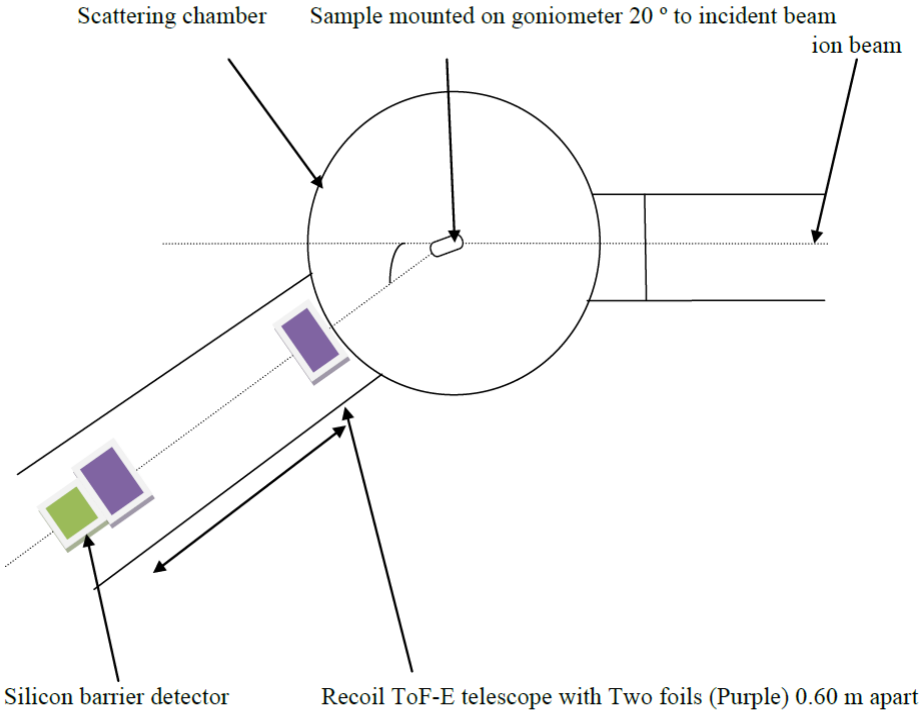

Figure 4.19: A typical experimental set-up of the mass and energy dispersive time of flight (ToF)-ERDA. The sample was aligned at an angle of 20º to the incident ion beam via a goniometer. The scattering angle was 30º. The purple blocks are carbon foil based timing detectors separated by a 0.60 m flight path. Behind the second foil is the silicon surface barrier detector (green block). The signal processing electronics (not shown) consists of the standard nuclear instrument modules including constant fraction discriminators, a time-to-digital converter and an analogue-to-digital converter for the Si surface barrier detector. Redrawn from reference [Tes95].

A mass dispersive ToF spectrometer made of two carbon foil based MicroChannel Plate (MCP) time detectors 0.6 m apart and a PIPS semiconductor energy detector located at the end of the flight path (behind second time detector) were employed in a coincidence measurement. The coincidence measurement of the time of flight and the energy of the recoils leads to the elemental separation of the recoil atoms according to mass. The mass curves are derived from relationship between the energy and the time of flight coordinates (t,E) [Kot06] as described by:

$$M = c(E - E_0)(t - t_0)^2 \qquad 4.19$$

where M is the mass of the recoil, t and E are the time and energy coordinates in the ToF vs Energy two-dimensional scatter plots and E_0 and t_0 and c are calibration constants. The ToF axis can then be converted into a linear energy axis via a re-binning of energy events [Msi13]. The elemental linear energy spectra can be converted into elemental depth profiles via a direct calculation using the transformation algorithm KONZERD [Ber95]. Developed from algorithms earlier developed for RBS [Ber95], KONZERD is used to solve, by iteration, the information on the number of events for each particular slice of depth (depth interval Δx) that in turn corresponds to an energy band. The relative atomic concentration n_i of element I is found from two independent equations. One way is first from the number of counts Y_i scattered from a depth interval Δx as given by [Ber95]:

$$Y_i = n_i \left(\frac{d\sigma}{d\Omega} \right) N_P \Delta\Omega \frac{\Delta x}{\sin \alpha} \qquad 4.20$$

Where $(d\sigma/d\Omega)_i$ is the differential cross-section defined earlier in section 4.4.5, N_P is the primary beam dose, α is the angle of incidence and $\Delta\Omega$ is the detector solid angle.

Secondly, further information is obtained from the energy interval ΔE_i in which i particles are scattered from depth interval Δx is given by [Ber95]:

$$\Delta E_i = \Delta x S_i(x) \qquad 4.21$$

$S_i(x)$ here is the energy loss factor for a depth x including contributions from the stopping of both the projectile and the recoil. Taking into account the linear additivity of stopping powers from Bagg's rule, this energy loss factor is given by [Berg95]:

$$S_i(x) = \sum_{j=1}^{m} n_j \left[K_i \frac{(dE_P / dx)^j}{\sin \alpha} + \frac{(dE_i / dx)^j}{\sin \beta} \right] = \sum_{j=1}^{m} (n_j a_{ij}) \qquad 4.22$$

where m is the number of elements in the target, $(dE_P/dx)^j$ and $(dE_i/dx)^j$ are the stopping powers of the projectile (p) and recoil (i) in element j respectively, K (defined in section 4.4.3 of RBS) is the kinematic factor of the recoil Ii. A system of linear equations for each slice of thickness (depth interval) is then found by diving equation 4.20 by equation 4.21 resulting in:

$$\frac{Y_i}{\Delta E_i} = \frac{n_i}{\sum_{j=1}^{m} n_j a_{ij}} c_i \qquad 4.23$$

Here c_i is a constant composed of the cross sections, the beam current and the detector acceptance angle [Berg95].

4.6 Secondary Ion Mass Spectrometry (SIMS)

Secondary ion mass spectrometry has become one of the most widely used and accepted techniques for analysis of trace elements in solid materials. Its popularity stems from its fast element mapping, high sensitivity for trace elements, accurate isotopic measurements and excellent depth resolution [Por07]. Depth resolution in the nm range is achievable with SIMS along with a lateral resolution below 0.2 µm and a trace element detection limit of the order of 1ppb (parts per billion) [Por07].

4.6.1 General principles of SIMS

The SIMS technique is centred on the bombardment of a sample surface by a primary ion beam and the detection of the masses of the sputtered particles from the target sample.

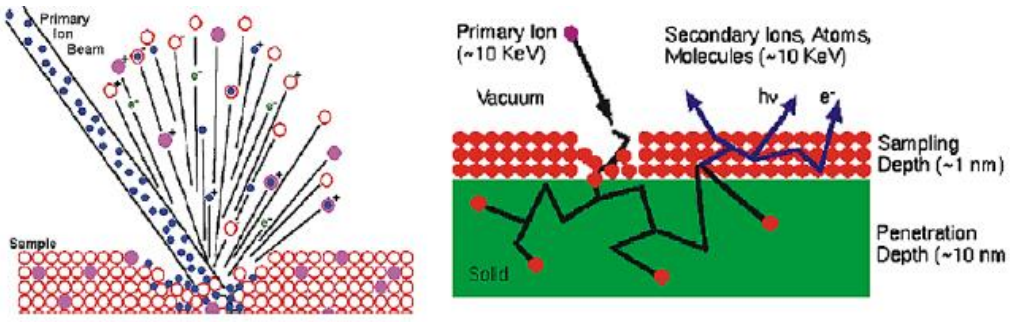

Figure 4.20: Secondary ion generation. Taken from Reference [Jai11].

In this study, SIMS was performed in the Dynamic SIMS mode which takes advantage of the destructive nature of the impinging ions to extract depth information. During analysis, the sample surface is continuously sputtered away. In this dynamic mode, depth profiles are then obtained by recording the secondary ion current as a function of time with the time scale

subsequently converted into a depth scale by calibration. Therefore the chemical information of the sample as a function of depth can be determined as the sample is eroded with time.

The interaction of the primary beam the target with atoms is best described via a collision cascade model. The model assumes that each primary ion transfers energy to target atoms in a series of binary collisions and the energetic target atoms known as recoils then collide with more target atoms. Some of the target atoms recoil back through the sample surface and it is these recoils that form the sputtered material. Details of ion-solid interactions have been reviewed in chapter 2 of this thesis.

Several species are used traditionally as the primary beam specie in SIMS analysis. These include Cs^+, O_2^+, Ar^+ and Ga^+ at energies ranging from 1 to 30 keV. At these energies some of the ions of the sputter beam end up being implanted in the sample. The range of these primary ions can be up to depths of 10 nm.

4.6.2 Secondary Ion Yield

The number of sputtered atoms that become ionized give what is known as the secondary ion yield. The ion yield depends on the elements in the target and is influenced by the ionization potential for positive ions and electron affinity in the case of negative ions [Vic89]. For example, it is known that oxygen bombardment increases the yield of positive secondary ions while cesium bombardment increases the yield of negative secondary ions [Vic89]. With oxygen bombardment, the concentration of oxygen in the surface layer increases. Metal-oxygen bonds that form in this region break during ion emission leaving oxygen negatively charged and metal positively charged [www1]. For cesium bombardment, the material work functions are reduced due to cesium implantation. An increase in secondary electrons being excited over the surface potential barrier leads to negative ion formation [www1].

Equation 4.24 below [Fel86,O'Co03], gives the secondary ion yield *Y'* (of particular charge, say, the yield of positive or negative ions) of a given element *A*.

$$Y' = \int_0^{E_m} \alpha(E) Y(E) dE \qquad 4.24$$

where α is the ionisation probability which depends on the sample composition, Y is the total yield of sputtered particles (neutral or charged) per primary ion impact which is also target material dependant and E_m is the maximum energy of the sputtered particles.

The measured current of secondary ions (of particular type) from element A in the target is given by equation 4.25 [Fel86].

$$I_A = C_A I_p \beta T \alpha(E,\theta) Y(E,\theta) \Delta\Omega \Delta E \qquad 4.25$$

where C_A is the concentration of A, I_P is primary beam current, β is the sensitivity of detector, T is the transmission of the system for the ion species measured, α is the ionisation probability, $\Delta\Omega$ and ΔE are the solid angle and with of the energy filter and θ and E are the angle and pass energy of the detector system.

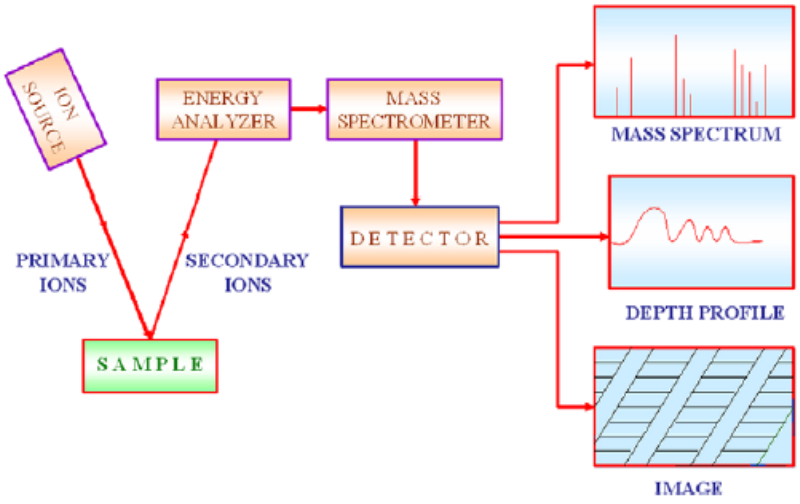

Figure 4.21: A typical set up of a SIMS experiment. Taken from reference [Jai11]

4.6.3 Mass Spectrometry

A key component of the SIMS set-up is the mass spectrometer. Several methods of mass spectrometry are available as options for use in SIMS analysis. In this work we have employed the now more common mass spectrometry technique in the SIMS community which is the Time-of-Flight Mass Spectrometer (ToF). In this work SIMS work was

performed on a ToF-SIMS 5 instrument at the EMSL, PNNL, Richland USA. In the ToF spectrometer system, ions are accelerated to a given potential so that the ions all have the same kinetic energy [Vic89]. In this scenario, ions of different mass:charge ratio will then have different velocities. Once the ions enter into a field free drift space, the ions spread out with heavier ions arriving later than lighter ones [Vic89]. A time sensitive detector system will then be employed to produce the mass spectrum.

4.6.4 Depth Profiling in SIMS

Depth profiling in SIMS analysis is achieved by monitoring the secondary ion count of desired elements in the target sample with time. The time axis is then converted into a depth scale if the sputter crater dimensions and sputter rate are known. In this work, a 2 kV Cs^+ beam was employed as the sputter beam to sputter a 300 μm area. The sputter area and depth were analysed by a profilometer. The sputter rate for the SiC samples was found to be 0.00280 nm/nA.s. For a secondary ion current of 168 nA (as measured by Faraday cup), the depth in nm was then calculated by multiplying the sputter rate by the secondary ion count and the total time.

4.7 X-ray Photoelectron Spectroscopy (XPS)

Siegbahn *et al.* (see [Vic97] for an historical introduction) led the development of a new surface analysis technique in the 1960s with the aim of measuring the elemental composition, chemical stoichiometry, the chemical state and the electronic state of the elements in a material [Zha09]. The technique is based on the analysis of the kinetic energy of electrons emitted by a material when monochromatic radiation (in this case X-rays) is used to excite the electrons in the material. The emitted electrons are known as photoelectrons and when their energies are analysed and plotted, a photoelectron spectrum results and hence the name X-ray Photoelectron Spectroscopy (XPS). The kinetic energy of these photoelectrons carries information on the bond energies of the electrons hence characteristic binding energies will give chemical and elemental information of the material. While the incident X-ray photons penetrate deep into the bulk material, photoelectrons that are free of inelastic collisions will originate from the top 1 nm to 10 nm of the material and as such XPS is a surface sensitive technique.

4.7.1 Physics of XPS (Photoionization)

Photoionization is the ejection of one or more electrons from an atom by irradiation of a material with an incident x-ray photon of known energy *hv (h is Planck's constant and v is the frequency of the radiation in Hz)* [Zha09]. In XPS two of the common x-ray sources are [Jai11]:

i. Mg K_α radiation with hv=1253.6 eV and

ii. Al K_α radiation with hv=1486.6 eV

Since the energy of the incident photon (E_p) is known and the kinetic energy (E_k) of the emitted electron can be measured experimentally, the binding energy (E_B) of the electron emitted from a certain electron configuration within the atom can be determined using equation 4.26 [O'Co03]:

$$E_k = E_P - E_B - \Phi_{SP} \qquad 4.26$$

Here, Φ_{SP}, is the work function of the spectrometer which is a combination of the work function of the sample and the work function induced by the analyser. This work function can be compensated for electronically and hence E_B can be found from equation 4.27.

$$E_B = E_p - E_k \qquad 4.27$$

The binding energy is unique for a specific atom and specific orbital hence it will provide the elemental and chemical state of the sample.

The standard set up of an XPS experiment consists mainly of an x-ray source, an electron energy analyser that is able to disperse the emitted photoelectrons according to their kinetic energy and a an ultra high vacuum environment that enables the emitted electrons to be analysed with limited collisions with gas particles. In most set ups, the energy analyser is a concentric hemispherical analyser (CHA). The CHA employs an electric field generated between two hemispherical surfaces to disperse electrons according to their kinetic energy [Jia11].

An XPS spectrum is a plot of the number of electrons that have been detected against the binding energy of the detected electrons. The specific binding energies give rise to characteristic peaks at particular energies indicating the presence of a particular element in

the sample. The intensity of these peaks will therefore an indication of the elements concentration. In this study, A Kratos Analytical fitted with a 5 axis auto stage and a Delay Line Detector (DLD) was used for XPS analysis. These measurements were performed at the EMSL, PNNL, USA. The x-ray source was Al K_α radiation with hv=1486.6 eV and 8 sweeps were performed for each peak for true high resolution studies. The energy scale was calibrated using the binding energy of C 1s at 284.8 eV.

4.8. Raman Spectroscopy

Monochromatic light of frequency ν incident on a molecule induces electronic polarisation in the molecule. The polarizability of a material depends on the molecular structure and the nature of the bonds. The electric field of the incident electromagnetic wave may be written as [Nak97]:

$$E = E_0 \cos(2\pi v_0 t) \qquad 4.26$$

where v_0 is frequency of the incident electromagnetic wave, E_0 is the amplitude of the wave and t is the time.

The induced dipole moment P is given by $P=\alpha E$, where α is the polarizability. Therefore the time-dependant induced dipole moment is then given in equation 4.27 as [Nak97]:

$$P = \alpha E_0 \cos(2\pi v_0 t) \qquad 4.27$$

Perturbation of electron clouds of molecular structures depends on the relative location of the constituent atoms. In molecular bonds, the atoms are confined to specific vibrational modes where the vibrational energy is quantized. The displacement dQ of the atoms about their equilibrium position due to the vibration mode is given by equation 4.28 as [Nak97]:

$$dQ = Q_0 \cos(2\pi v_i t) \qquad 4.28$$

where Q_0 is the amplitude of vibration and v_i is the frequency of vibration. For small displacements the polarizability may be approximated by a Taylor series expansion as [Nak97]:

$$\alpha = \alpha_0 + \frac{\partial \alpha}{\partial Q} Q_0 \cos(2\pi v_i t) \qquad 4.29$$

where α_0 is the polarizability of a molecular mode at equilibrium position. Combining equations 4.27 and 4.29 yeilds [Nak97]:

$$P = \alpha_0 E_0 \cos(2\pi\nu_0 t) + \frac{\partial\alpha}{\partial Q} Q_0 E_0 \cos(2\pi\nu_0 t)\cos(2\pi\nu_i t) \qquad 4.30$$

By applying a trigonometric identity equation 4.30 can be expressed as [Nak97]:

$$P = \alpha_0 E_0 \cos(2\pi\nu_0 t) + \left(\frac{\partial\alpha}{\partial Q}\frac{Q_0 E}{2}\right)\{\cos[2\pi(\nu_0 - \nu_i)t] + \cos[2\pi(\nu_0 + \nu_i)t]\} \qquad 4.31$$

Equation 4.31 shows induced dipole moments are created at three frequencies ν_0, (ν_0-ν_i) and (ν_0+ν_i). Scattered radiation also results at these same frequencies. The first frequency corresponds to the incident frequency and the scattering is elastic (Mie or Rayleigh scattering). The second and the third frequencies are shifted to lower and higher frequencies and are inelastic in nature. The scattered light in these two inelastic modes are the Raman modes named after C.V. Raman who first identified them [Ram28]. The down shifted frequency (longer wavelengths are known as the Stokes scattering modes and the up-shifted frequency (shorter wavelength) are known as the anti-Stokes.

Raman scattering is much weaker than Rayleigh scattering by a factor of 10^{-3} to 10^{-5} [Nak97]. In order to acquire high quality Raman spectra, instruments such as notch filters, tuneable filters, laser stop apertures, double and triple spectrometric systems are used to reduce Rayleigh scattering [Smi05]. In general, a modern Raman instrument consist of an excitation source (laser), sample illumination system and light collection optics, wavelength selector (filter or spectrophotometer) and detector (photodiode array or CCD) [Jia11]. A sample is normally illuminated with a laser beam in the ultraviolet (UV), visible (Vis) or near infrared (NIR) range. Scattered light is collected with a lens and is sent through interference filter or spectrophotometer to obtain a Raman spectrum of a sample.

The Raman shift provides information about changes in the vibrational, rotational and electronic energy of a molecule or crystal. The vibrational energies of molecules differ from material to material due to differences in molecular structures. This means that their Raman spectra will also be different depending on the materials molecular structure. Raman spectroscopy therefore becomes a powerful tool for probing the molecular structure of

materials along with any changes induced in the material, such as changes in a materials structure by radiation damage and its annealing. Depending on the laser power and material under examination, Raman spectroscopy is mainly non destructive. However, damage or annealing of the sample could take place depending on laser power/material/illumination time combination.

In this study the Raman measurements were performed using laser in the visible region and Deep Ultraviolet (DUV) region. Measurements in the visible region were performed with a T64000 Raman spectrometer from HORIBA Scientific, Jobin Yvon Technology (Villeneuve d'Ascq, France). The Raman spectra were excited with the 514.5 nm line of a Coherent Innova® 70C Series Ion Laser System and the 100x objectives of an Olympus microscope was used to focus the laser beam (spot size ~ 2 µm) on the samples and also collected the backscattered Raman signal. An integrated triple spectrometer was used in the double subtractive mode to reject Rayleigh scattering and dispersed the light onto a liquid nitrogen cooled Symphony CCD detector. The spectrometer was calibrated with the silicon phonon mode at 520 cm^{-1}.

For the ultraviolet region, Raman spectra were acquired using a UV-Vis Horiba LabRAM HR Raman spectrometer with an Olympus BX41 microscope attachment. The excitation wavelength was the 244 nm line of a frequency-doubled argon ion laser. The incident beam was focused onto the sample using a 40x UVB objective and the backscattered light was dispersed via a 2400 lines/mm UV grating onto a liquid nitrogen-cooled CCD detector. Data was acquired and processed using LabSpec 5 software.

References

[Bir89] J. Bird and J. Williams, "Ion Beams for Materials Analysis", Academic Press, Australia, 1989, p.620.

[Ber95] A. Bergmaier, G. Dollinger, C. Frey and T. Faestermann, Fresenius J Anal Chem 353 (1995) 582.

[Bin83] G. Binning H. Rohrer, C. Gerber and E. Weibel ,Physical Review Letters, 50 (1983) 120.

[Bin86] G. Binning, C. F. Quate and C. Gerbe, Atomic Force Microscope, Physical Review Letters, 56 (1986) 930.

[Bow09] W. Bowen and N. Hilal, "Atomic Force Microscopy in Process Engineering, Introduction to AFM for Improved Process and Products", Butterworth-Heinemann, Elsevier, Oxford, UK (2009). P.2.

[Cer07] A. Cerezo, P. Clifton, M. Galtrey, C. Humphreys, T. Kelly, D. Larson, S. Perez, E. Marquis, R. Oliver, G. Sha, K. Thompson, M. Zandbergen and R. Alvis, Materials today, 10 (2007) 36.

[Chu78] W. Chu. J. Meyer and M. Nicolet, "Backscattering Spectrometry", Academic Press, New York, 1978.

[Cur80] J. Curie and P. Curie, "Sur l'elecricite polaire dans les cristaux hermiedres a faces inclines, Comptes Rendus", 91 (1880) 386.

[Fel86] L. Feldman and J. Meyer, "Fundermentals of Surface and Thin Film Analysis", Elservier Science Publishing Co, New York, 1986.

[Fri12] E. Friedland, "Stop5", Department of Physics, University of Pretoria, (2012). Private communication.

[Fro89] J. Frosien, E. Plies and K. Anger, J. Vac. Sci. Technol. B 7 (1989) 1874.

[Gau09] B. Gault, M. Moody, F.De Geuser, G.Tsafnat, A.La Fontaine, L. Stephenson, D. Haley and S. Ringer, "Advances in the calibration of atom probe tomographic reconstruction ", Journal of Applied Physics 105 (2009) 034913.

[Gei13] H. Geiger and E. Marsden, Phil. Mag. 25 (1913) 606.

[Gia04] L. Giannuzzi and F. Stevie, "Introduction to Focused Ion Beams, Kluwer Academic Press, New York,NY, USA (2004).

[Gna13] H. Gnaser, R.Schiller, M.Wahl and B.Reuscher, Nucl. Instr and Meth. B 315 (2013) 126.

[Gro84] J. Grob and P.Siffert, Cryst. Growth. 8 (1984) 59.

[Gol03] J. Goldstein, D. Newbury, D. Joy, C. Lyman, P. Echlin, E. Lifshin, L. Sawyer and J. Michael,"Scanning Electron Microscopy and X-Ray Microanalysis", 3rd edition, Springer, USA (2003).

[Gom61] R.Gomer, "Field Emission and Field Ionisation", Harvard University Press, Cambridge, MA, USA,1961.

[Gra31] R. van de Graaff, Phys. Rev. 38 (1931) 1919.

[Jai11] I. Jain and G.Agarwal, Surface Science Reports 66 (2011) 77.

[Kum09] K. Kumagai and T. Sekiguchi, Ultramicroscopy 109 (2009) 368.

[Law87] G. Lawes, "Scanning Electron microscopy and X-ray Microanalysis", John Wiley and Sons, New York, U.S.A (1987).

[Mil00] M. Miller, Materials Characterization 44 (2000) 11.

[Mil01] M. Miller, Micron 32 (2001) 757.

[Mil05] M. Miller, K. Russell and G. Thompson, Ultramicroscopy 102 (2005) 287.

[Mil09] M. Miller, and R. Forbes, Materials Characterization 60 (2009) 461.

[Mil12] M. Miller, T. Kelly, K. Rajan and S. Ringer, Materials Today 15 (2012) 158.

[Msi13] M. Msimanga, D. Wamwangi, C. Comrie, C. Pineda-Vargas, M. Nkosi and T. Hlatshwayo, Nucl. Instr and Meth. B 296 (2013) 54.

[Nag13] M. Nagoshi,T. Aoyama and K. Sato, Ultramicroscopy 124 (2013) 20.

[Nak97] K. Nakamoto, "Infrared and Raman Spectra of Inorganic and Coordination Compounds, Fith Edition" John Wiley & Sons, New York, U.S.A (1997)

[New00] D. Newbury and D. Williams, Acta Materialia, 48 (2000) 323.

[O'Co03] J. O'Connor, B. Sexton and R. Smart, "Surface Analysis Methods in Materials Science"Springer-Verlag Berlin Heidelberg, Germany (2003).

[Por07] S. Portier, S. Bremier and C. Walker, International Journal of Mass Spectrometry 263 (2007) 113.

[Ram28] C. Raman, Indian J. Physics, 2 (1928) 387.

[Ree05] S. Reed, "Electron Microprobe Analysis and Scanning Electron Microscopy in Geology" 2nd edition, Cambridge University Press, Cambridge, United Kungdom, (2005).p.17.

[Rut11] E. Rutherford, Phil. Mag. 21 (1911) 669

[Smi05] E. Smith and G. Dent, "Modern Raman Spectroscopy: a Practical Approach", Wiley,New Jersey, 2005.

[Sou78] H. Southworth and J. Walls, Surface Science 75 (1978) 129.

[Suv07] A. Suvorova and S. Samarin, Surface Science 601 (2007) 4428.

[Tes95] J. Tesmer, M. Nastasi, J. Barbour, C. Maggiore and J. Meyer, "Handbook of modern Ion Beam Materials Analysis", Materials Research Society, Pittsburgh, USA (1995) p85.

[Vau08] D. Vaughan, "Energy dispersive microanalysis, An introduction", Thermo Fisher Scientific (2008).

[Ver04] J. Vermeulen, Imaging and Microscopy 04 (2004).

[Vic89] J. Vickerman, A. Brown and N. Reed, "Secondary Ion Mass Spectrometry, Principles and Applications" Clarendon Press,Oxford University Press, New York, USA, 1989.

[Vic97] J. Vickerman," Surface Analysis-The Princilal Techniques", John Wiley and Sons, Chichester, England, 1997.

[Vur11] F.Vurpillot, M.Gruber, G. Da Costa, I. Martin, L.Renaud, A. Bostel, Ultramicroscopy 111 (2011) 1286.

[Wes95] W. Wesch, A. Heft, E. Wendler, T. Bachmann and E. Glaser, Nucl. Instr and Meth B 96 (1995) 335.

[www1] http://www.tedella.com/apertures-and-fillaments_html/yps-schottky.htm,accessed September 2014

[www2] http://pprco.tripod.com/SIMS/Theory, accessed June 2014.

[Zha09] S. Zhang, L. Li and A. Kumar" Materials characterisation techniques" 1st edition, Taylor & Francis, Florida, USA (2009).p.177.

[Zho06] W. Zhou and Z. Wang, "Scanning Microscopy for Nanotechnology-Techniques and Applications" Springer-Verlag (2006).

[Zie77] J. Ziegler, "Helium Stopping Powers and Ranges in All Elements", Pergamon Press, New York, 1977.

Chapter 5: Sample preparation

5.1 Ion implantation

Single crystalline 6H-SiC wafers 6H-SiC (from *Intrinsic Semiconductors*®) and polycrystalline SiC – made up of predominantly 3C-SiC crystallites - (from *Valley Design Corporation*®) were used as starting substrates in this study. Implantations of several of the radiological significant fission product elements namely cesium, iodine, silver, strontium and xenon were performed for the various instigations in this study as listed below:

Table 5.1: Table listing the ion implantation parameters for the various investigations in this study.

Study	Ion	Implantation temperature	Fluence	Energy
Raman Spectroscopy Studies	$^{127}I^{+}$ $^{109}Ag^{+}$ and $^{88}Sr^{+}$	Room temperature	1×10^{16} cm^{-2} 2×10^{16} cm^{-2}	360 keV
Near-surface recrystallization of the amorphous implanted layer of ion implanted 6H-SiC	1. $^{131}Xe^{+}$, $^{127}I^{+}$ and $^{133}Cs^{+}$ 2. $^{109}Ag^{+}$ and $^{88}Sr^{+}$	Room temperature	1×10^{16} cm^{-2} 2×10^{16} cm^{-2}	360 keV
Diffusion behaviour of cesium in silicon carbide at T > 1000 °C	$^{133}Cs^{+}$	Room temperature, 350 ºC and 600 ºC	1×10^{16} cm^{-2}	360 keV
Synergistic effects of iodine and silver ions co-implanted in 6H-SiC	$^{109}Ag^{+}$ and $^{127}I^{+}$	Room temperature	2×10^{16} cm^{-2}	360 keV

The ion implantations were performed at The Institut für Festköperphysik, Friedrich-Schiller-Universität Jena, Jena, Germany using their 400 kV implanter Romeo. An illustration of the ion beam setup of all the accelerators and beam lines is shown in figure 5.1 below.

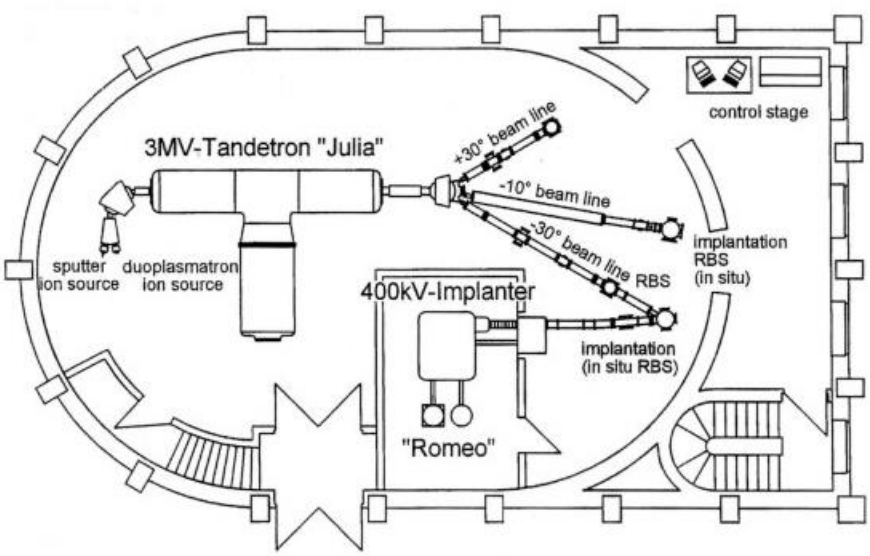

Figure 5.1: Illustration of the Ion Beam Laboratory at the Institute of Solid State Physics, Friedrich-Schiller-Universität Jena, Jena, Germany. Taken from [www1].

During the implantations, the flux was maintained at a rate below 10^{13} cm^{-2} s^{-1} to minimise the effects that may lead to an increase in the substrate temperature, reducing the probability of simultaneously annealing some of the radiation damage produced during the room temperature implantations. During these room temperature implantations however, the temperature of the samples rose to about 55 ºC. The angle of incidence of the ions was set at an angle of 7° relative to the normal to avoid channelling effects during implantation.

5.2 Annealing of samples and the annealing system

After the implantations, the wafers were cut into specimens of dimensions approximately 5.5 mm × 5 mm. These dimensions were chosen on the basis of the maximum allowable size for mounting on sample holders of certain experimental techniques, in particular the RBS sample holders. For the cutting process, a programable Buehler Isomet precision diamond saw was used. This saw makes use of thin metal bonded diamond wafering blades which allow for

more precise cutting, less material loss and reduced induced deformation [www2]. For the single crystalline wafers, the wafers were initially cut into strips of 5.5 mm in the direction parrallel to the primary flat (along the $[11\bar{2}0]$ direction). During the cutting, a coolant was constantly applied to the saw blade tip. The strips were then cut in a perpendicular direction at intervals of about 5 mm producing the desired specimen size of 5.5 mm × 5 mm. Although the sample holders for RBS target mounting limited the specimens to these dimensions size, the area was more than enough as the beam spot of our analysing beam was collimated to 2 mm^2. To clean the samples of any debris and physical contamination, the samples were rinsed in acetone in an ultrasonic shaker followed up by a deionesed water and Extran MA 02 soap solution. The samples were then rinsed in deionised water folluwed up by a final rinse in methanol to remove the excess water.

For the annealing cylces, the final 5.5 mm × 5 mm samples were placed inside small graphite crucibles. The annealing was performed in a computer controlled high temperature vacuum graphite furnace (Webb® 77). To prevent cross contamination, samples implanted with different species were annealed in separate crucibles.

5.2.1 Webb 77 Graphite furnace

Inside the oven, the temperature is controlled by a Eurotherm 2704 controller connected to a thermocouple as well as a pyrometer. The thermocouple is employed for measurements below 1475 ºC and the pyrometer for measurements above 1525 ºC [Web06]. An average value of the thermocouple and pyrometer readings is used in the temperature range in between the 1475 ºC and 1525 ºC set points. Figure 5.2 below is an illustration of a typical heating and cooling curve. The nominal temperature accuracy for the Webb oven is given ±15 ºC.

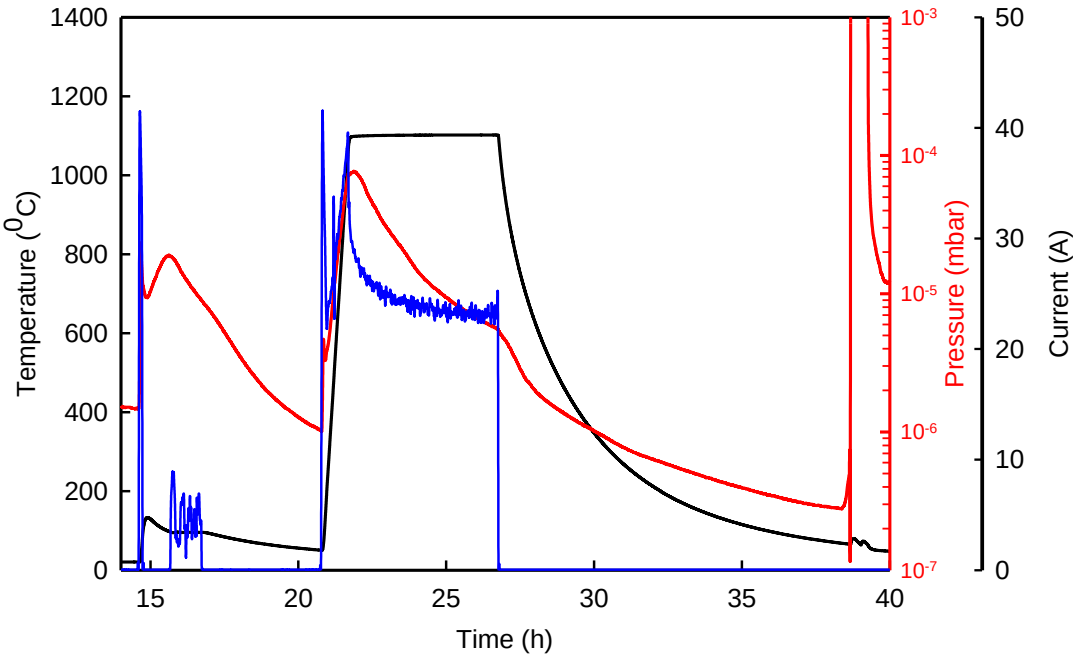

Figure 5.2: Heating and cooling curves for a sample annealed at 1100 ºC for 5 hours. The blue curve represents the current drawn by heating element, the red curve shows the vacuum pressure and the temperature is illustrated by the black curve.

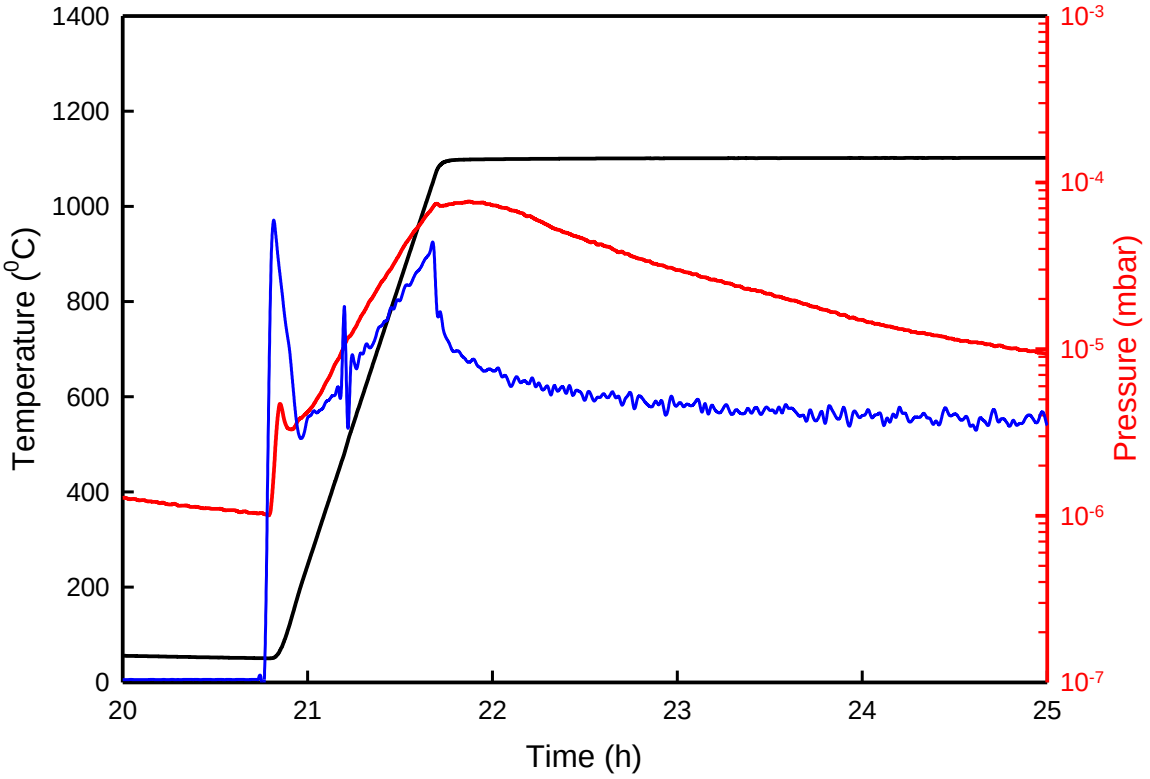

Figure 5.3: Heating curve of the Webb® furnace set to heat up at a rate 20°C per minute. See Figure 5.2 for the meaning of the different coloured curves and also the scale representation of the current curve (blue curve).

Prior to each annealing cycle, the oven was evacuated to a pressure in the 10^{-7} mbar range. This was followed up by a degassing phase where the oven was heated to 100 ºC for one hour to aid the desorption of water vapour and other gases adsorbed on the fibrous carbon internal high temperature insulation. The degassing also helps to ensure that the maximum pressure during annealing will not fall below the 10^{-5} mbar region as most of the adsorbed gases would have been desorbed. For all our experiments, the oven was programmed for a heating rate of 20 ºC/min. On switching on the heating element, a large current of about 40 A is drawn (see figure 5.2 blue peak near around 15 hour mark during initial degassing and at around 21 hours at start of ramping up temperature to set annealing temperature). The current drawn by the element then drops and stabilises to about 24 A as the regulating system kicks in. A noticeable feature just after the element is swithed on and before the regulation of current is

the increase in the chamber vacuum pressure to the order of about 10^{-5} mbar. This is due to the increased degassing due to the high initial current. As the curent regulation stabilises the currrent to about 24 A-see figure 5.2 at around the 22 hour mark, the base pressure is then reduced to the order of 10^{-6} as the puming rate of the turbo pump becomes again larger than the rate of degassing. In this particular cycle, the oven was set to dwell at a temperature of 1100 ºC for 5 hours (from 22 hour mark to 27 hour mark in figure 5.2). At the end of the 5 hours, the current is automatically switched off and the oven allowed to cool off naturally (27 hour mark to 40 hour mark in figure 5.2). From Newton's cooling law, the Webb oven cooling is approximately given by:

$$T(t) = F\exp(-Zt) \qquad 5.1$$

The cooling rate is then the time derivative of the decrease in temperature given by:

$$\frac{dT}{dt} = -FZ\exp(-Zt) \qquad 5.2$$

where F and Z are constants, T is the temperature and t the time. For our Webb system, F and Z have been determined by fitting data of the cooling curve and this information can be found in work of Hlatshwayo [Hla10].

References

[www1] http://www.physik2.uni-jena.de/inst/exphys/ionen/accessed July 2014.

[www2] http://www.buehler.com, accessed July 2014

[Web06] R.D. Webb Company, operating manual Webb 77. 2006.

[Hla10] T.T. Hlatshwayo, "Diffusion of silver in 6H-SiC" PhD Thesis, Department of Physics, University of Pretoria, South Africa, 2010, p62.

Chapter 6 Results- Diffusion Studies

6.1 Introduction

Our group has been performing in depth studies on the diffusion of the radiological significant fission product elements in SiC over the past 8 years. These include isochronal and isothermal annealing studies on the diffusion of iodine [Fri10], silver [Fri09,Hla12a,Hla12b], strontium [Fri12] and xenon [Fri14]. In this thesis we continue this effort by extending the diffusion studies to cesium implanted SiC. Isochronal and isothermal annealing studies of single crystalline and polycrystalline SiC samples implanted with cesium ions have been performed and are presented in sections 6.1.1 and 6.12.

6.1.1 Isochronal annealing results of cesium implanted single and polycrystalline SiC

Figure 6.1(a) shows the 360 keV Cs^+ as-implanted RBS-channelling spectra of the 6H-SiC samples implanted at room temperature, 350 ºC and at 600 ºC. The surface region of the cold implant is up to a depth of about 190 nm totally amorphous. This amorphous region only partly re-grows epitaxially from the bulk during annealing as illustrated in figure 6.1(b), while the remainder re-crystallizes into a finely grained polycrystalline phase. The implant at 350 ^oC exhibits a highly disordered buried layer from 25 to 180 nm below the surface, which, however, is not yet fully amorphous, as the crystal lattice is restored after annealing. Therefore this temperature is just below the critical temperature for amorphization for cesium ions. The reported critical temperatures for other ion species are lower than that for cesium. At an implantation temperature of 600 ^oC, the crystal structure is retained, albeit with a high degree of distortions.

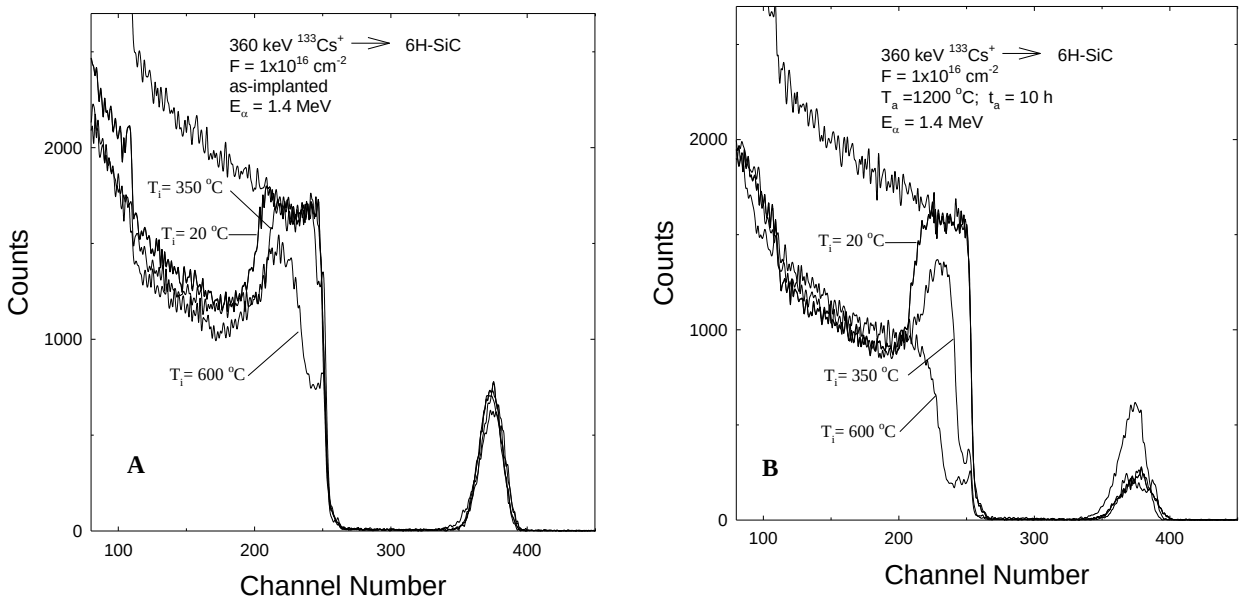

Figure 6.1: RBS-channelling spectra of cold and hot implants before (A) and after 10 hours annealing at 1200 °C (B).

The cesium depth distributions at room temperature and at 600 °C are depicted in figure 6.2 together with those of strontium [Fri12] and iodine [Fri11] for comparison. The first four moments obtained by fitting the profiles to an Edgeworth distribution as described in section 2.3 of chapter 2 are as follows: Room temperature implantation (R_P= 106 nm, σ=29 nm, β=2.8 and γ=0.2) and 600 ºC implantation(R_P=108 nm, σ=40 nm, β= 2.8 and γ=0.6). The broadening of the cesium profile at the higher implantation temperature of nearly 40% reveals an abnormally strong temperature dependence of irradiation induced diffusion. Less than 15% broadening was previously observed for two other ion species iodine and strontium and less than 5% difference for silver [Hla12b]. Since iodine is almost as heavy as cesium, this dependence seems not to be directly related to the ion mass. Also shown are TRIM-98 simulations, which agree reasonably well as far as the projected ranges are concerned, but predict much smaller σ-values. This is not surprising considering the many approximations made in this code, especially the neglect of thermal effects.

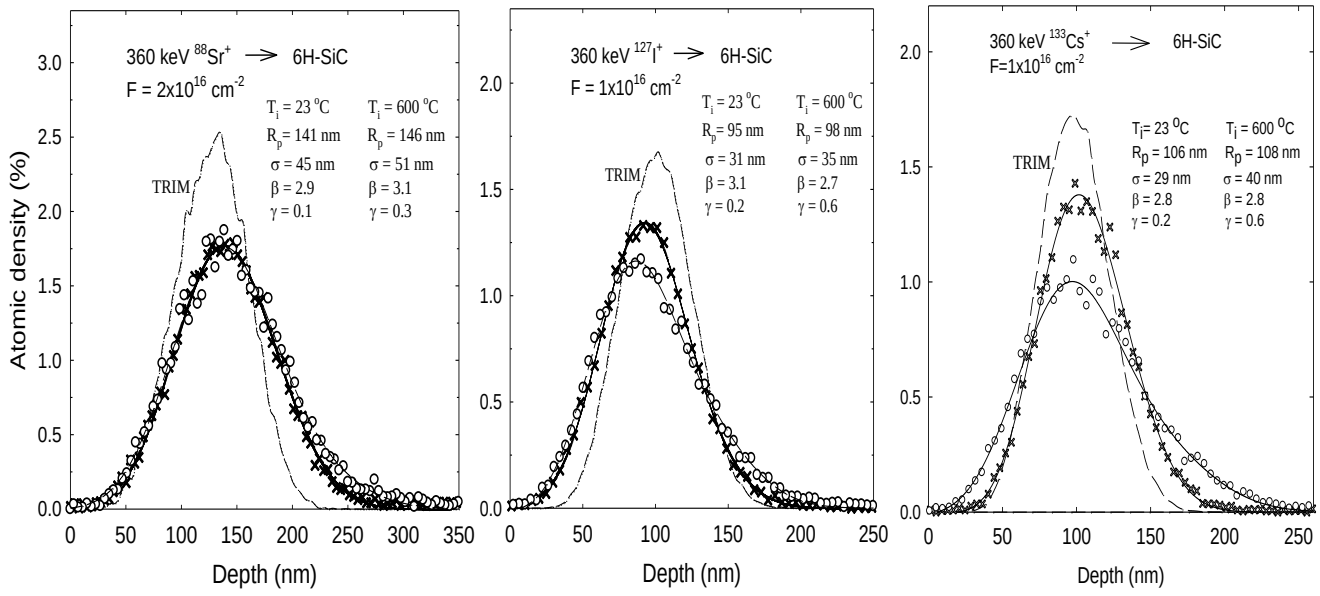

(a) (b) (c)

Figure 6.2: Depth profiles of strontium [Fri12] (a), and iodine [Fri11] (b) implanted at room temperature (X) and 600 °C (O) compared with those of cesium (c). The four distribution moments for the cold and hot implantations are given in each figure. Also shown are TRIM-98 simulations [Zie85].

Figure 6.3 shows the isochronal annealing curves for the 6H-SiC and poly crystalline wafers implanted with cesium. In both samples the widths of the room temperature implants increase during the first annealing cycle due to diffusion in the initially amorphous surface regions. This does not occur in the samples implanted at 600 ^{o}C, where the basic crystal structure is retained. In the case of the 350 ^{o}C implants an increase of the width of the ion distribution is clearly observed in 6H-SiC, while this is not so obvious in CVD-SiC. Although the experimental errors are too large for a definite statement, it appears from figures 6.3a and 6.3b that the as-implanted width of the 350 °C implantation is similar to that at room temperature in 6H-SiC, while it is more like the 600 °C implantation in CVD-SiC. Further width broadening occurs in all samples only at temperatures above 1200 ^{o}C. Within experimental errors, very little difference is observed for the six samples, although a slight tendency of less diffusion at higher implantation temperatures might be concluded from the 6H-SiC measurements. This is in sharp contrast with diffusion results from xenon implanted 6H-SiC [Fri14] where the annealing behaviour of the cold and hot implanted samples showed marked differences. This was attributed to the large differences in the crystal structures after

annealing of the cold and hot xenon implanted samples. Radiation damage in the hot implants was gradually reduced with annealing while SEM showed that after annealing the samples implanted at room temperature the near surface structure became polycrystalline resulting in a drastically modified surface topology composed of large crystals after annealing at 1300 ºC for 5 hours. The differences in the evolution of the surface topography of the cold implants with annealing and its role in the diffusion of several types of implanted fission product elements has been explored by SEM and AFM studies and will be presented in section 7.1 of chapter 7.

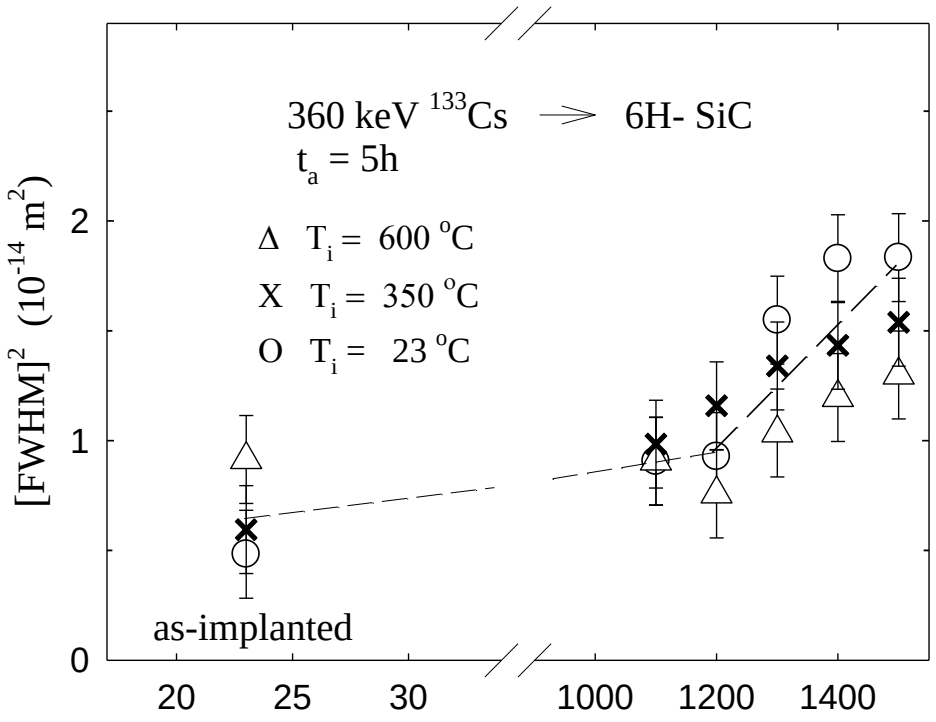

(a)

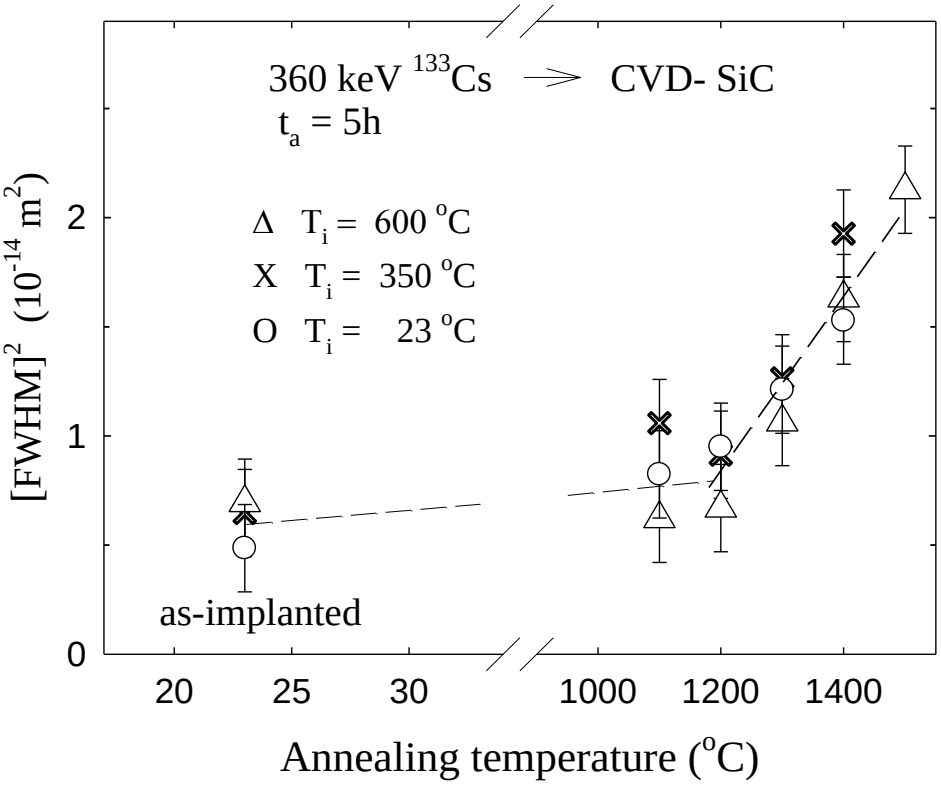

(b)

Figure 6.3: Isochronal annealing curves for 6H-SiC (a) and CVD-SiC (b) at room temperature (O), 350 °C (X) and 600 °C (Δ).

The retained cesium during isochronal annealing is depicted in figure 6.4. No loss occurs in both samples implanted at 600 °C, while approximately 50% is lost during the first annealing cycle in the samples implanted at room temperature. Obviously cesium diffuses relatively fast through the amorphous region towards the surface, where it evaporates into the vacuum. No further diffusion occurs after this first cycle up to 1400 °C, as the amorphous region recrystallizes simultaneously.

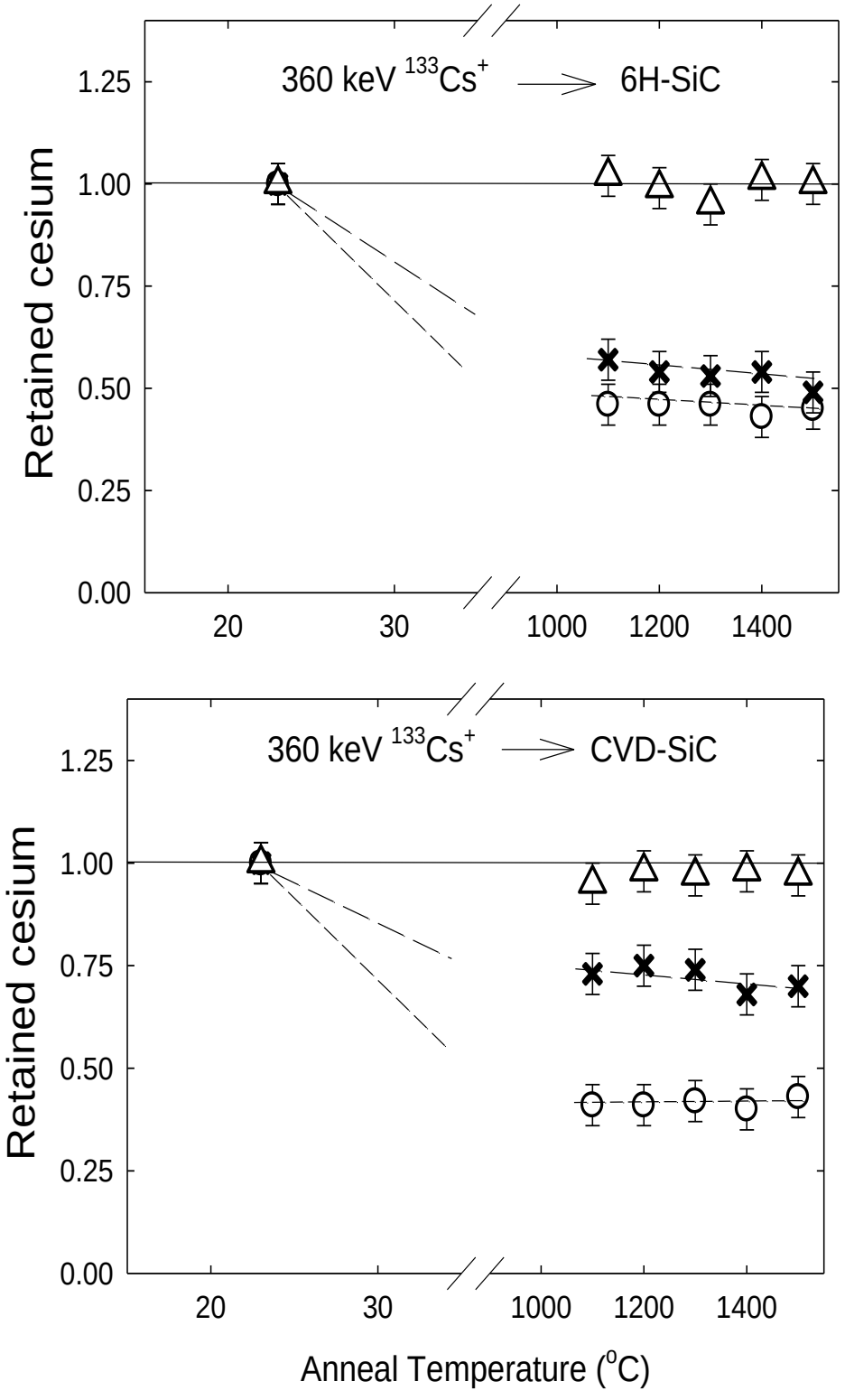

Figure 6. 4: Retained cesium after 5 hours isochronal annealing of 6H-SiC and CVD-SiC implanted at room temperature (O), 350 °C (X) and 600 °C (Δ).

A different behavior is again observed for the 350 ^{o}C samples. The cesium loss in the single crystalline sample is similar to the room temperature implant, while only about 25% is lost from the poly crystalline sample. This, together with the results presented in figure 6.3 seems to indicate, that the degree of amorphization is less in the latter sample. However, whether this is due to the poly crystalline character cannot be decided with certainty from the results. From figure 6.1 it seems that the characteristic temperature for amorphization is near 350 ^{o}C for Cs implantation, which is higher than expected from a semi-empirical model [Web00,Web08] but would be in accordance with values obtained for Ga and Sb ions implanted at similar energies [Wes95,Hef96]. At this temperature the ion flux, which has not been closely monitored during implantation, can have a decisive influence on the degree of amorphization.

This cesium loss behaviour is also in sharp contrast with the observed diffusion behaviour of xenon implanted samples [Fri14]. In the case of xenon, no loss of xenon was observed for from the first annealing cycle through to the 1200 ºC annealing cycle for both the cold and hot implants of both 6H-SiC and polycrystalline samples. Significant loss of xenon was only observed after annealing at temperatures above 1300 ºC. However this was attributed to surface erosion due to thermal etching at these temperatures as observed via SEM and AFM [Fri14]. Similarly no loss of iodine was observed during the first annealing cycles with broadening of iodine profile only above 1100 ºC [Fri10]. Approximately 4 % of implanted silver (cold implants) was lost after the first annealing cycle at 1100 ºC with about 47% loss after the 1400 ºC annealing cycle for 6H-SiC samples [Hla12b]. The loss of cesium during the first annealing cycle however, is similar to the behaviour of strontium where strong diffusion is observed for room temperature implanted 6H-SiC after the first annealing cycle at 1000 ºC [Fri12].

6.1.2 Isothermal annealing results of cesium implanted single and polycrystalline SiC

Figure 6.5 depicts isothermal annealing curves of the 6H-SiC wafers at 1200 ^{o}C, 1300 ^{o}C and 1400 ^{o}C. Similar curves are obtained with the CVD-SiC samples (not shown). The cold implants show the expected strong initial diffusion before re-crystallization, but no further diffusion during subsequent annealing cycles. No diffusion at all is observed in the hot implants. Diffusion coefficients are obviously in all cases below our detection limit of 10^{-21} m^2 s^{-1}. This observation, which seems to be inconsistent with the relatively strong diffusion

above 1200 ^{o}C during isochronal annealing (see figure 6.3), points to a trapping mechanism of impurities by defect structures. Diffusion processes are only taking place during periods of defect annealing and stop as soon as defect restructuring is coming to an end. Cesium atoms bound to defect complexes are released during their annihilation or restructuring, but are again captured after some time by more stable defects. During isochronal annealing that can happen after each cycle at a higher temperature, while during isothermal annealing it occurs only during the first cycle. A similar situation was also observed for the diffusion behaviour of strontium [Fri12].

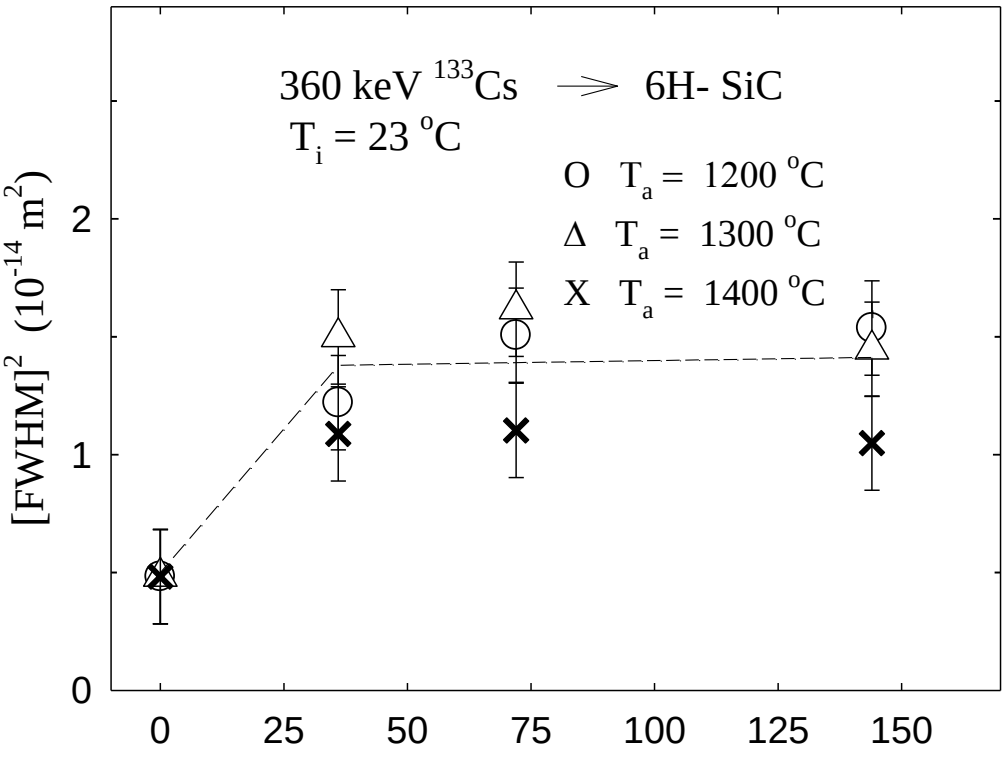

(a)

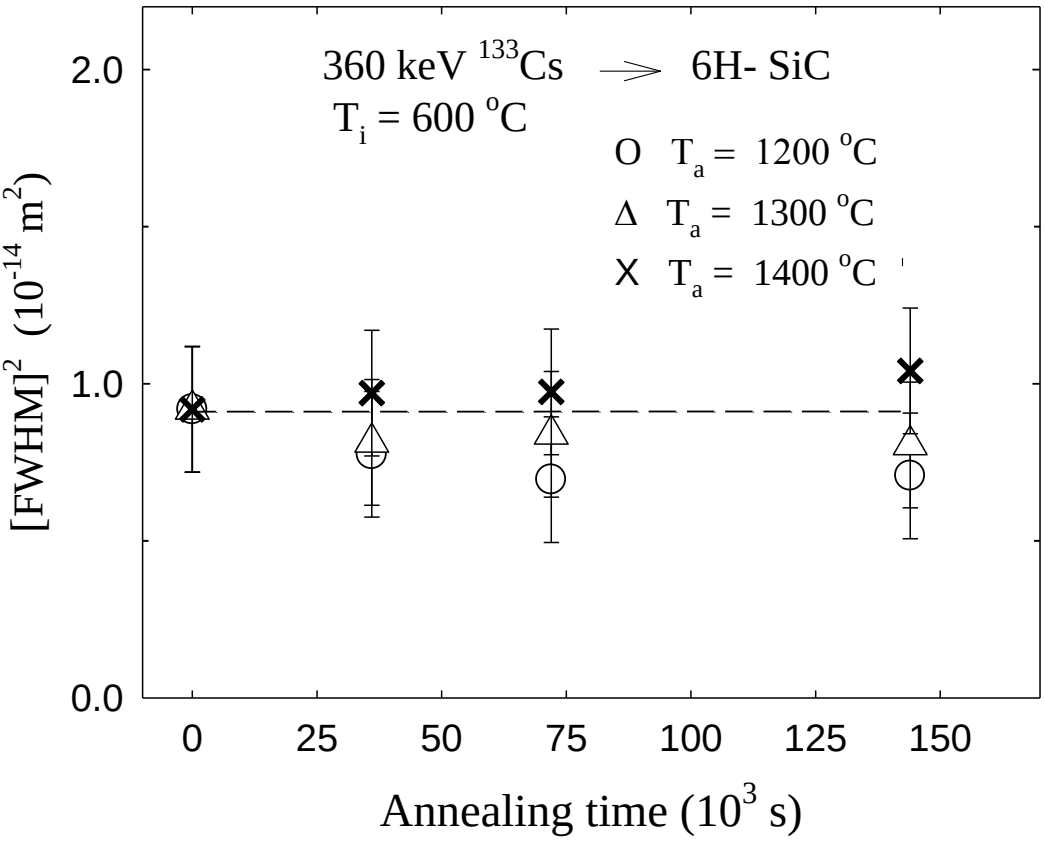

(b)

Figure 6.5: Isothermal annealing curves of cold (a) and hot implanted 6H-SiC at 1200 °C, 1300 °C and 1400 °C (b).

The retention of cesium during isothermal annealing displayed in figure 6.6 is the same as observed during isochronal annealing. No cesium loss from the hot implants and about 50% loss from the room temperature ones are found, while the samples implanted at 350 °C again report different losses of 50% and 25% from the 6H-SiC and CVD-SiC wafers respectively.

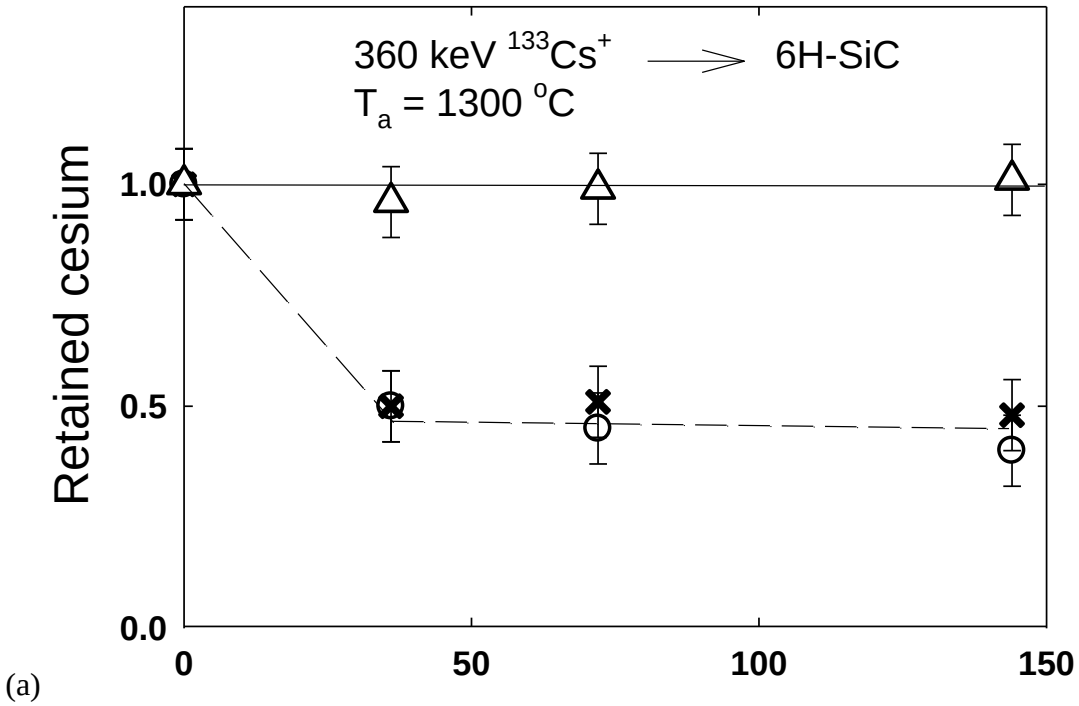

(a)

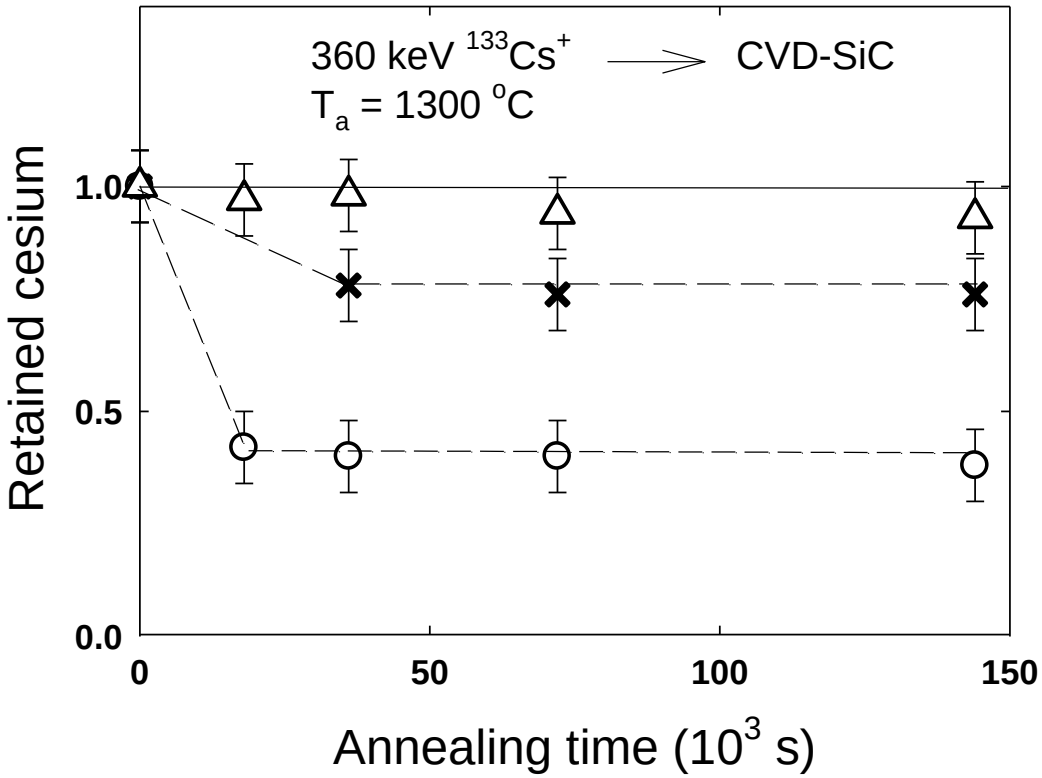

(b)

Figure 6.6: Retained cesium in 6H-SiC and CVD-SiC implanted at room temperature (O), 350 °C (X) (a) and 600 °C (Δ) after isothermal annealing at 1300 °C (b).

6.2 Results of the high temperature isochronal annealing studies of iodine and silver ions implanted in to 6H-SiC: Synergistic effects on the diffusion behaviour in SiC

Recent studies on the diffusion behaviour of Ag implanted 6H-SiC and I implanted 6H-SiC (room temperature implantations) [Hla10,Kuh10] have shown contrasting trends. Appreciable loss of the implanted silver was observed after long time annealing while very little iodine loss was observed after similar annealing cycles. Another study [Dwa14], involving the use of a multilayer diffusion couple also reveals the contrasting diffusion behaviour of I and Ag. The diffusion couple composed of CVD β-SiC, highly anisotropic pyrolythic carbon and a SiC capping layer of Plasma Enhanced CVD (PECVD) SiC was designed to closely simulate behaviour in the TRISO particle. In their study, samples were each separately implanted with europium, cesium, strontium, silver and iodine ions. After annealing at 1100 °C for 10 hours, the PECVD SIC barrier was able to retain all the fission products within diffusion couple except for the silver.

To shed more light on this diffusion behaviour, a new study in this thesis used high temperature, long time isochronal annealing cycles of 360 keV Ag implanted and 360 keV I implanted 6H-SiC samples along with 6H-SiC samples co-implanted with 360 keV ions of both I and Ag in the same wafer. The implantations were done with the substrate at room temperature. The samples were vacuum annealed at 1500 °C for 30h. Several techniques including RBS-C, ERDA, SIMS and APT were used in the investigations and the results are presented in the following section, section 6.2.1 to section 6.2.4

6.2.1 RBS-C results

Figure 6.7 shows the RBS spectra of the as-implanted and annealed samples of Ag (360 keV ions) implanted into 6H-SiC. The measurements show that within the detection limits of RBS, all of the implanted Ag was lost after annealing at 1500 ºC for 30 hours. The carbon surface peak of the RBS spectra near channel number 130 was significantly higher for the annealed sample than for the as-implanted sample. This result shows a build up of a carbon layer on the surface after annealing. The accumulation of a surface carbon layer is due to the decomposition of SiC at this temperature [Ber12]. At this temperature Si evaporates leaving C on the surface. Decomposition of the SiC surface at temperatures of 1500 °C and above has also been reported for Ag ion implantation into SiC at 350 ºC and 600 ºC [Hla12a].

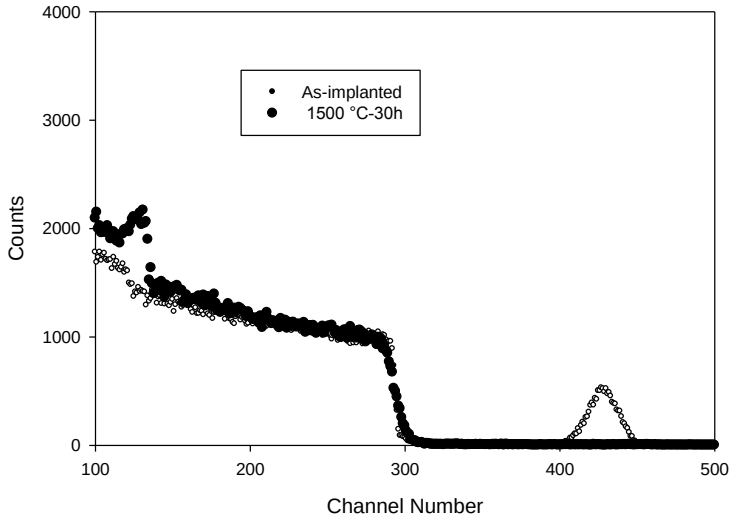

Figure 6.7: The random spectrum of as-implanted SiC sample implanted with 360 keV silver ions to a fluence of 1×10^{16} cm^{-2} compared to the post-annealed spectrum of the same sample annealed at 1500 °C for 30h. The ion implantation was performed at room temperature.

The RBS spectra of the as-implanted and annealed samples of 360 keV I ions implanted into 6H-SiC is shown in figure 6.8. In contrast to the Ag implanted sample, annealing of the I implanted sample shows that most of the I is still present in the sample after the same annealing conditions of 1500 ºC for 30 hours. In this case, the iodine profile has broadened significantly after the annealing showing that diffusion has taken place during annealing. The complete loss of Ag in the previous sample indicates that Ag diffuses faster than I in the initially amorphous SiC (later polycrystalline SiC) at this temperature. A comparison of the signals from the surface carbon edges shows that while there is some modest surface carbon enrichment for the I implanted sample (channel 130), the carbon layer is far more pronounced for the surface of the Ag implanted samples.

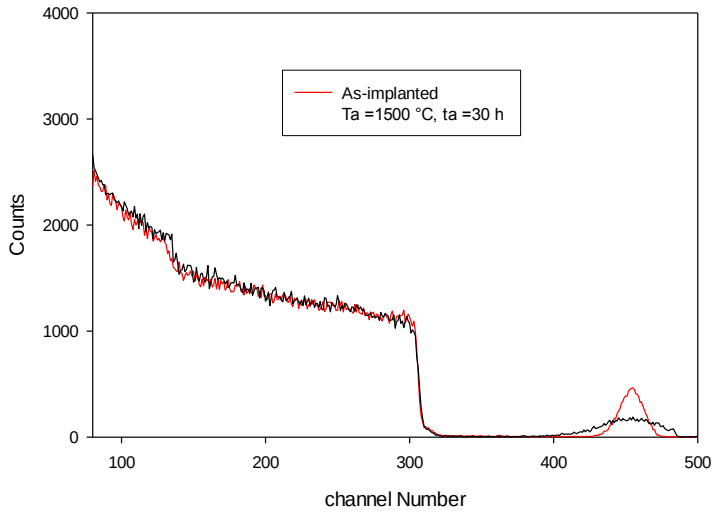

Figure 6.8: The random spectrum of the as-implanted SiC sample implanted with 360 keV iodine ions to a fluence of 1×10^{16} cm^{-2} compared to the post-annealed spectrum of the same sample annealed at 1500 °C for 30h. The ion implantation was performed at room temperature.

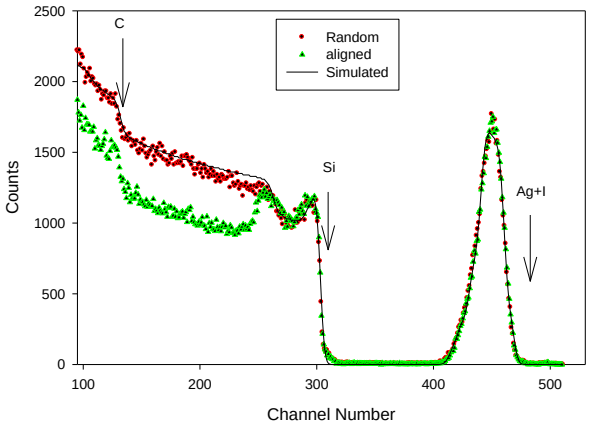

Figure 6.9: Aligned and random RBS spectra of the 360 keV silver and 360 keV iodine (each to a fluence of 1×10^{16} cm^{-2}) co-implanted into SiC at room temperature as compared with SIMNRA simulation. The surface positions are indicated by the arrows. The implantations were performed at room temperature.

Figure 6.9 shows the RBS and RBS-C spectra of the as-implanted sample along with a theoretical simulation using the SIMNRA code [May97]. The arrows on the plot indicate the surface positions of the elements. The co-implantation of the Ag and I ions at room temperature resulted in the creation of an amorphous surface layer up to a depth of 290 nm from the sample surface. This can be seen from the aligned spectrum overlapping with the random spectrum from the Si surface edge. The combined Ag and I impurity concentration in the SiC matrix results in a dip, observable just beyond the Si surface edge. The Gaussian peak from channel 400 to channel 500 is from the signal coming from the implanted ions. The similarity of the masses of Ag and I results in RBS being unable to resolve and separate the signals from the 2 species. Calculations performed by the Stopping and Range of Ions in Matter (SRIM) code predict that the projected ranges for I and Ag are 97.1 nm and 107.3 nm respectively [www1].

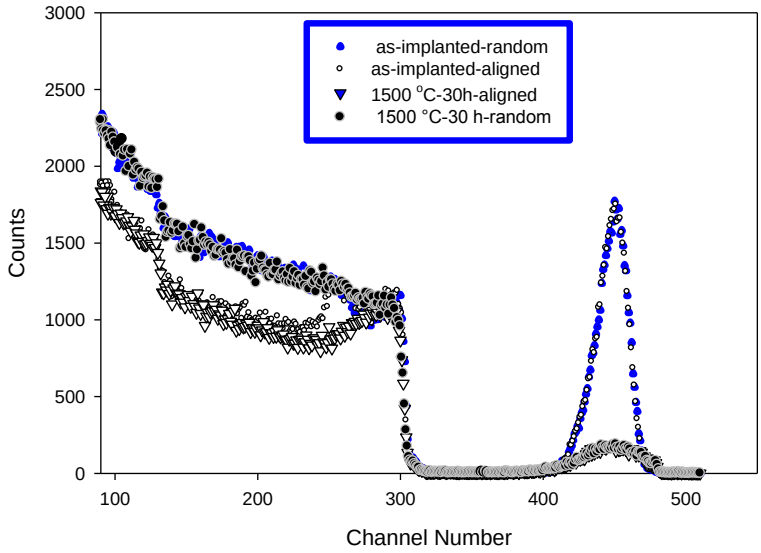

Figure 6.10: Aligned and random RBS spectra of silver and iodine co-implanted into SiC at room temperature compared with the aligned and random spectra of the sample annealed at 1500°C.

The RBS random and aligned spectra of the co-implanted sample compared with the random and aligned spectra after annealing at 1500 ºC for 30 hours are shown in figure 6.10. The aligned spectra of the annealed sample appears to show that some recrystallization of the

amorphous layer had taken place epitaxially starting from the bulk-damaged interface layer. However, this thinning of the damaged near surface region could be partly due to surface erosion due to thermal etching of SiC at these temperatures. Comparing the profiles of the implanted species before and after annealing, it is clear that a significant amount of the implanted material is lost via diffusion through the front surface.

6.2.2. Heavy ion ERDA results of silver and iodine ions co-implanted in to 6H-SiC

Due to the similarities in the masses of Ag and I, RBS is not able to resolve the contributions from Ag and I in the implantation profiles. However, heavy ion ERDA performed using a 26 MeV Cu^{7+} ion beam allows us to separate and clearly resolve the contributions of the respective implanted ions. ERDA profiles showing the variation of the atomic concentration with depth of both the as-implanted and the annealed samples of the co-implanted samples are presented in figure 6.11 and figure 6.12 respectively. The ERDA profiles of the as-implanted sample in figure 6.11 show the Ag profile sitting slightly deeper than the I profile. This is expected considering Ag's lower mass resulting in a deeper projected range for Ag ions (cf. the projected range values given above). The overlapping signals from the atomic concentrations of Si and C are also to be expected from the equal amounts of Si and C in SiC.

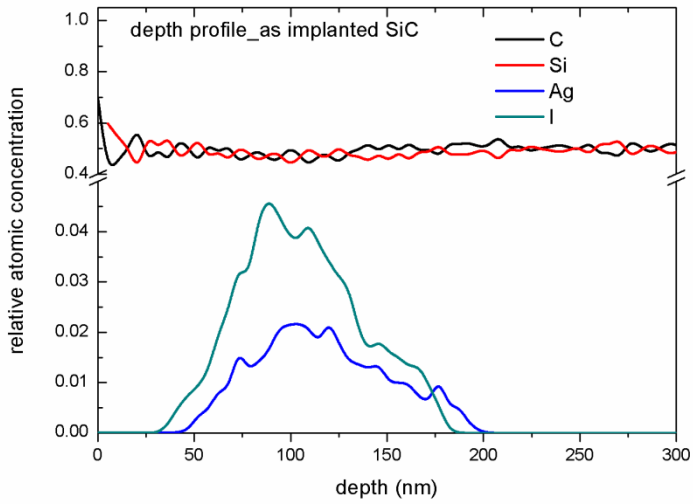

Figure 6.11: Heavy Ion ERDA results of I and Ag co-implanted at room temperature.

The ERDA profiles of the co-implanted sample after annealing at 1500 ºC for 30 hours are shown in Figure 6.12. Both the Ag and I concentration profiles have been reduced due to loss of the implants via the front surface. Diffusion of both I and Ag has also taken place towards the bulk as the back end of the profiles now extend beyond 200 nm and to 250 nm for I and Ag respectively. The strain introduced by the double implantation could cause the damage that normally extends beyond the implanted region to be higher than in the case of the single element implantation. This damage could provide pathways for the ions in the co-implanted sample to move towards the bulk in this case. The presence of Ag after the 1500 ºC annealing cycle in the co-implanted sample is a significant result. No Ag had been detected in the Ag implanted sample in the absence of I by RBS results (see figure 6.7). This is probably due to the formation of AgI, a relatively stable silver halide used in photographic paper. This possibility will be discussed further in sections 6.2.4 and 7.2.

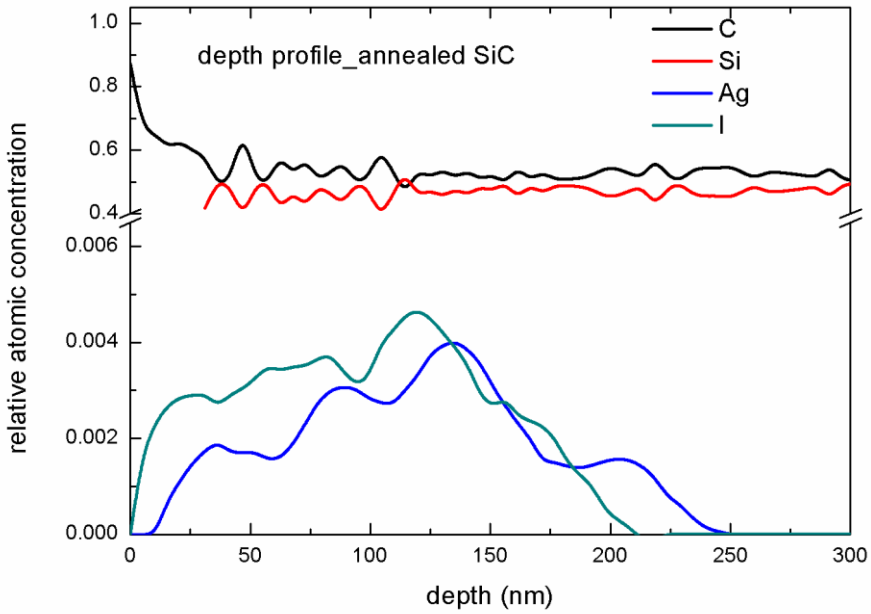

Figure 6.12: Heavy Ion ERDA results of I and Ag co-implanted at room temperature and annealed at 1500 °C for 30 h.

From figures 6.11 and 6.12, it is clear that approximately 90 % of I and Ag have been lost. The loss of iodine in the co-implanted sample is greater than in the iodine only samples (see figure 6.8). The stronger iodine loss in the co-implanted sample also points to the surface

erosion alluded to in section 6.2.1. As iodine sits closer to the front surface than Ag (figure 6.12), the higher loss of iodine here than in the iodine only implanted samples can be attributed to the surface erosion. Raman spectroscopy studies were also performed to ascertain the level of surface decomposition for both single and co-implanted samples. These results are discussed in section 7.3.

6.2.3 SIMS Results of silver and iodine ions co-implanted in to 6H-SiC

To complement the RBC and ERDA analysis, SIMS measurements were performed on the samples co-implanted with Ag and I. SIMS depth profiling of the samples is shown in figure 6.13

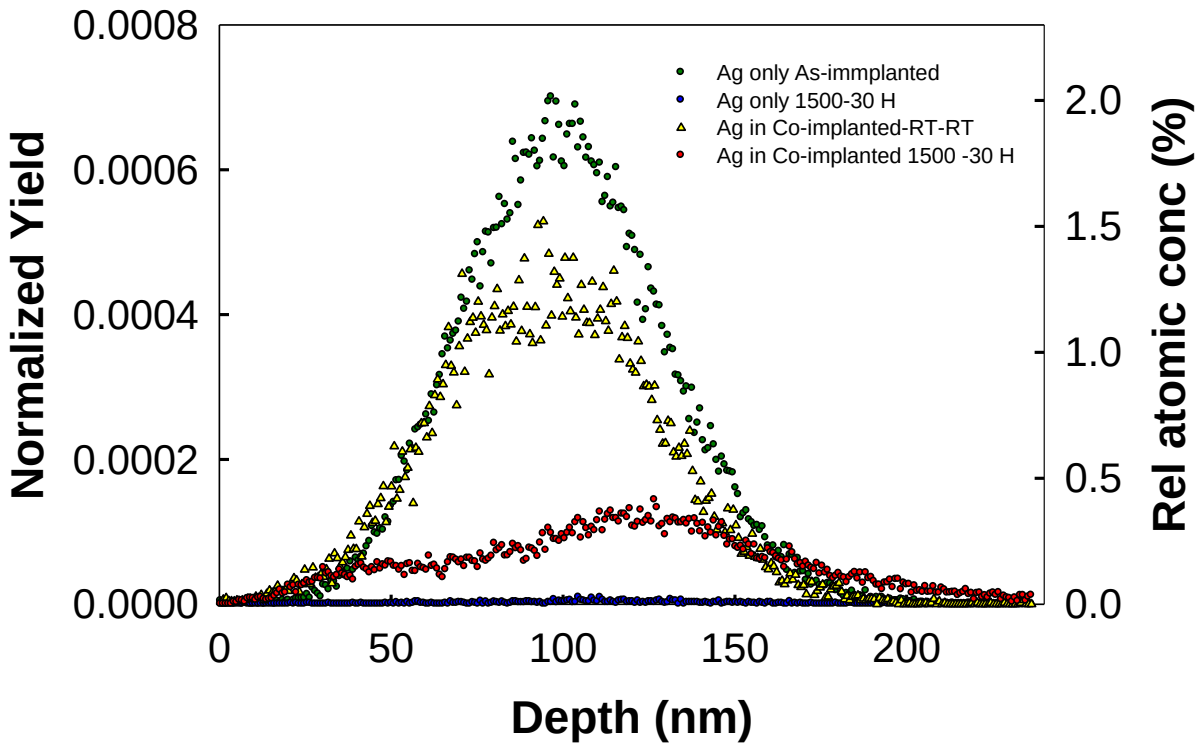

Figure 6.13: SIMS yield profiles from Ag ions in SiC normalized to Carbon 12. The profiles from SIMS measurements of the single element Ag implantation are: the as-implanted sample (green curve), the as-implanted of the co-implanted sample (yellow curve), the co-implanted sample annealed at 1500 ºC for 30 hours (red curve) and the single element Ag implanted sample also annealed at 1500 ºC for 30 hours (blue curve).

In figure 6.13, four signals, two from the Ag signal in the single element implantation (as-implanted and annealed) and two from the Ag signal in the co-implanted sample (as implanted and annealed) are plotted together for comparison. The as-implanted profile (green curve) shows the initial peak concentration of Ag in SiC as calculated was approximately 2%. After annealing at 1500 ºC for 30 hours (blue curve), virtually all of the implanted Ag has been lost through the front surface. This result is consistent with our RBS results presented in figure 6.7. However, when I ions are co-implanted with Ag ions and annealed again at 1500 ºC for 30 hours, SIMS Ag distribution profile shows that some Ag has been retained (red curve). For the co-implanted sample the peak concentration of the implanted Ag fell from a peak concentration of about 1.5% (yellow curve) to approximately 0.4 % (red curve). This is consistent with our heavy ion ERDA results presented in figure 6.12. This result demonstrates that the presence of I has a synergistic effect on the diffusion-inhibition and retainment of Ag in SiC. As discussed in section 7.1, iodine's role in enhancing recystallisation [Kuh14] could play an important role in the immobilisation of Ag. The iodine assisted retention of silver could also point to the formation of silver and iodine defect complexes. This possibility will be discussed in the following section on atom probe tomography studies (Section 6.2.4).

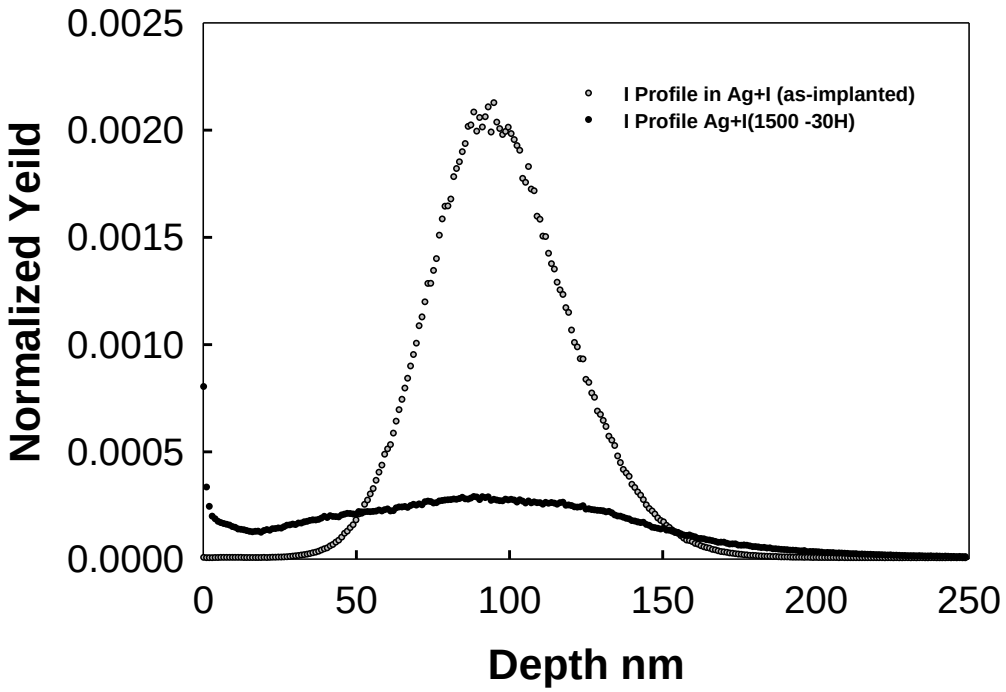

Figure 6.14: I distribution profiles from SIMS measurements of the as-implanted of the co-implanted sample (grey curve) and from the co-implanted sample annealed at 1500 ºC for 30 hours (black curve).

Shown in figure 6.14 are the corresponding SIMS profiles of I from SIMS measurements of the as-implanted spectrum of the co-implanted sample (grey curve) and from the co-implanted sample annealed at 1500 ºC for 30 hours (black curve). The presence of iodine after annealing agrees with our ERDA results shown in figure 6.12.

6.2.4 APT Results of silver and iodine ions co-implanted in to 6H-SiC

Atom Probe Tomography (APT) was utilized to get a clearer picture of the Ag and I diffusion behaviour at atomic level. Figure 6.15a shows an SEM image of the APT needle specimen of the Ag and I co-implanted and annealed sample. APT analysis resulted in 7.8 million ion data capturing information up to 80nm depth from the top surface of the needle specimen. The entire APT reconstruction is shown in figure 6.15 (b)) where Si (grey), C (brown) are

predominantly visible. Ag only (blue) and I only (red) ion distributions are shown in figure 6.15(c) and (d) respectively from which multiple regions of clustering of Ag and I can be observed.

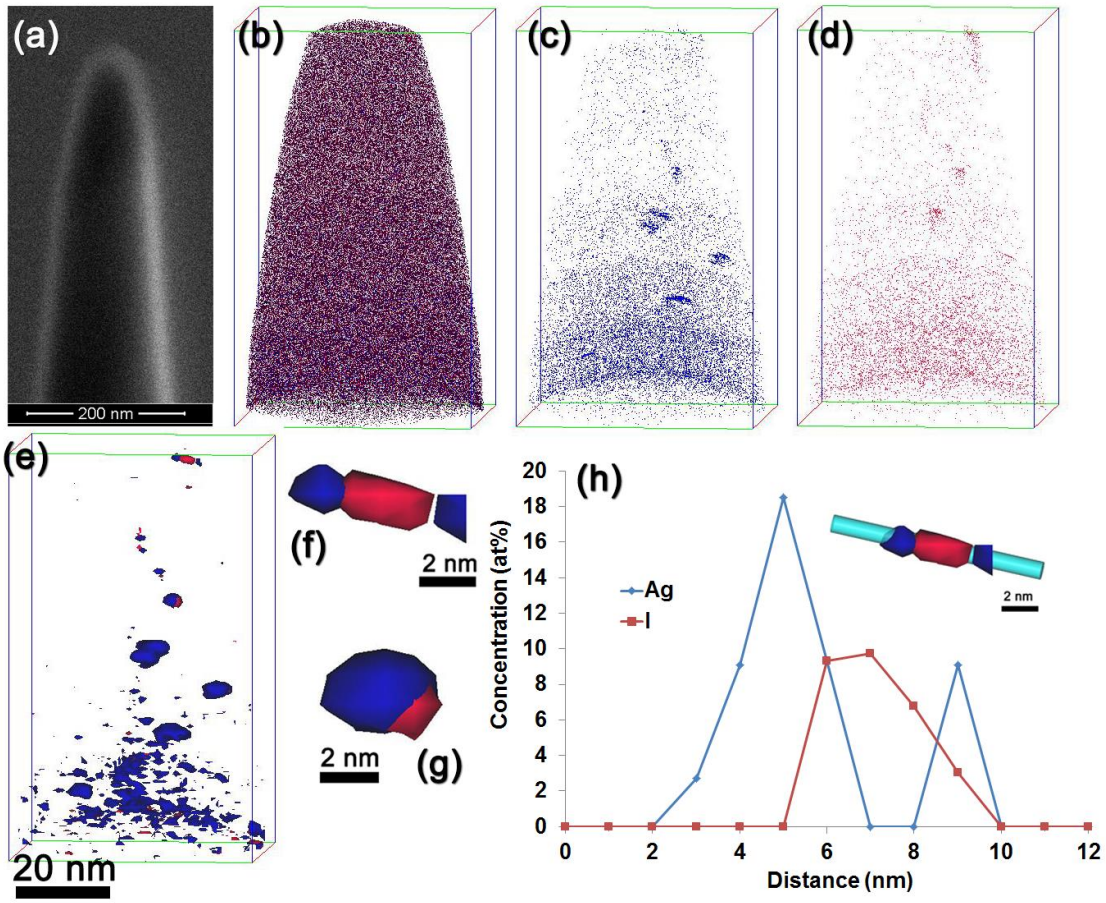

Figure 6.15: APT results from Ag and I co-implanted sample (a) SEM image of the final needle specimen (b) all ion map of the reconstruction showing Si (grey), C(brown), Ag (blue) and I(red) ion. (c)Only Ag ion distribution showing regions of clusters of Ag (d) Only I distribution showing regions of I clusters at similar locations of Ag clusters (e) 3 at% Ag and 3 at% I isocomposition surface showing the overall distribution of Ag and I clusters in the reconstruction (f, g) magnified views of two clusters showing the spatial correlation of Ag and I clusters (h) 1D composition profile across the clusters shown in (f) highlighting Ag enrichment on either sides of an I enriched cluster.

These ion maps shows a higher concentration of both Ag and I towards the 80 nm region, consistent with the composition profile of the implants seen via RBS (figure 6.10), SIMS (figures 6.13 and 6.14) and Heavy ion ERDA (figure 6.12). This is to be expected as the ion distribution peaks at the projected ranges of the ions which, predicted by SRIM [www1], are

approximately 97.1 nm and 107.3 nm for I and Ag, respectively. A cluster of I ions is visible within the first 10 nm from the top surface of reconstruction, consistent with near surface peaks observed from RBS and SIMS measurements (figures 6.8 and 6.14). To further delineate the Ag and I clusters, isocomposition surfaces were plotted at 3 at% Ag (blue) and 3 at% I (red) as shown in figure 6.15(e). From the isocomposition surfaces shown in figure 6.15 (e), a clear spatial association of Ag and I clusters can be noted. Examples of two such clusters with clear spatial association between Ag and I enriched regions are shown magnified in figures 6.15(f) and (g). Subsequently, to quantify the compositional changes going across the cluster shown in figure 6.15(f), a 1D concentration profile was plotted using a 1nm diameter cylinder (shown as inset in fig 6.15(g)). The composition profile given in figure 6.15(h) clearly highlights the presence of an I enriched region in the middle of two Ag enriched regions. This spatial association of Ag and I enriched regions are particularly interesting considering past reports of ions of individually implanted Ag and I into SiC have been known to form nano-clusters after high temperature annealing cycles [Hla12b,Mal13].

References

[Ber12] N.G. van der Berg, J.B. Malherbe, A.J. Botha and E Friedland, Appl. Surf. Sci. 258 (2012) 5561.

[Dwa14] S. Dwaraknath, G.S. Was, J. Nucl. Mater, 444 (2014) 170.

[Fri09] E. Friedland, J. Malherbe, N. van der Berg, T. Hlatshwayo, A. Botha, E. Wendler and W. Wesch, J. Nucl. Mater. 389 (2009) 326.

[Fri10] E. Friedland, N.G. van der Berg, J.B. Malherbe, R.J. Kuhudzai, A.J. Botha, E. Wendler and W. Wesch, Nucl. Instr and Meth. B 268 (2010) 2892.

[Fri11] E. Friedland, N. Van der Berg, J. Malherbe, J. Hanke, J. Barry, E. Wendler and W. Wesch, J. Nucl. Mater. 410 (2011) 24.

[Fri12] E. Friedland, N.G. van der Berg, J.B. Malherbe, E. Wendler and W. Wesch, J. Nucl. Mater. 425 (2012) 205.

[Fri14] E. Friedland, K. Gärtner, T.T. Hlatshwayo, N.G. van der Berg and T.T. Thabethe, Nucl. Instr and Meth. B 332 (2014) 415.

[Hef96] A. Heft, E Wendler, J. Heindl, T Bachmann, E. Glaser, H.P. Strunk and W. Wesch, Nucl. Instr. and Meth. B 113 (1996) 239.

[Hla10] T.T. Hlatshwayo, "Diffusion of silver in 6H-SiC" PhD Thesis, Department of Physics, University of Pretoria, South Africa, 2010.

[Hla12a] T. Hlatshwayo, J. Malherbe, N. van der Berg, A. Botha and P. Chakraborty, Nucl. Instr and Meth. B 273 (2012) 61.

[Hla12b] T. Hlatshwayo, J. Malherbe, N. van der Berg, L. Prinsloo, A. Botha, E. Wendler and W. Wesch, Nucl. Instr and Meth. B 274 (2012) 120.

[Kuh10] R. Kuhudzai, "Diffusion of ion implanted iodine in 6H-SiC", Masters Dissertation, Department of Physics, University of Pretoria, South Africa, 2010.

[Kuh14] R. Kuhudzai ,N. van der Berg, J. Malherbe, T. Hlatshwayo, C. Theron, A. Buys ,A. Botha, E.Wendler , W. Wesch, Nucl. Instr. and Meth. B 332 (2014) 251.

[Mal13] J. Malherbe, N. van der Berg, A. Botha, E. Friedland, T. Hlatshwayo, R. Kuhudzai, E. Wendler, W. Wesch, P. Chakraborty and E. Da Silveira, Nucl. Instr. and Meth. B 315 (2013) 136.

[May97] M. Mayer, SIMNRA User's Guide, Report IPP 9/113, Max-Planck-Institut für Plasmaphysik, Garching, Germany, 1997.

[Web00] W. Weber, Nucl. Instr. and Meth. B 166-167 (2000) 98.

[Web08] W. Weber, L. Wang, Y. Zhang, W. Jiang and I.-T, Bae, Nucl. Instr. and Meth. B 226 (2008) 2793.

[Wes96] W. Wesch, A. Heft, E. Wendler, T. Bachmann and E. Glaser, Nucl. Instr. and Meth. B 96 (1995) 335.

[www1] http://www.srim.org

[Zie85] J. Ziegler, J. Biersack and Y. Littmark, "The Stopping and Range of Ions in Solids, Pergamon Press, New York, 1985.

Chapter 7 Results-Surface microstructure studies of ion implanted SiC

As discussed in section 6.1.1 of chapter 6, some differences were observed concerning the loss of implanted species during the initial annealing cycles for the different types of ions implanted into 6H-SiC at room temperature. No losses were observed for samples implanted with iodine or xenon during the initial annealing cycles while significant losses were observed for samples implanted with strontium, cesium and silver. In the case of silver, Hlatshwayo *et al.* [Hla12b] attributed the loss of silver to the surface escape model via cavities that developed on the sample surfaces after annealing. To get a clearer picture on the effect of the surface microstructure on the release of the these fission product elements, SEM and AFM studies were performed on the samples implanted with cesium, iodine, silver, strontium and xenon to see if any correlation can be made to the losses discussed in section 6.1.1. The results are presented here in section 7.1.

7.1 SEM studies on the annealing behaviour of ion implanted 6H-SiC

Figure 7.1(a) shows a typical SEM image of the as-received un-implanted 6H-SiC wafer. The surface had only some polishing marks (P) observable on it and the surface roughness was found to be approximately 0.5 nm via AFM. Figure 7.1(b) shows the as-implanted surfaces of the xenon implanted sample. The surfaces of all the other as-implanted samples (not shown) are similar to the xenon one. As the sample surfaces were amorphous after implantation, the surfaces were flat and featureless with the polishing marks less pronounced after ion bombardment. The surface roughness was about 1 nm for all the samples. The increase in RMS roughness, as measured by AFM, after ion bombardment is due to sputter-induced roughening [Mal94].

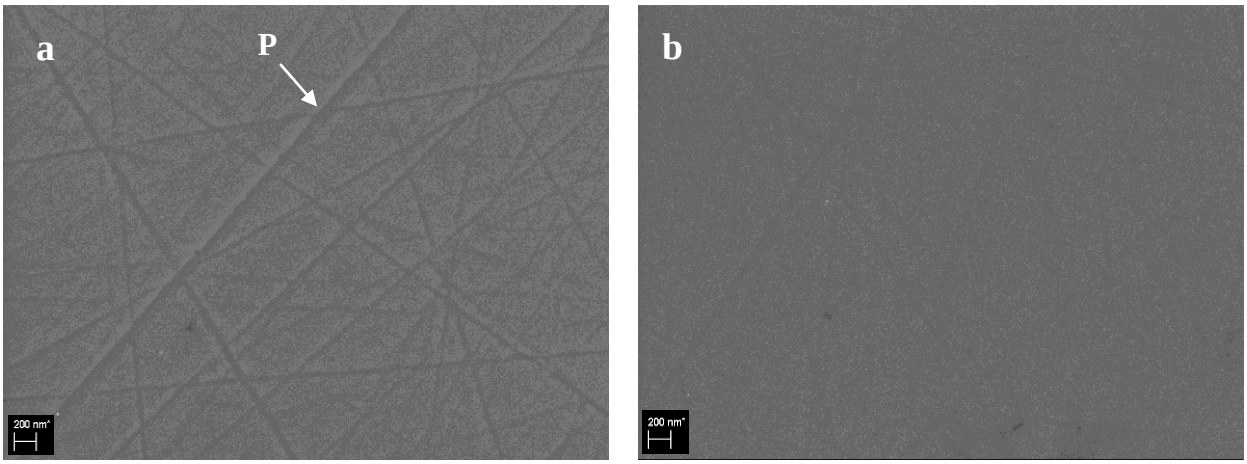

Figure 7.1: SEM images of (a) as received 6H-SiC, and (b) the as-implanted image of 6H-SiC implanted with Xe ions. The ion energy was 360 keV and the implantation was performed at room temperature. The scale bar in the SEM images represents 200 nm.

The images showing the effect of annealing at 1100 ºC for 15 min on implanted samples are shown in figure 7.2. In figure 7.2 (a), for the strontium implanted sample, the surface is no longer featureless. The previously amorphous surface layer appears now to have been recrystallized into a polycrystalline material as some crystallites are observed on the surface although it is difficult to clearly ascertain their size. Figure 7.2 (b) shows the SEM image of the cesium implanted sample; evidence of some recrystallization can be seen from the contrast which seems to be depicting crystallites on the surface. These crystallites are not as developed as those observed on the strontium implanted sample. Elongated thin crystallites (L) appear on the annealed surface of the silver implanted sample (Figure 7.2 (c)), with some extending to a length of about 1 μm. There seem to be no preferred orientation as these needle type crystallites develop randomly on the surface. Star-like crystallites (S) were observed on the surface of the xenon implanted sample (figure 7.2(d)). These crystallites look similar to those observed by Snead *et al*. [Sne98] on annealing of neutron amorphised SiC.

They appear to nucleate from certain points or centres on the surface and grow parallel to the surface. Again there appears to be no preferred orientation for growth.

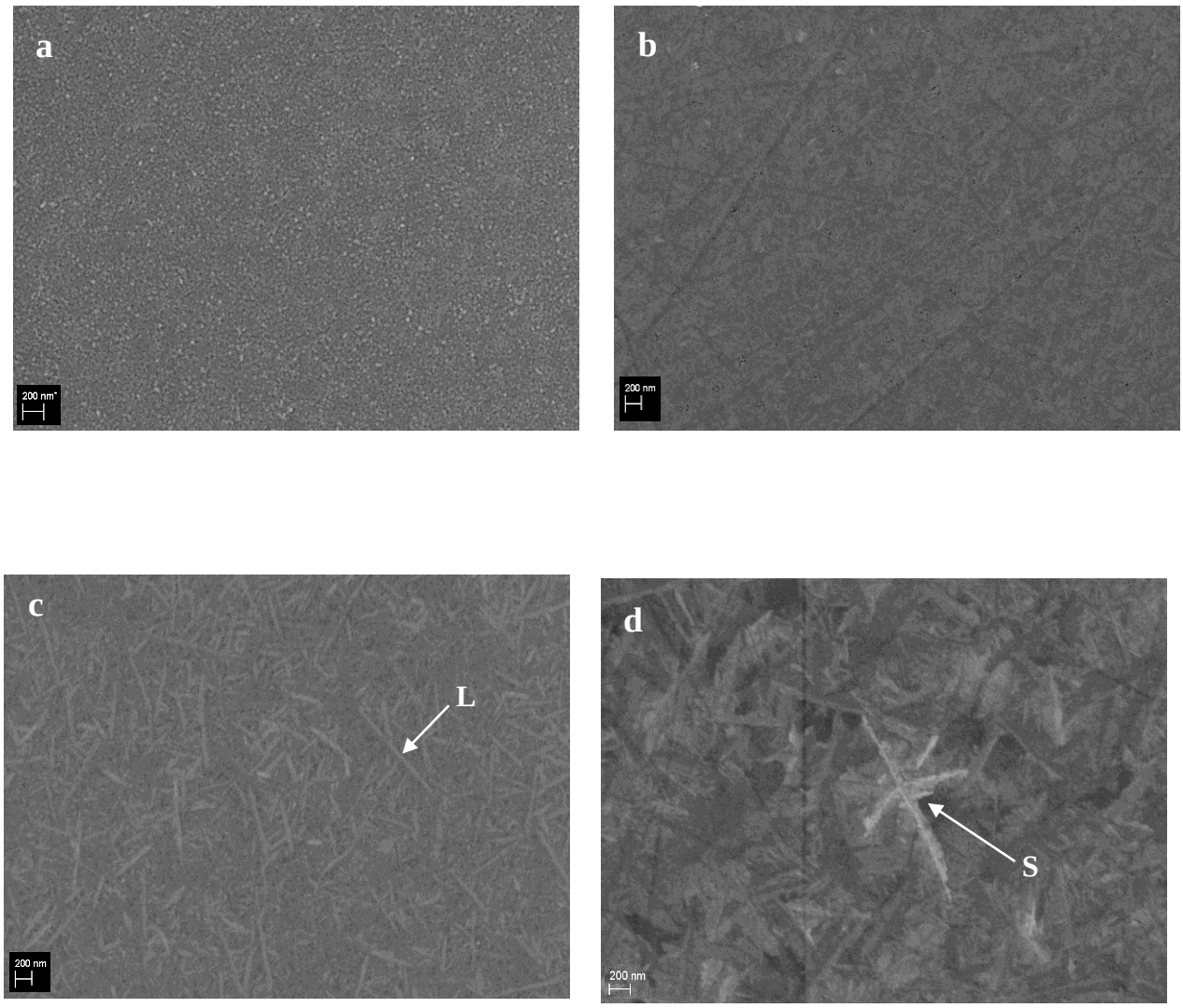

Figure 7.2: SEM images of 6H-SiC wafers implanted with ions of (a) Sr, (b) Cs, (c) Ag and (d) Xe. All the samples were annealed at 1100 ºC for 15 minutes. The ion energy was 360 keV and all implantations were performed at room temperature. Ion fluences for all samples were 1×10^{16} cm^{-2}. The scale bar in the SEM images represents 200 nm.

The surface of the iodine implanted sample (figure 7.3 (a)) is characterised by pockets of closely packed (densely packed regions) of nano crystallites (C) as well as elongated thin crystallites (L). Some of these long crystallites extend to lengths of about 1 μm . In this case the thin crystallites seem to branch out from certain growth centres (G) unlike those observed

for the silver implantation. The crystals are more developed than in the silver case, where needles seem to grow in a sea of amorphous zones while for the iodine implanted sample, thin long crystallites grow along with pockets of closely packed nano crystallites. The case of expedited growth in the presence of iodine is supported by the image showing the sample co-implanted with silver and iodine (figure 7.3(b)). In this case, the long thin crystallites are more pronounced than in the case of silver implantation alone, and the seemingly amorphous zones observed on silver implanted samples are now crystalized with close packed nano crystallites now being visible. A similar trend is observed in figure 7.3(c) which shows the annealed SiC sample co-implanted with cesium and iodine ions. In this image the long thin crystallites (size) are now visible which were not fully developed for the sample only implanted with cesium. At 1100 °C for 15 mins, all the surfaces look to have under gone recrystallization although iodine implanted sample seems to have the most developed crystal structures.

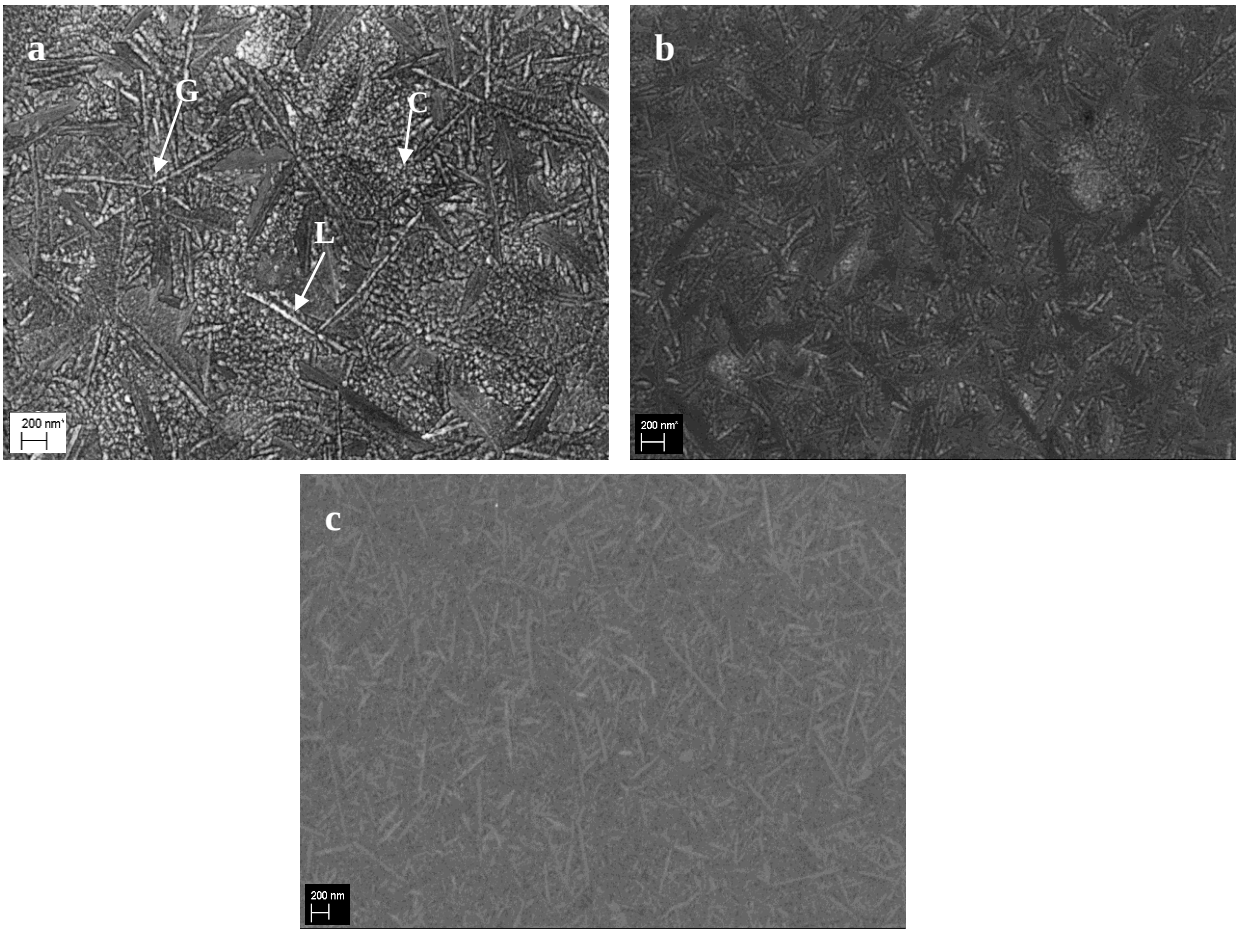

Figure 7.3: SEM images of 6H-SiC wafers implanted with ions of (a) iodine, (b) co-implanted with ions of Ag and I, and (c) co-implanted with ions of Cs and I. All the samples were annealed at 1100 ºC for 15 minutes. The ion energy was 360 keV and all implantations were performed at room temperature. Ion fluencies for all samples were 1×10^{16} cm^{-2}. The scale bar in the SEM images represents 200 nm.

Micrographs of the implanted samples annealed 1200 °C for 5 hours are shown in figures 7.4 and 7.5. For the strontium implanted sample (figure 7.4(a)), the polycrystalline surface observed looks similar to the one observed after the 15 min anneal at 1100 °C. However, the nano crystallites on the surface are now more visible and larger. Cavities (O) on the surface are observable at this annealing cycle. The grain size of some of these crystallites is estimated

to be about 100 nm with a few nano crystallites having grown to approximately to a diameter of 150 nm. AFM analysis shows the surface roughening to approximately 5 ± 1 nm, with the height of some of the larger crystals approximately 17 nm.

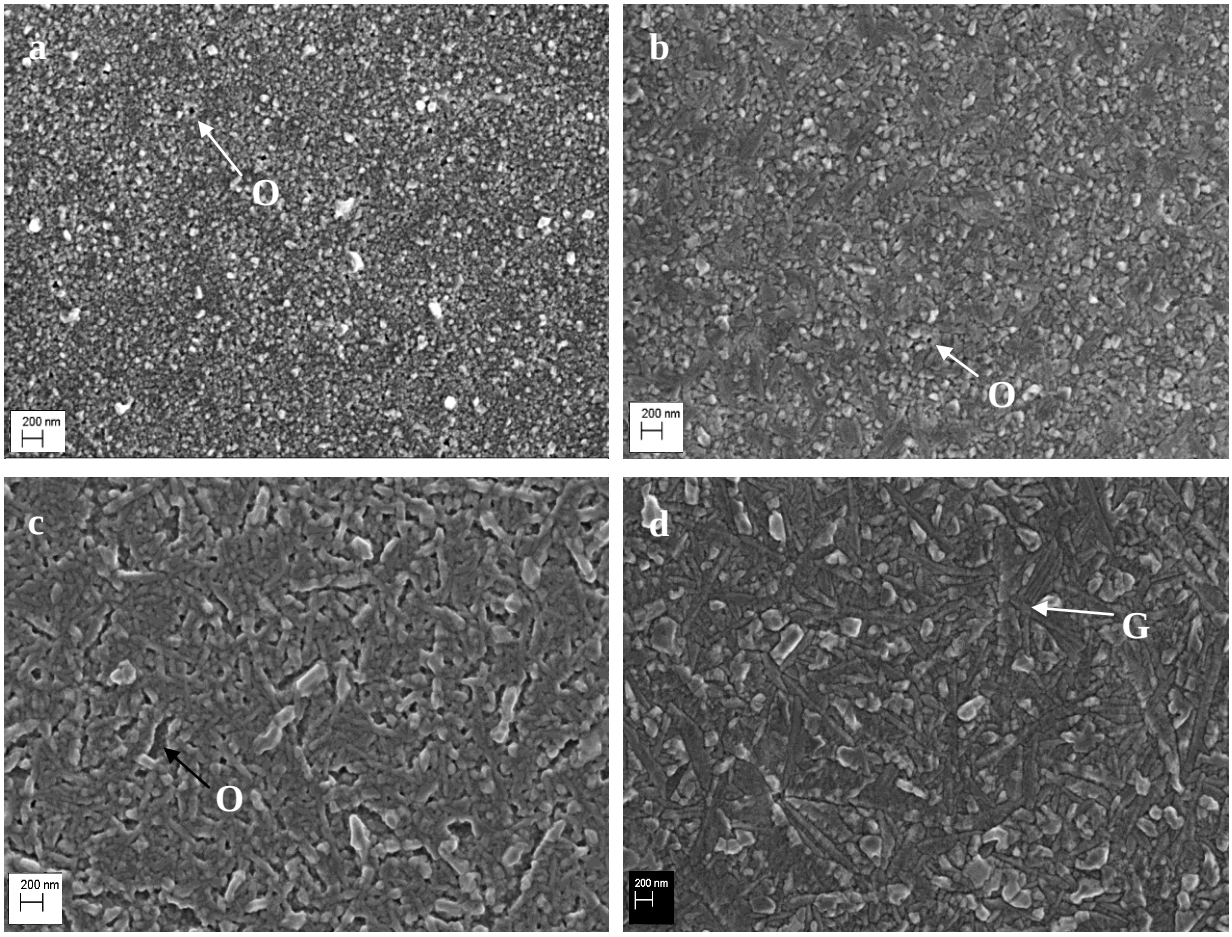

Figure 7.4: SEM images of 6H-SiC wafers implanted with ions of (a) Sr, (b) Cs, (c) Ag and (d) Xe. All the samples were annealed at 1200 ºC for 5 hours. The ion energy was 360 keV and all implantations were performed at room temperature. Ion fluences for all samples were 1×10^{16} cm^{-2}. The scale bar in the SEM images represents 200 nm.

The recrystallization of the amorphous SiC into crystals occurs according to a step-flow mechanism [Bur31]. For the crystals to grow materials must be provided from nearby areas resulting in the formation of cavities. Crystal surfaces with higher surface energies grow

proportionally faster than surfaces with lower surface energies via surface diffusion, according to Wulf's law [Wul01], thereby lowering the total energy of the system.

The cesium implanted sample is shown in figure 7.4(b). In this case the polycrystalline surface is composed of short thin crystallites approximately 300 nm long, and irregular close packed nano crystallites approximately 100 nm in diameter. The surface is also not continuous as cavities are also prominent on this surface. Surface roughness, as measured by AFM, was found to be approximately 6.3 ± 1 nm. The largest crystals on the surface grew to heights of about 20 nm.

From the image of the silver implanted sample (figure 7.4(c)), the recrystallized surface is characterised by a number of cavities (O). The larger cavities on this annealed surface extend to diameters beyond 200 nm and to depths of 45 nm. The top surface is far from being a continuous layer. Although larger crystallites (of diameter larger than 200 nm and height of 45 nm) develop on the surface, their growth via surface diffusion leaves behind large cavities or pits.

On annealing the xenon implanted 6H-SiC (figure 7.4(d)), the surface is characterised by long, thin crystallites branching out from growth centres. These elongated thin crystallites extend to a lengths 700 nm to 900 nm on average. Large faceted crystals (approximately 200-300 nm in diameter) characterised by multiple twinning (visible under higher magnification) have also grown under annealing. These crystals grow to heights reaching approximately 50 nm. The surface appears to be quite continuous, with the large cavities observed for the silver implanted samples not seen in this case. Although the growth mechanism appears be the same, i.e. of larger crystals growing through a crystal surface diffusion supply mechanism, the surface layer does not break up in the xenon implanted sample. Large faceted crystals with a few cavities can be seen on the iodine implanted sample, (figure 7.5(a)). In the case of iodine these crystals easily grow to diameters of about 200 nm and in some cases 400

nm. These crystallites reach heights of approximately 65 nm above the sample surface. Again the thin and elongated crystals branching out from certain growth points are visible. It is quite clear that the largest crystals grow on the iodine amorphised surfaces. Fewer cavities are also observed for annealed samples implanted with iodine and xenon as compared to the cesium, strontium and silver implanted samples.

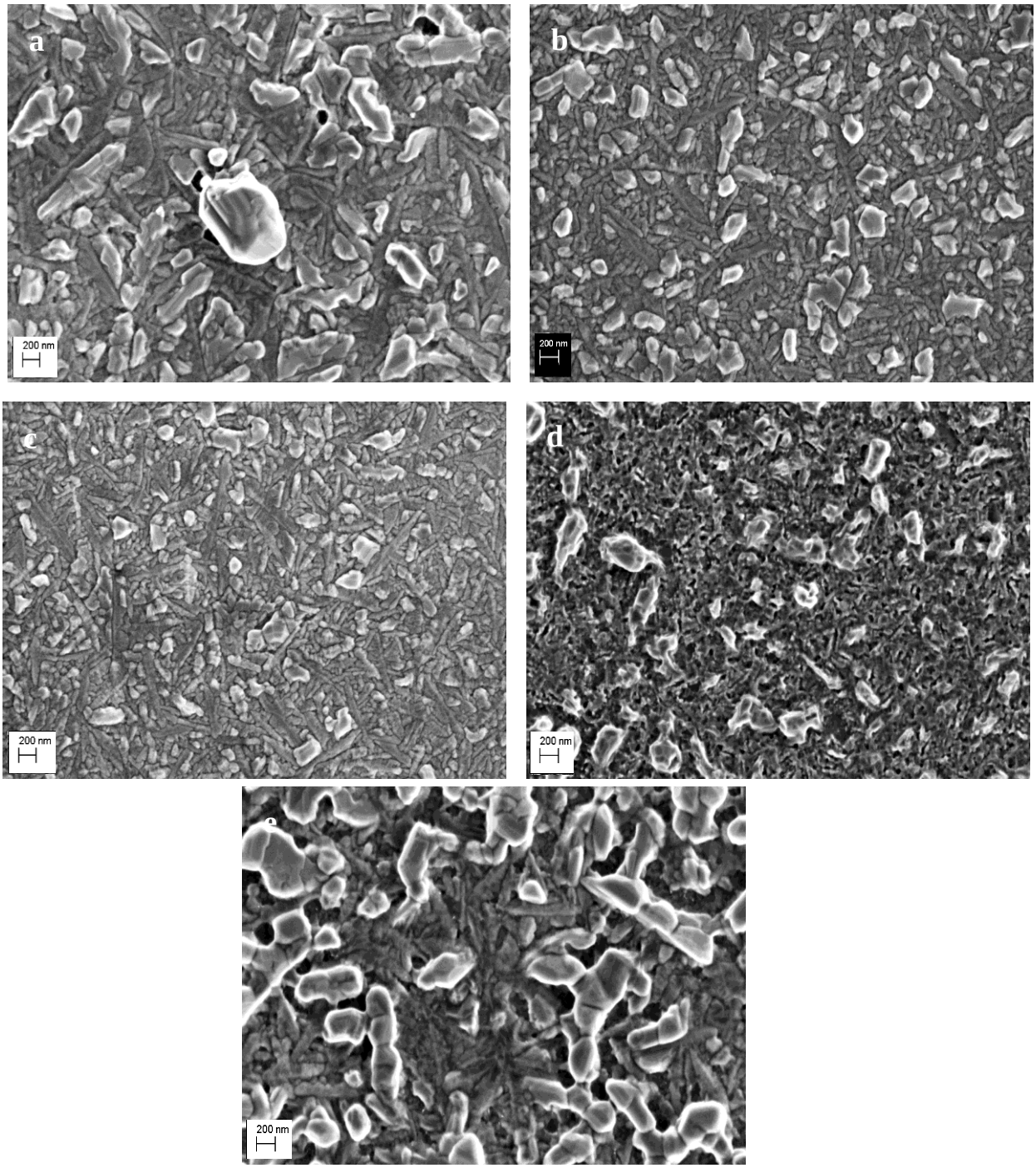

Figure 7.5: SEM images of 6H-SiC wafers implanted with ions of (a) I, (b) co-implanted with ions of Ag and I, (c) co-implanted with ions of Cs and I , annealed at 1200 ºC for 5 hours, (d) implanted with Ag and (e) implanted with I. Samples in (d) and (e) were annealed at 1400 °C for 30 hours. The ion energy was 360 keV and all implantations were performed at room temperature. Ion fluences for all samples were 1 $\times 10^{16}$ cm^{-2}. The scale bar in the SEM images represents 200 nm.

The larger crystallites and fewer but larger cavities observed for the iodine implanted surfaces compared to the other implanted samples could suggest some form of stronger binding or chemical interaction or catalytic action between the iodine and SiC. Malherbe [Mal13] discussed the suggestions previously made that iodine and other halogen elements can aid crystal growth in SiC [Pap99,Ped07,Ram94]. According to Malherbe [Mal13] this process is probably related to compound formation in the amorphous SiC with free Si and C due to the bombardment process. It is known that iodine reacts with silicon above 600°C to form SiI_4 which reacts further with silicon at high temperatures (above 800 °C) to form SiI_2 [Cis02,Wan00]. The SiI_2 again decomposes above 1000 °C. These processes are pressure dependent when performed in fluid conditions. Within a solid, the above temperatures might be different. These processes might explain the report by Ramesh *et al*. [Ram94] that pure 3C-SiC is obtained when heating Si and activated carbon powder in an iodine atmosphere in a commercial microwave oven. These chemical reactions between iodine and free Si, released in the SiC by the ion bombardment process, might lead to the recrystallization driven topography development.

As stated in section 1.2 of chapter 1 modern nuclear fuel elements are coated with a SiC layer to retain radioactive fission products within the fuel elements. The appearance of cavities on the surfaces after annealing might have implications for the nuclear industry. Recently it was proposed that these cavities might act as migration paths for implanted silver in SiC [Hla12b]. It is therefore expected that iodine and xenon are more likely to be retained in SiC while the large cavities observed on silver and cesium and the cavities on strontium implanted samples could provide paths for their release. This is consistent with the loss of implanted elements observed form RBS measurements as discussed in section 6.1.1 of chapter 6.

Annealing for a longer time (30 hours) at a higher temperature (1400 ºC) seems to support the case for some sort of stronger binding in the presence of iodine. Figures 7.5(d) and 7.5(e) show SEM images of SiC implanted with Ag and I respectively after annealing for 30 hours at 1400 ºC. From these images, the crystals on the Ag implanted surface are not as faceted anymore. They appear to be not as defined as in the images of the samples annealed at the lower temperature (1200 ºC for 5 hours figure 7.4(c)). This may indicate that decomposition due to thermal etching is already taking place. In the case of the iodine implanted sample, the large crystals still exhibit well defined facets indicating that the thermal etching is not as advanced at this stage as in the case of silver. Similar results have been observed after annealing at 1500 ºC for 30 hours using Rutherford backscattering spectroscopy (figures 6.7 and 6.8 of chapter 6). These figures show that the increase in the detected surface carbon signal was more pronounced for the silver implanted sample than in the case of iodine implanted SiC. At these temperatures, the decomposition of SiC is accompanied by the evaporation of silicon leaving carbon on the surface [Ber12].

To further investigate the thermal decomposition of the SiC nanocrystallites on the surfaces, samples implanted with ions of iodine were annealed at an even higher temperature of 1700 ºC for 5 hours. Samples implanted with silver ions were also annealed under the same conditions and the SEM images of these samples are shown in figure 7.6.

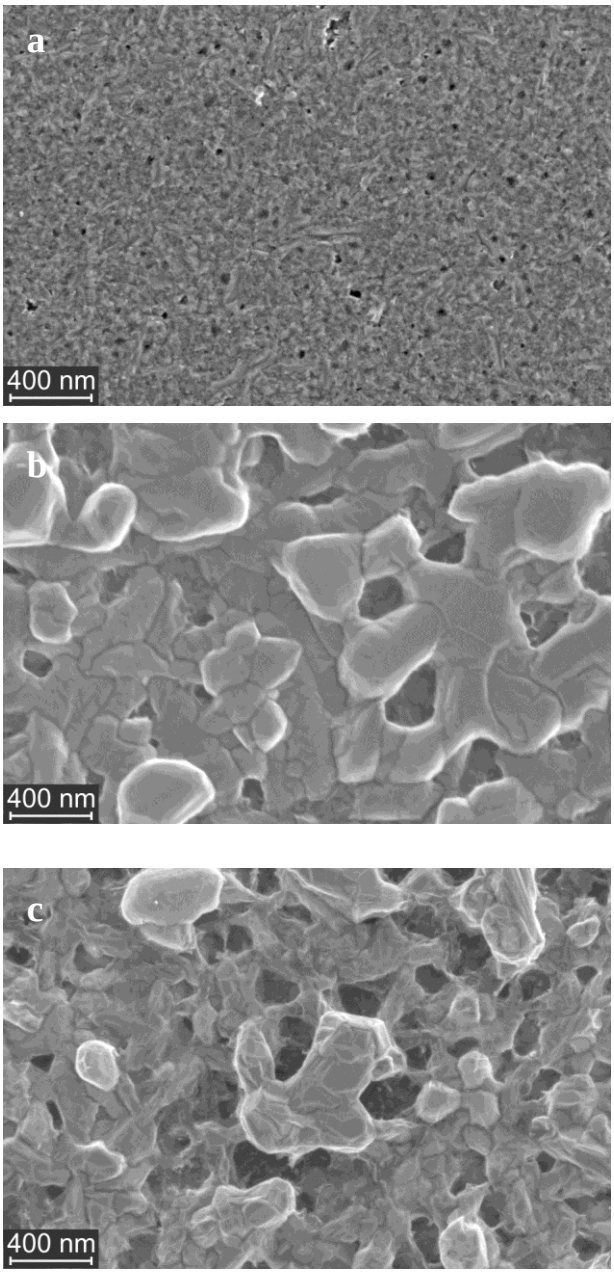

Figure 7.6: In-lens SEM images of the different implanted SiC surfaces after vacuum annealing at 1700 °C for 5 h. (a) 360 keV Ag^{+} implanted to a fluence of 2×10^{16} cm^{-2}. (b) 360 keV I^{+} implanted to a fluence of 1×10^{16} cm^{-2}. (c) Co-implanted 360 keV Ag^{+} and I^{+} implanted, each implanted to a fluence 1×10^{16} cm^{-2}, resulting in a total fluence of 2×10^{16} cm^{-2}.

In figure 7.6 (a) the nano crystallites that were visible on the recrystallized Ag implanted samples after lower temperatures annealing cycles (figure 7.4 (c)) have undergone further decomposition and are now barely visible at this magnification. In contrast, the larger crystals

which grew on the I implanted samples are still clearly visible even at the highest annealing temperatures (figure 7.6(b)). Thus, the presence of I enhances the growth of the surfaces crystals as well as improve their stability at high temperatures. This holds also for the Ag and I co-implanted samples. Figure 7.6(c) shows the surface morphology of the Ag and I co-implanted samples 1700 °C for 5 hours. Here, the large crystals similar to those observed on the samples implanted with I only are observable. The large crystallites on the Ag and I co-implanted sample are still well defined and comparable with the crystallites on the I implanted samples The effect of I on the increased stability of SiC to thermal decomposition could be linked to some form of compound formation. Friedland *et al*. [Fri12] have also previously ascribed the remarkable I retention in SiC to possible compound formation. In a recent review article, Malherbe [Mal13] and references therein, discussed in detail possible compound formation due to interaction of I with free Si in implantation damaged SiC.

To investigate the possible chemical interaction between I and Ag or Si in, XPS studies were performed and the results are presented in the next section, section 7.2.

7.2 XPS studies on I and Ag co-implanted samples

XPS analysis was carried out on the surface of Ag and I co-implanted sample after annealing at 1500 ºC for 30 hours to determine the chemical nature of Ag and I. I 3d high resolution spectrum (figure 7.7(a)) shows doublet peaks at 620.3 eV (I $3d_{5/2}$) and 631.8 eV (I $3d_{3/2}$), which can be ascribed to molecular I_2 [Kau89,Sal80]. If iodine is in the form of AgI, I 3d5/2 peak should be at 618.4 eV associated with I^- [Li08]. Ag 3d spectrum shown in figure 7.7(b) exhibits doublet peaks at 368.9 eV (Ag $3d_{5/2}$) and 374.9 eV (Ag $3d_{3/2}$), which can be assigned to metallic Ag [Li08]. If Ag is in the form of AgI, Ag $3d_{5/2}$ peak should be at 367.2 eV assigned to Ag^+ [Che10]. Thus, both I 3d and Ag 3d spectra confirm the absence of AgI compound in the annealed sample. However, the binding energies of I 3d5/2 and Ag 3d5/2 for AgI in a host matrix like in SiC can be different from that of bulk AgI.

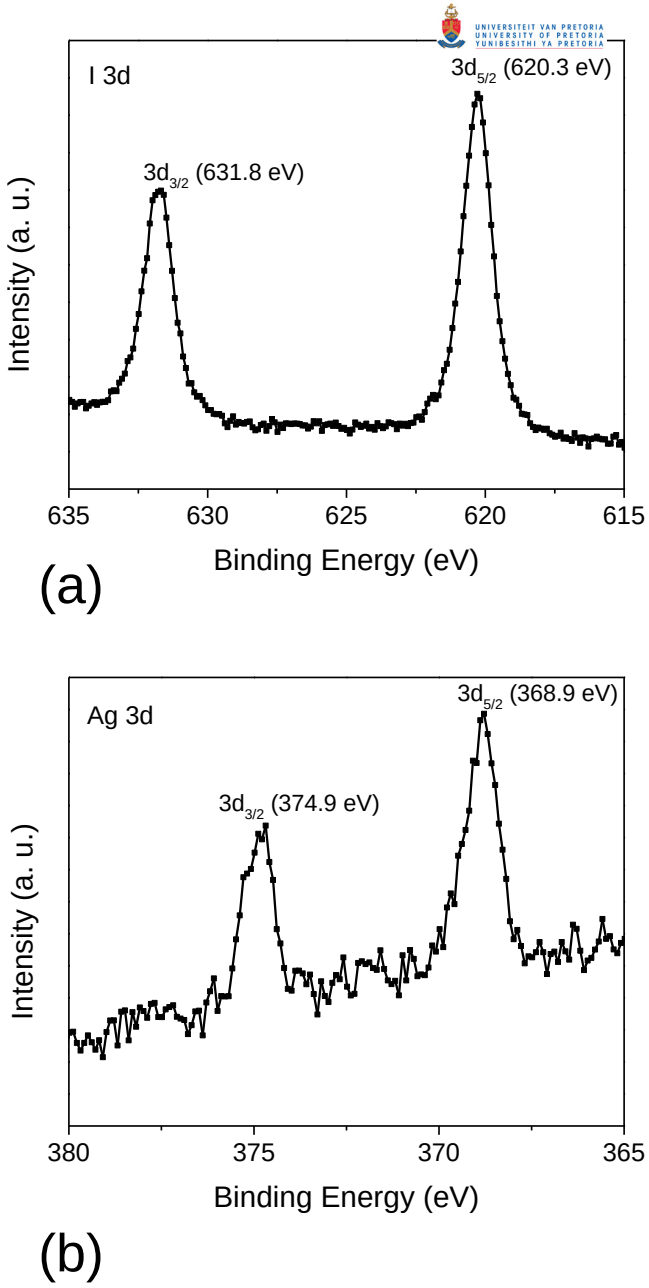

Figure 7.7: High resolution XPS spectra of (a) I 3d and (b) Ag 3d showing the binding energies for I 3d5/2 peak at 620.3 eV and Ag 3d5/2 peak at 368.9 eV, respectively.

Electronic binding energies of AgI nanoclusters into zeolites [Zha01] showed that electronic binding energies had moved to higher energies as compared to electronic binding energies from bulk AgI. Li *et al*. have reported binding energy values of Ag 3d and I 3d for AgI/TiO2 nanostructures similar to the binding energy values observed in this study [Li08]. They have assigned Ag $3d_{5/2}$ peak at 368.8 eV to metallic Ag nanoclusters, which constitute a very thin metallic Ag shell on AgI cores. They also observed I $3d_{5/2}$ peak at 620.1 eV, which was assigned to I_2. The binding energy of the I 3d5/2 peak could also not give any concrete information in terms of I-Si compound formation. As mentioned earlier in section 7.1 of this

chapter, the low loss of I had been pointed to some strong binding effect or compound formation. The APT results in combination with XPS analysis indicating the metallic nature of Ag and I could point to strong binding effects between Ag and I which can be the factor determining the retention of Ag in the co-implanted sample.

7.3 Raman spectroscopy studies on the recrystallization and thermal decomposition of SiC

The thermal decomposition of the SiC surfaces was further investigated by Raman spectroscopy. This work is presented in this section. Figure 7.8 shows optical microscopy images (reflected light) of the as-received 6H-SiC wafer, iodine bombarded and the annealed samples. Here, we show only the iodine implanted samples as all the images were similar for all ion implantations performed. In figure 7.8(a), the as-received wafer is clearly optically transparent as one can see right through it to the sample stage below. After ion implantation with 360 keV iodine ions which renders the near surface region amorphous to a depth of approximately 220 nm [Fri10] the sample is now very opaque – see Figure 7.8(b). This is due to defects that increase the absorption coefficient in materials. In SiC the absorption coefficient increases with defect density and optical transmittance has been found to decrease from 0,55 for virgin 6H-SiC to below 0.20 for amorphous SiC with laser illumination in the visible region [Mus96].

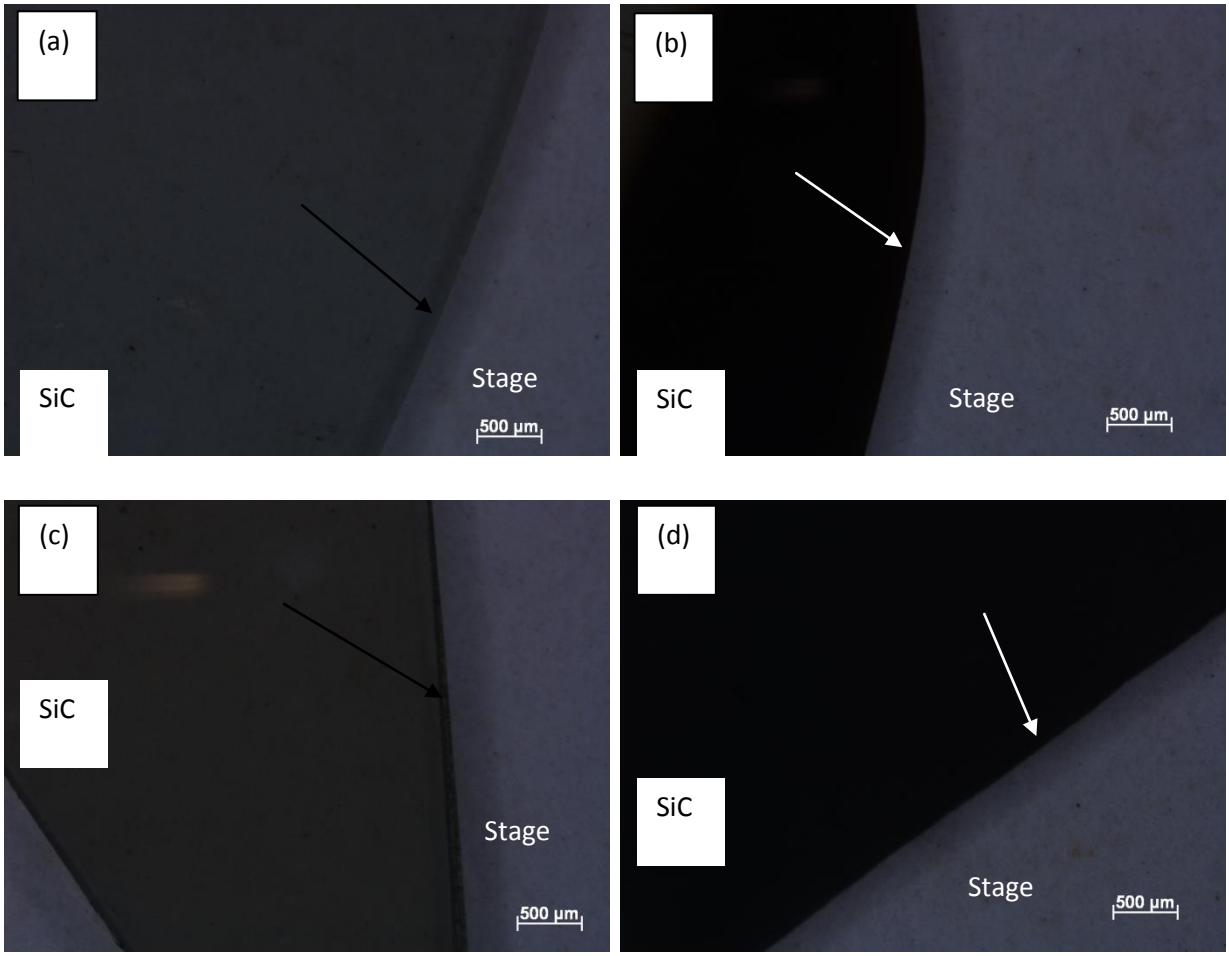

Figure 7.8: Optical microscopy images of (a) a sample cut from the as-received 6H-SiC wafer, (b) the as-implanted sample (implanted with 360 keV iodine ions), (c) the iodine implanted sample annealed at 1200 ºC for 5 hours and (d) the iodine implanted sample sequentially annealed up to 1600 ºC. The arrows indicate the sample edges.

Similar results were observed for our silver as-implanted samples and this behaviour has been found to be independent of ion species implanted [Mus96] as well as for neutron bombarded 4H-SiC and 6H-SiC [Wen12]. Annealing at 1200 ºC caused the sample to become transparent again but with reduced transparency compared to the as-implanted sample – see figure 7.8(c). This is because of the initial amorphous layer recrystallizing in to a polycrystalline material [Fri10]. Sequential annealing from 1200 ºC to 1600 ºC in steps of 100 ºC for 30 hours per cycle caused the sample to become very dark and opaque again (figure 7.8 (d)). This is attributed to the decomposition of SiC at the very high temperatures, especially at 1500 ºC

and 1600 ºC, with silicon sublimating leaving behind a carbon rich layer on the surface [Ber12].

Figure 7.9 (a) shows a comparison between the Raman spectra acquired with the 514 nm laser of the virgin wafer (blue), the as-implanted (green) and the iodine implanted sample annealed at 1200 ºC for 5 hours (red). The spectra of the as-received wafer and the one annealed at 1200 ºC for 5 hours look very similar. Their Raman peak positions due to the sp^3 Si-C bonding [Bol95,Nak97] and width of the 3 signature TO (at wavenumbers 763.5, 785.7 and793.8 cm^{-1}) and the LO peak (wavenumber 962.5 cm^{-1}) are very comparable with only a small decrease in the intensity of the annealed sample. This is attributed to several factors, viz. epitaxial growth of the amorphous layer from the amorphous-crystalline interface, the random crystallites that are formed on the SiC surface during annealing (see section 7.1) and the penetration of the laser light through the semi-transparent implanted (and annealed) layer into the bulk 6H-SiC.

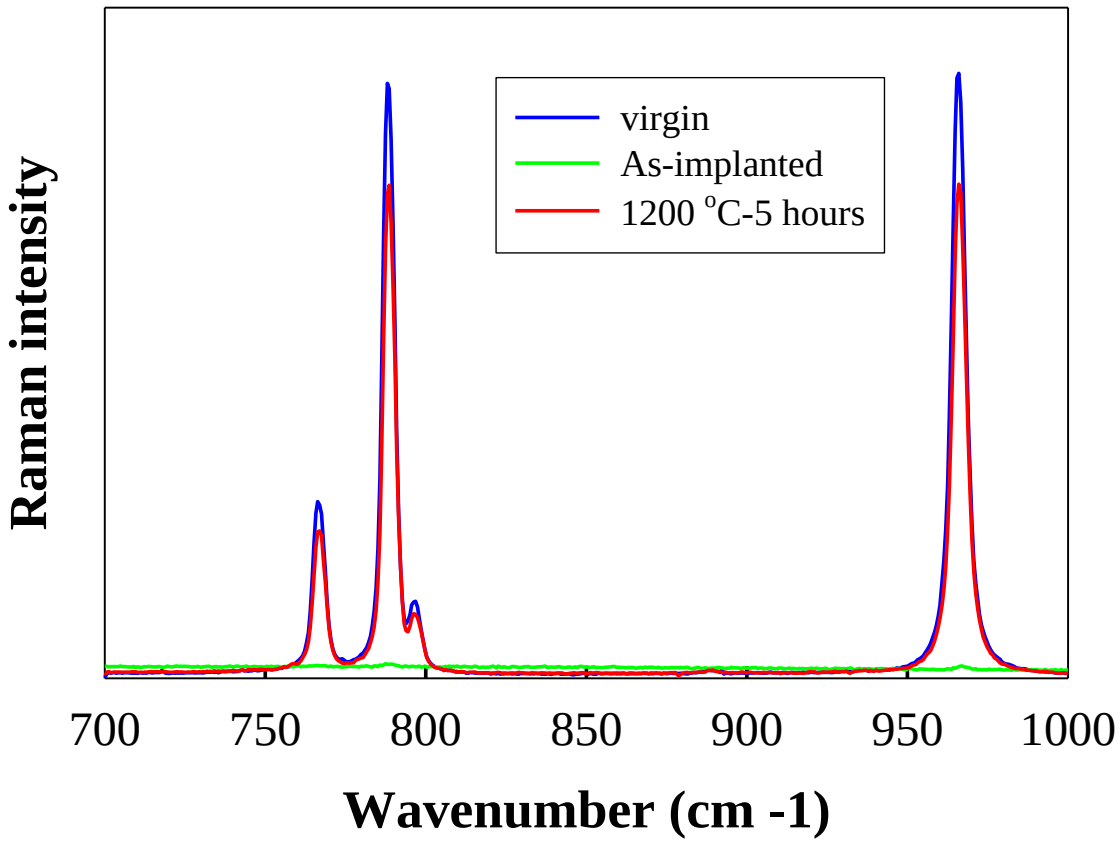

(a)

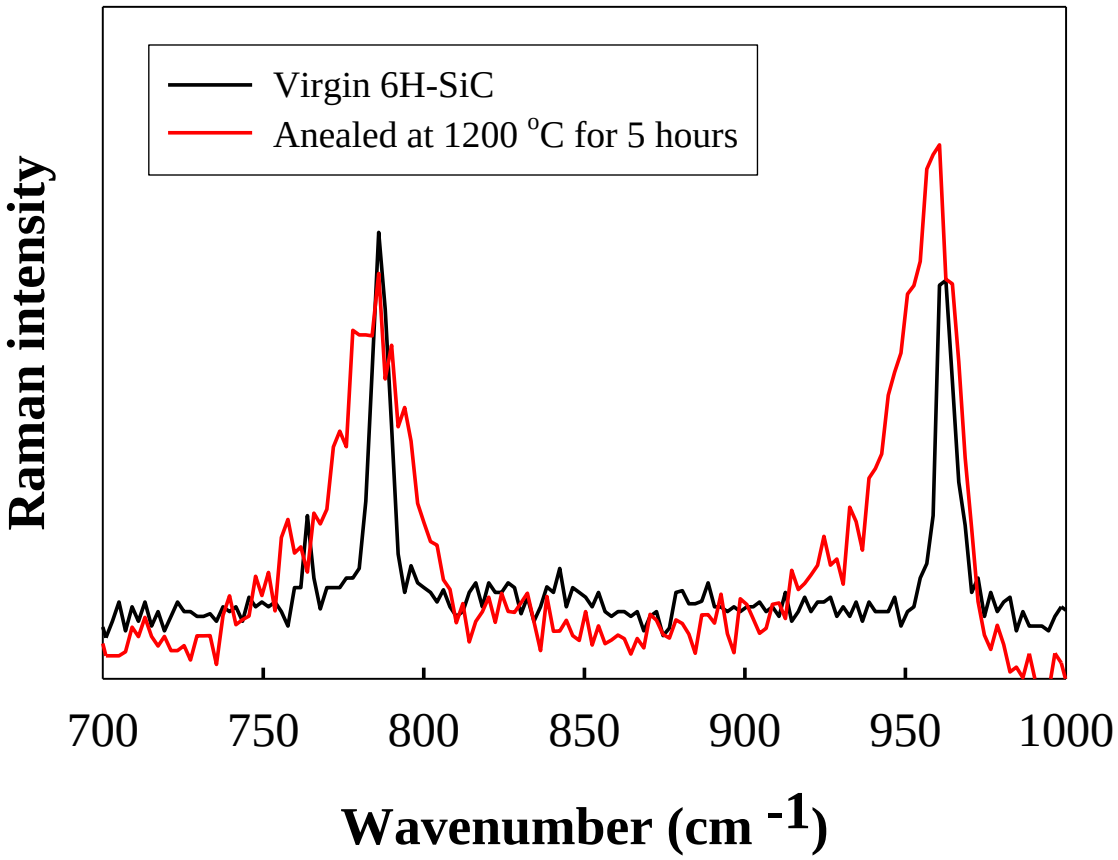

(b)

Figure 7.9: (a) Raman spectra of the virgin 6H-SiC (blue), as-implanted sample implanted with iodine ions (green) and the iodine implanted and annealed sample (red). Raman measurements were performed in the visible region with a 514 nm laser. The corresponding Raman spectra of the virgin and the iodine implanted and annealed sample with the 244 ultraviolet laser are shown in figure 2 (b). The samples were annealed at 1200 ºC for 5 hours.

In the as-implanted sample the 514 nm laser was not able to penetrate the amorphous region resulting in the disappearance of the Raman signature peaks of 6H-SiC. After annealing the 514 nm laser was able to penetrate deeper into the sample resulting in the contribution from the undamaged 6H-SiC dominating the signal from the recrystallized polycrystalline SiC near surface layer. This can also be correlated to their respective optical images shown in figures 7.8 (a) and (c) where the annealed sample regains some of its transparency compared to the

amorphous as-implanted one figure 7.8 (b). The Raman spectra of the amorphous (as implanted sample) (green) is also shown in figure 7.9 (a) for reference; -, here the LO and TO peaks of 6H-SiC are not detected indicating the absence of long range order. With 514 nm laser excitation, it has been found that for 6H-SiC, the probing depth exceeds the projected range of low energy (energy in the order of a few hundred keV) ion implantations [Har06]. For this wavelength the effective penetration depth is around 2 mm for 6H-SiC, although with a 100x objective such as the one used in this work, the sampling depth is typically in the order of a few microns. In our case the projected range of 360 keV iodine ions is about 100 nm as calculated by SRIM [www1] and the resulting amorphous layer was approximately 220 nm thick from the surface. In the amorphous samples (figure 7.8(b) and figure 7.9) the increased sample absorption enables the laser to just probe the near surface damaged region. Similar results were observed for the silver implanted samples.

Figure 7.9(b) shows Raman spectra obtained with 244 nm DUV light of the as-received (virgin) 6H-SiC compared with that of the iodine implanted sample after annealing at 1200 ºC for 5 hours. For the virgin sample, sharp and well resolved peaks of the signature TO (wavenumber 787 cm $^{-1}$) and LO (wavenumber 966 cm $^{-1}$) 6H-SiC peaks at positions are observed. This is due to the well-defined repetitive structure of the hexagonal crystal structure. The broadening and asymmetry (towards the lower wavenumbers) of the LO (wavenumber 960 cm $^{-1}$) and TO (wavenumber 785 cm $^{-1}$) peaks of the annealed sample is due to spatial phonon confinement [Col03] arising from the break down in periodicity due to the nano crystalline nature of the resulting near surface polycrystalline layer (see section 7.1 for SEM images of crystals). The UV exciting laser is capable of isolating the contribution from this near surface region from the bulk Raman signal contributions due to its low penetration depths in 6H-SiC of approximately 50 nm-100 nm [Har06]. Therefore the UV laser excitation was clearly better suited for near surface Raman analysis of annealed ion implanted samples at this temperature than the lasers in the visible range. Similar spectra (not shown) were observed for the silver implanted samples after the same annealing conditions.

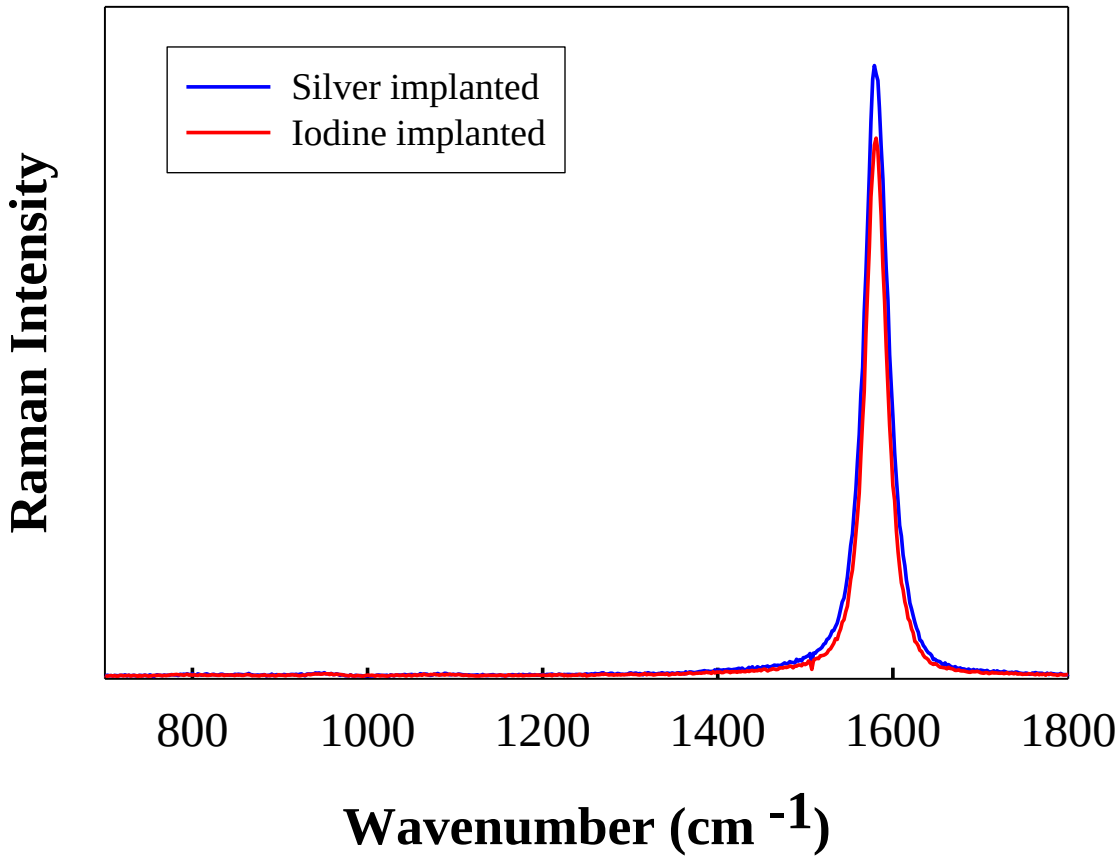

(a)

Figure 7.10: (a) Raman spectra of the sample implanted with iodine ions (red) and silver (blue) annealed up to 1600 ºC for 30 hours. Raman measurements were performed in the visible region with a 244 nm laser.

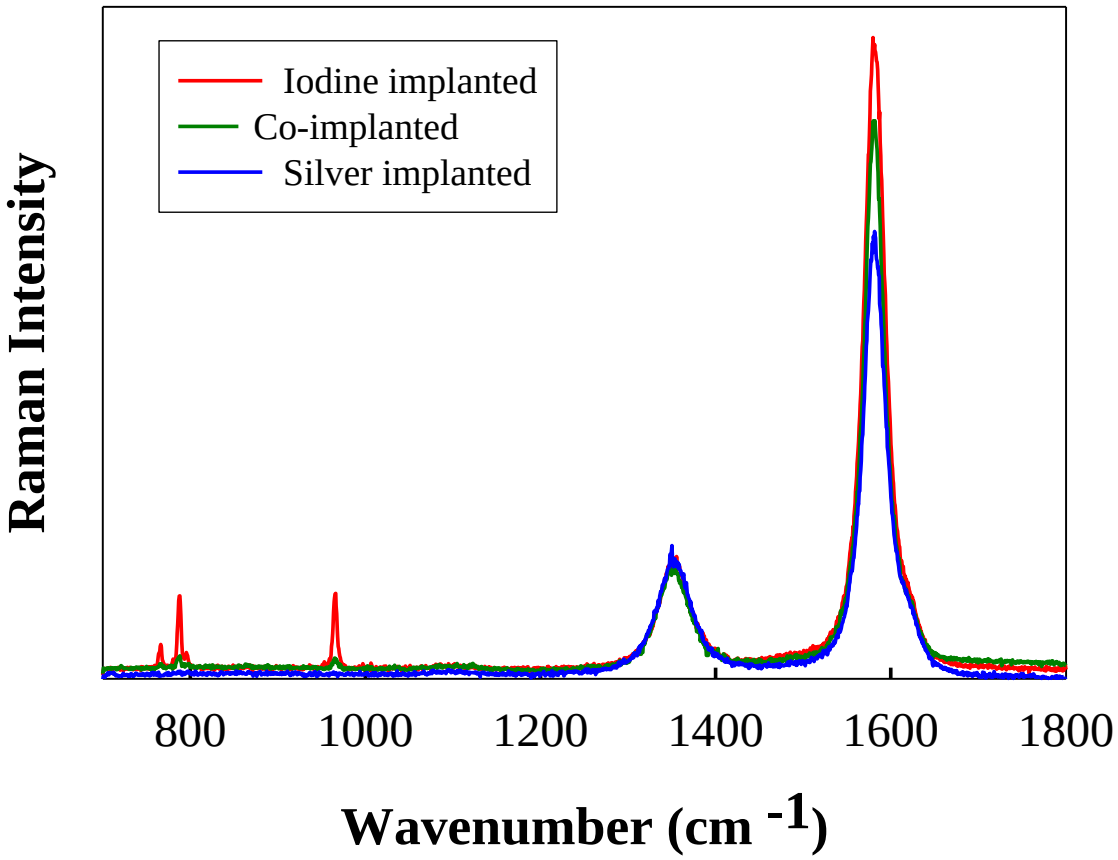

(b)

Figure 7.10: (b) The corresponding Raman spectra of iodine implanted and annealed sample (blue), the silver implanted (green) and the sample with both species co-implanted (red) with the 514 ultraviolet laser are shown in figure 7.10 (b).

The Raman spectra of samples implanted with iodine and silver and annealed sequentially from 1200 ºC up to 1600 ºC in steps of 100 ºC for 30 hours per cycle acquired with the 244 nm excitation laser are shown in figure 7.10(a). From the Raman spectra, a graphite peak from the sp^2 bonding (G band wavenumber 1578 cm^{-1}) is observed. No LO and TO of 6H–SiC Raman peaks were observed. These results indicate that surfaces of both samples were now covered with a layer of carbon, demonstrating that thermal decomposition of SiC had has occurred. For deep ultra-violet DUV excitation at 244 nm, the penetration depth in carbon is ~10-15 nm [Fer01]. Therefore since only the carbon peak is detected the carbon layer here

is thicker than 15 nm. This graphitization of the surface can also be observed optically as shown in figure 7.8 (d). These results are in agreement with Rutherford Backscattering Spectroscopy measurements for silver and iodine implanted samples annealed at temperatures above 1500 ºC (see figures 6.7 and 6.8 in chapter 6).

Figure 7.10(b) shows the corresponding Raman spectra of iodine and silver implanted samples annealed sequentially from 1200 ºC up to1600 ºC in steps of 100 ºC for 30 hours per cycle acquired with the 514 nm excitation laser. The Raman spectrum of a sample co-implanted with ions of both iodine and silver sequentially annealed under the same conditions is also included for comparison. The TO peaks (wavenumbers 766 and 788 cm^{-1}) and the LO peak (at wavenumber 966 cm^{-1}) of SiC were detected in the iodine implanted samples after sequential annealing but not for the silver implanted sample after the same annealing conditions. The same SiC Raman peaks with a reduction in peak heights were however detected for the sample co-implanted with ions of iodine and silver and annealed under the same conditions. The reduction in the SiC peak heights for the co-implanted sample indicates that the carbon surface layer is thicker than in iodine only samples but thinner than for the silver only samples. The 514nm laser was completely absorbed by the carbon layer on the silver implanted samples but not the iodine implanted samples giving an indication of the thickness of the respective layers. The penetration depth in carbon with the 514 nm excitation is approximately 80-100 nm [Amm10]. Since no signature 6H-SiC peaks are detected for the samples implanted with silver after annealing up to 1600 ºC it could imply that the carbon layer on these surfaces is greater than 80 nm while the carbon layer is less than 80 nm thick for the samples implanted with iodine. These results indicate that the presence of iodine somehow reduces the thermal decomposition of SiC at these temperatures. These results are in agreement with Scanning electron microscopy (SEM) results from our previous measurements in the same temperature range (see section 7.1 of this chapter)

The sp^2 (D and G band) peaks at wavenumbers 1350 cm^{-1} and 1579 cm^{-1} respectively, were observed after sequential annealing of all the samples as shown in figure 7.10(b). The G peak arises from the bond stretching of all pairs of sp^2 atoms in both rings and chains while D peak is due to breathing modes of sp^2 atoms in rings [Fer01]. The presence of these peaks is an indication that the surfaces are covered by a carbon layer. The intensity of the G peak is higher for the iodine implanted sample and the co-implanted sample as compared to the silver implanted sample. This could be an effect of iodine enhancing the recrystallization of the

carbon layer with a more graphitic pattern or crystal quality in the presence of iodine (hence the higher intensity G graphitic peak). With the 514 nm laser, the vibrational modes of sp^2 sites have a greater cross section than with 244 nm excitation. Therefore the D peak is detected while it is not detected with the 244 nm laser UV excitation [Gil98]. Similar results showing the absence of the D peak for 244 nm excitation have been observed for Highly Oriented Pyrolytic Graphite (HOPG) [Mon13]. The absence of the D peak at 244 nm can be attributed to two other factors: 1. The well-known trend were the intensity of the D peak decreases with increasing excitation frequency, see ref.[Bor95] and references therein, and 2. The D peak is not detected for graphitic or carbons showing some long range order [Bor95] while small peaks (D peaks) have been detected for amorphous carbons at 244 nm. Since the D peak was not detected at 244 nm excitation in our samples, we can also conclude that the carbon layer on the surface is not amorphous and has some long range order.

The evolution of the SiC nano crystals on the sample surfaces were monitored by Atomic Force Microscopy (AFM). Root Mean Square (rms) roughness values and surface area difference data extracted from measurements are shown in figures 7.11 (a) and (b) respectively. The increase in rms roughness observed for iodine and silver implanted samples from about 21 nm and 28 nm (after 1200 ºC) to about 71 nm and 38 nm (after 1300 ºC) respectively, can be attributed to crystal growth on surfaces. These results were confirmed by SEM (images not shown), and is in line with our previously reported results in section 7.1 of this chapter.

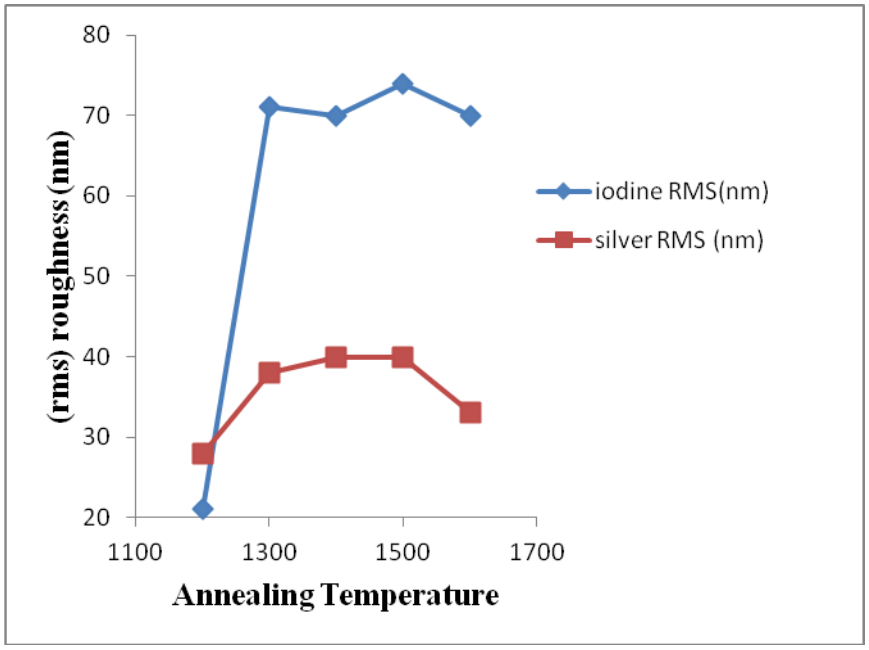

(a)

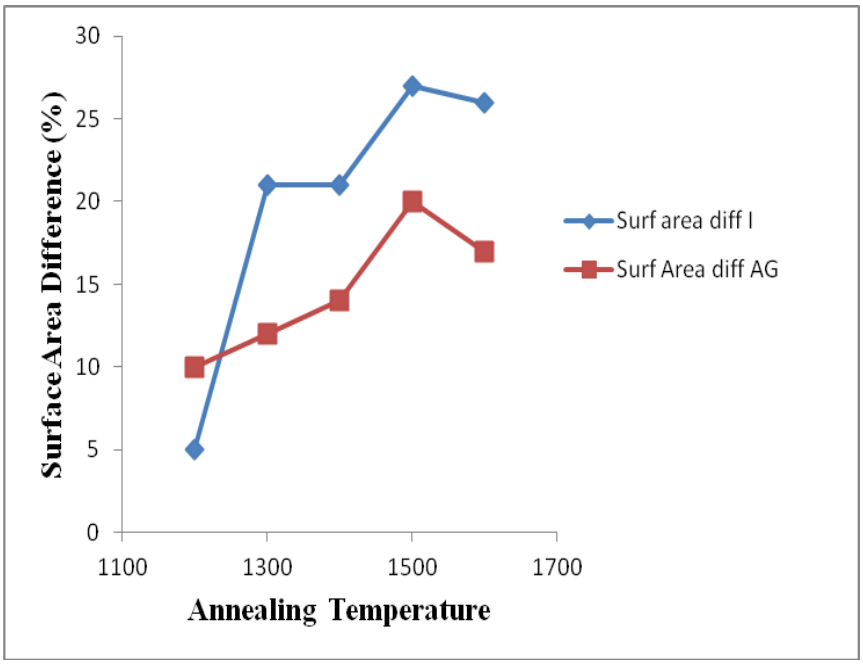

(b)

Figure 7.11: (a) rms roughness values of samples implanted with iodine (blue) and silver (red). (b) surface area difference values extracted from AFM images for the same samples. The samples were implanted at room temperature and anneals sequentially from 1200 ºC to 1600 ºC for 30 hour cycles.

A corresponding increase can also be seen from the surface area difference curves. The surface area difference is defined as the difference between the analysed region's three-dimensional surface area and its two-dimensional projected surface area [www2]. The steeper increase in roughness for iodine implanted samples is due to the fact that larger crystals have been observed to grow on iodine samples as compared to silver implanted samples. The dip in the roughness curves for the silver implanted samples and the corresponding reduction in the surface area difference after annealing at 1600 ºC can be related to the thermal etching of SiC nano crystallites on the surface. This etching of the crystallites has been observed via SEM analysis (see section 7.1). The dip in both the roughness and the surface area difference for the iodine implanted sample is markedly less drastic than the dip observed for the silver implanted sample. This could further support the case that iodine has a stabilising effect on the SiC and agrees with the Raman results discussed above.

References

[Amm10] M. Ammar, J. Rouzaud, C. Vaudy, N. Toulhoat and N. Moncoffre, Carbon 48 (2010) 1244.

[Ber12] N. van der Berg, J. Malherbe, A. Botha and E. Friedland, Appl. Surf. Sci. 258(2012) 5561.

[Bol95] W. Bolse, J. Conrad, T. Rödle and T. Weber, Surface and Coatings Technology 74 (1995) 927.

[Bor95] R. Bormett, S. Asher, R. Witowski, W. Partlow, R.Lizewski and F. Pettit, J. Appl. Physics. 77 (1995) 5916.

[Bur31] W. Burton, N. Cabrera, F. Frank, Philos. Trans. R. Soc. 243A (1931) 299.

[Cis02] T. Ciszek, H. Wang, M. Page, R. Bauer and M. Landry, IEEE 21 (2002) 206.

[Col03] P. Columbian, Spectroscopy Europe 15 (2003) 8.

[Fer01] A. Ferrari and J. Robertson, Phys. Rev. B 64 (2001) 075414-1.

[Fri10] E. Friedland, N. van der Berg, J. Malherbe, R. Kuhudzai, A. Botha, E. Wendler and W. Wesch, Nucl. Instr. and Meth. B 268 (2010) 2892.

[Gil98] K. Gilkes, H. Sands, D. Batchelder, W. Milne and J. Robertson,J. Non-Crystalline. Solids. 227 (1998) 612.

[Har06] H. Harima, Microelectronic Engineering, 83 (2006) 126.

[Hla12b] T. Hlatshwayo, J. Malherbe, N. van der Berg, L. Prinsloo, A. Botha, E. Wendler and W. Wesch, Nucl. Instr and Meth. B 274 (2012) 120.

[Che10] H. Cheng, B. Huang, Y. Dai, X. Qin, and X. Zhang, Langmuir 26 (2010) 6618.

[Kau89] R. Kaufmann, H. Klewe-Nebenius, G. Pfennig, and H. J. Ache, Fresenius Z. Anal. Chem. 333 (1989) 398.

[Li08] Y. Li, H. Zhang, Z. Guo, J. Han, X. Zhao, Q. Zhao, and S. Kim, Langmuir 24 (2008) 835.

[Mal94] J. Malherbe, CRC Crit. Rev. Solid State Mater. Sci. 19 (1994) 129.

[Mal13] J. Malherbe, J. Phys. D Appl. Phys. 46 (2013) 473001.

[Mon13] G. Montagnac, R. Caracas, E. Bobocioiu, F.Vittoz and B. Reynard, Carbon 54 (2013) 68.

[Mus96] P.Musumeci, L. Calcagno, M. Grimaldi and G. Foti, Nucl. Instr. Meth. B 116 (1996) 327.

[Nak97] S. Nakashima and H. Harima, Phys. Stat. Sol. A 162 (1997) 39.

[Pap99] G. Papasouliotis and S. Sotirchos, J. Mater. Res. 14 (1999) 3397.

[Ped07] H. Pedersen, S. Leone, A. Henry, V. Darakchieva, E. Janzén, Surf. Coat. Technol.201 (2007) 8931.

[Ram94] P. Ramesh, B. Vaidhyanathan, M. Ganguli and K. Rao, J. Mare. Res 9 (1994) 3025

[Sal80] W. Salaneck, H. Thomas, R. Bigelow, C. Duke, E. Plummer, A. Heeger, and A. MacDiarmid, J. Chem. Phys 72 (1980) 3674.

[Sne98] L. Snead, S. Zinkle, J. Hay and M. Osborne, Nucl. Instr and Meth. B 141 (1998) 123.

[www1] http://www.srim.org

[www2] http://www.bruker.com

[Wan00] T.H. Wang, T.F. Ciszek, J. Electrochem. Soc. 147 (2000) 1945.

[Wen12] E. Wendler, T. Bierschenk, F. Felgenträger, J. Sommerfeld, W. Wesch, D. Alber, G. Bukalis, L. Prinsloo, N. van der Berg, E. Friedland and J. Malherbe, Nucl. Instr. and Meth. B 286 (2012) 97.

[Wul01] G. Wulff, Z. Krist, Z. Kristallogr. 34 (1901) 449.

[Zha01] Q-Z. Zhai, W-H. Hu, X. Guan, T-Su Jiang, S. Qiu, M-Q Zou, Journal of Solid State Chemistry 169 (2001) 81.

Chapter 8 :Conclusions

The diffusion of several of the significant fission product elements in SiC along with the effect of the surface microstructure on this diffusion has been presented in this thesis. One of the fission products elements concerned was cesium, where a new full in-depth diffusion study in both single and polycrystalline SiC was presented. These were results compared with those from previous studies pertaining to the diffusion of iodine, silver, strontium and xenon. (These studies were from our research group in which I contributed to the measurements and interpretation to different extent. For example, the iodine studies were done by my as part of my MSc project.) A strong correlation was found between the loss of implanted material and surface microstructure after annealing by comparing the release of implanted species under similar conditions and new information gathered by SEM and AFM studies on the samples of all these elements.

From isochronal annealing experiments performed on room temperature implanted samples, about 50 % of the implanted cesium was lost during the initial 5 annealing hour cycles at 1100 ºC. For the xenon implanted samples no loss of xenon was observed for the first annealing cycle and up to the 1200 ºC annealing cycle for both 6H-SiC and polycrystalline samples. Similarly no loss of iodine was observed during the first annealing cycles with broadening of the iodine profile only above 1100 ºC. Approximately 4 % of implanted silver was lost after the first annealing cycle at 1100 ºC with about 47% loss after the 1400 ºC annealing cycle for 6H-SiC samples. The loss of cesium during the first annealing cycle however, was found similar to the behaviour of strontium where strong diffusion is observed for room temperature implanted 6H-SiC after the first annealing cycle at 1000 ºC.

From SEM analysis, new results reported in this study showed that the appearance of cavities on the surfaces after annealing might have acted as surface diffusion migration paths or as openings for vapours for implanted species in SiC. Surfaces of iodine and xenon implanted samples were more continuous and containing less cavities than surfaces of cesium, strontium and silver implanted samples. It therefore explains why iodine and xenon retention after initial annealing cycles was higher in SiC while the large cavities observed on silver and cesium and the cavities on strontium implanted samples resulted in their release from SiC.

A strong temperature dependence of irradiation induced diffusion during cesium implantation was also observed. A broadening of the cesium profile at the higher implantation temperature (600 ºC) of nearly 40% was observed. Less than 15% broadening was previously observed for two other ion species iodine and strontium and less than 5% difference for silver. Since iodine is almost as heavy as cesium, this dependence was found not to be directly related to the ion mass. With regards to the radiation damage retained after implantation, the surface region of the cold implant was up to a depth of about 190 nm totally amorphous. This amorphous region only partly re-grows epitaxially from the bulk during annealing while the remainder re-crystallizes into a finely grained polycrystalline phase. The implant at 350 ^{o}C exhibited a highly disordered buried layer from 25 to 180 nm below the surface, which, however, was not yet fully amorphous, as the crystal lattice is restored after annealing. At an implantation temperature of 600 ^{o}C, the crystal structure is retained, albeit with a high degree of distortions. The level of radiation damage retained with respect to the implantation temperature could be also be correlated to the release of the implanted cesium from SiC. No loss of cesium in samples implanted at 600 ^{o}C, while approximately 50% is lost during the first annealing cycle in the samples implanted at room temperature. Obviously cesium diffuses relatively fast through the amorphous region towards the surface, where it evaporates into the vacuum. Approximately 25 % of the cesium was lost for samples implanted at 350 ºC.

Isothermal annealing experiments on the room temperature implants show the expected strong initial diffusion through the amorphous near surface region before re-crystallization, but no further diffusion during subsequent annealing cycles. No diffusion at all was observed in the higher temperature implantations at the two temperatures above room temperature. For the latter, the diffusion coefficients were obviously below our detection limit of 10^{-21} m^2 s^{-1} in all cases.

SEM images and AFM analysis also suggest that iodine is more effective in promoting crystal growth during the annealing of bombardment-induced amorphous SiC layers than the rest of the ions we implanted. In samples of silicon carbide co-implanted with iodine and silver, fewer cavities were visible on the surface indicating that iodine influenced the recrystallization. Surface crystallites that grew on the iodine implanted surfaces were more resistant to thermal etching and decomposition than those that grew on the silver implanted

samples at temperatures of up to 1400 ºC for 30 hours. The samples were annealed at an even higher temperature of 1700 ºC for 5 hours. The nano crystallites that were visible on the recrystallized Ag implanted samples after lower temperatures annealing cycles had now undergone further decomposition and were now barely visible. In contrast, the larger crystals which grew on the I implanted samples are still clearly visible even at the highest annealing temperatures. Thus, the presence of I enhances the growth of the surfaces crystals as well as improve their stability at high temperatures. This holds also for the Ag and I co-implanted samples. The large crystals similar to those observed on the samples implanted with I only were still visible. The large crystallites on the Ag and I co-implanted sample were still well defined and comparable with the crystallites on the I implanted samples.

The effect of I on the increased stability of SiC to thermal decomposition could explain the I assisted retention of Ag in co-implanted SiC samples. This synergistic behaviour of iodine (I) and silver (Ag) ions co-implanted into 6H-SiC after annealing was investigated by RBS, ERDA, TOF-SIMS, APT and XPS. Depth profiles after annealing at 1500 ºC for 30 hours showed both I and Ag were still present in the co-implanted samples while complete loss of Ag was observed for the single element Ag implanted samples annealed under the same conditions. However, for I only implanted samples, some iodine was retained. These results suggest that I plays a role in the retention of Ag in SiC. APT analysis clearly indicated formation of both Ag and I clusters in the annealed co-implanted sample. Also a clear spatial correlation of Ag and I clusters was observed in the APT results. The APT results in combination with XPS analysis does not contradict the assumption that there is binding between Ag and I. Thus by utilizing multimodal chemical imaging we have clearly identified the reasoning for retention of Ag due to I in SiC which we believe can be important for understanding the fission product transport through SiC.

The decomposition/thermal etching of the near surface amorphous layers retained after ion implantation into 6H-SiC at room temperature was also investigated by the combination of Raman spectroscopy in the visible and DUV regions. Analysis of the characteristic TO and LO 6H-SiC Raman peaks with laser excitation in the visible range, showed that annealing of the samples at 1200 ºC for 5 hours resulted in the reappearance of the characteristic Raman peaks that look very similar to the virgin samples, although with lower intensity due to some retained defects upon recystallisation of the SiC surface layers. The similarities between the virgin and the annealed sample spectra were due to the deep penetration of the laser in the

visible range resulting in the signal from the bulk undamaged SiC contributing to the overall spectra. However, DUV laser excitation showed that after annealing the peaks are broader and asymmetrical compared to the virgin samples synonymous with the contribution of the nanocrystalline materials. Sequentially annealing up to higher temperature (i.e. 1600 ºC) annealing cycles caused the complete decomposition of the top surface layer of the SiC. Raman measurements with laser light in the visible region showed that the extent of decomposition at 1600 ºC was greater for the silver implanted samples than for the iodine implanted samples. These results show that combination of both the DUV and visible Raman measurements would be best suited for analysis of the evolution of thermal decomposition of ion implanted 6H-SiC at the higher temperatures.

In future, we plan to perform angle resolved XPS analysis to obtain more information about the chemical state of Ag and I on the surface and near surface of the sample. This analysis should incorporate samples annealed over a wider temperature range starting from lower temperature around 900 ºC where SiC recrystallization is known to occur. Annealing from 900 ºC, which is well below the boiling point of AgI could also help shed more light on the possible formation of AgI. As cesium is one of the two fission products (along with silver) that have been detected outside intact fuel particles, one of the areas of focus of our future studies will be to investigate the effect of co-implantation of cesium with iodine. This study will help us understand if there are any synergistic effects similar to what we have observed in this study for iodine and silver co-implanted samples. We envisage to use a mix of a number of characterisation techniques including, Atom Probe Tomography, Secondary ion mass Spectrometry and Transmission Electron Microscopy. We will also explore further the thermal etching of the surface layers of SiC by widening the range of implanted ions and using additional characterisation techniques such as Scanning Tunnelling Microscopy and XRD for chemical analysis.

Chapter 9: Research outputs

The work in this thesis has contributed to several publications and conference proceedings. A summary of these research outputs is listed below:

9.1 Publications in peer-reviewed or refereed journals

1.**R.J. Kuhudzai** , E.K. Friedland , J.B. Malherbe , T.T. Hlatshwayo , C.C. Theron , A.V. Buys, A.J. Botha, E.Wendler c , W. Wesch, "Near-surface recrystallization of the amorphous implanted layer of ion implanted 6H-SiC", Nuclear Instruments and Methods in Physics Research B 332 (2014)252-256.

2.T.T. Hlatshwayo, N.G. van der Berg ,M. Msimanga, J.B. Malherbe, **R.J. Kuhudzai**, "Iodine assisted retainment of implanted silver in 6H-SiC at high temperatures", Nuclear Instruments and Methods in Physics Research B 334 (2014)101-105

3. J. B. Malherbe, N.G. van der Berg, A.J. Botha, E. Friedland, T.T. Hlatshwayo, **R.J. Kuhudzai**, E. Wendler, W. Wesch, P. Chakraborty, E.F. da Silveira "SEM Analysis of ion implanted silicon carbide" Journal: Nuclear Instruments and Methods in Physics Research B 315(2013) 136-141.

4.E. Friedland, N.G. van der Berg. T.T. Hlatshwayo, **R,J. Kuhudzai**, J.B. Malherbe, E. Wendler, W. Wesch "Diffusion behaviour of Cesium in silicon carbide at T>1000 ºC" Journal: Nuclear Instruments and Methods in Physics Research B 286 (2012) 102-107.

5.E. Friedland, N.G. van der Berg, J.B. Malherbe, **R.J. Kuhudzai**, A.J. Botha, E.Wendler, W. Wesch "*Study of iodine diffusion in silicon carbide"* Journal: Nuclear

9.2 Conference Presentations

9.2.1 International Conferences

Czech Republic, September 2014

18th Microscopy Congress, Prague, Czech Republic

AFM and SEM studies on high fluence, low energy iodine implantation in 6H-SiC (Poster presentation)

Belgium, September 2014

19th IBMM Conference Leuven, Belgium

Deep ultra violet and visible Raman spectroscopy studies of ion implanted 6H-SiC: Recrytallisation behaviour and thermal decomposition/ thermal etching of the near surface region

United States of America, June 2013

21ST Ion Beam Analysis Conference, Seattle, Washington State

Near surface recystallisation of ion implanted silicon carbide (Poster presentation)

Japan, October 2012

2nd Nuclear Materials Conference

Annealing studies of cesium and iodine co-implanted 6H-SiC. (Poster Presentation)

Zimbabwe, December 2011

6th International Conference of Africa Materials Research Society

Ion implantation of Iodine and Cesium in 6H-SiC, damage production and diffusion behaviour (Oral presentation

Brazil, April 2011

20th Ion Beam Analysis (IBA) Conference, Itapema

Ion implantation of Iodine in 6H-SiC, damage production and diffusion behaviour. (Poster presentation)

9.2.2 National conferences

Cape Town, December 2012

50th Microscopy Society of Southern Africa Conference (MSSA)

Annealing studies of ion implanted 6H-SiC (Oral Presentation)

Durban, July 2009

South Africa Institute of Physics Conference

Radiation damage and diffusion of iodine in 6H-SiC. (Poster Presentation)